Airborne Wind Energy Airfoils

Design of Pareto-optimal airfoils for rigid wing systems in the field of Airborne Wind Energy

E.J. Kroon 4157958

MSc. Thesis
Aerospace Engineering

TU Delft Delft University of Technology

Aerodynamics and Wind Energy

October 24, 2018

Airborne Wind Energy Airfoils

By

Erik Jan Kroon

in partial fulfilment of the requirements for the degree of

Master of Science
in Aerodynamics and Wind Energy

at the Delft University of Technology,
to be defended publicly on October 24, 2018

Supervisor:	ir. Gaël de Oliveira Andrade
Thesis committee:	Prof. dr. Simon Watson
	Dr. ir. Matteo Pini
	ir. Nando Timmer

Preface

This Master of Science Thesis has been written at the Wind Energy group of Delft University of Technology; faculty of Aerospace Engineering; Aerodynamics, Wind Energy, and Propulsion department, in fulfilment of the master program Aerodynamics and Wind Energy.

I would like to express my gratitude to the many people that have helped me. First I would like to thank the company 'e-kite' which took me in as an intern and showed me the exciting new possibilities in the field of Airborne Wind Energy. Special thanks to Coert Smeenk and Alfred van den Brink for the interesting discussions and the guidance during my internship, and Uwe Fechner (contracted by e-kite) for providing the topic of this thesis.

Many thanks to my supervisor Gaël de Oliveira Andrade, without whose previous work this thesis would not have existed, and whose extensive experience and advice have been a tremendous help.

Last but not least I would also like to thank my friends and family who have supported me for many years helping me get to where I am now.

Erik Kroon,
Delft, October 24, 2018

Summary

The goal of this thesis is to provide airfoil designs specific to rigid wing systems used in Airborne Wind Energy (AWE). The airfoils will be designed using optimisation techniques. Because airfoil optimisation is already mature, the focus of the thesis lies on using previous research to set up suitable design goals. Airfoils are optimised for these goals. Insights gained from these airfoils are used to update and improve the goals and designs. Thus the aim of the thesis is to identify what goals are important for AWE airfoils, and secondary what kind of effects a tether has on airfoil design.

For the optimisation of airfoils the code known as OptiFlow[1] will be used developed at Delft University of Technology. OptiFlow is a multi-objective optimiser that optimises for two goals. It uses the parametric geometry representation method CST[2] to transform airfoil shapes to a set of design parameters. These parameters are used in the genetic algorithm NSGA-II[3] to generate random airfoils. The flow solver Rfoil[4] is then used to calculate the properties of the airfoils. Based upon these properties, scores for the two design goals are assigned to each airfoil. The optimised airfoils with the best scores are presented in a Pareto Front.

As a starting point of the design phase existing airfoils and their design methods where investigated. These airfoils ranged from the well known NACA series to recent designs, such as the wind turbine specific airfoils of Delft University of Technology. For the first designs of this thesis power production and building height were set as goals. These goals were defined using Loyd's crosswind kite derivations and simple reasoning, which resulted in a ratio of lift cubed over drag squared for power production and maximum thickness for building height. The designs based upon these goals were computed with semi-laminar flow which resulted in relatively thick airfoils with their maximum thickness at 40% of the chord. These airfoils showed maximum lift coefficients of 1.5 around angles of attack of 5 degrees, with low drag values in the order of 0.005.

Based upon the first results a tether was introduced into the model with regards to the goal of power production. This tether was introduced with the help of an estimation by Houska and Diehl[5], which resulted in an updated ratio of lift cubed divided by the square of airfoil *and* cable drag. This updated ratio was used to optimise new airfoils. The results from this optimisation showed airfoils with maximum thickness at 30% of the chord. The maximum lift coefficient increased towards 1.8 at higher angles of attack of 10 degrees and drag increased up to values of 0.01.

Conventional wind turbine design was then used as inspiration to determine a third design goal. Due to the importance of minimising downtime, resilience to roughness was chosen as the third goal. This goal was defined by the difference in rough and clean maximum lift coefficients. The designs flowing from the three goals perform as well in fully turbulent flow as in semi-laminar flow, and feature maximum thickness at 20% of the chord. The maximum lift coefficient increased to values of 2.2 at 15 degrees angle of attack. Similarly the drag coefficient also increased rapidly, up to 0.015.

To improve control, which is beneficial for the prototyping phase as less effort would be needed for the development of control systems, airfoils were designed by constraining the moment coefficient to be constant for the linear region. These final airfoils showed maximum thickness at 20% to 30% of the chord depending on the desired moment coefficient. However the maximum lift coefficient dropped to values of 1.6 and 1.8, with drag values between 0.01 and 0.015. Thus focusing on easy control in the final designs resulted in a loss of lift without a reduction in drag.

It was found over the course of this thesis that cable drag tended to dominate airfoil drag, resulting in high lift designs with high drag. Furthermore when looking at turbulent flow it was found that the best airfoils were those that only performed at high angles of attack. These airfoils featured separation at low angles of attack and could thus only perform at higher angles.

The high lift airfoils resulting from this thesis feature higher maximum lift coefficient than the existing designs, and the drag of these airfoils is lower. This leads to an increase in energy yield and contributes to the goal of bringing sustainable energy faster to more people.

Contents

Nomenclature

Symbols

A_c	Cable Area	$[m^2]$
A_K	Kite Area	$[m^2]$
AR	Cable to Kite Area Ratio	[-]
b	Circle radius Joukowsky transform	[-]
c	Chord length	$[m]$
C_d	Airfoil Drag Coefficient	[-]
C_D	Kite Drag Coefficient	[-]
$C_{D,C}$	Cable Drag Coefficient	[-]
Cf_{BH}	Cost Function for Building Height	[-]
Cf_C	Composite Cost Function	[-]
Cf_{PP}	Cost Function for Power Production	[-]
Cf_{RR}	Cost Function for Roughness Resilience	[-]
C_l	Airfoil Lift Coefficient	[-]
C_L	Kite Lift Coefficient	[-]
C_{lmax}	Maximum Airfoil Lift Coefficient	[-]
$C_{lmax_{clean}}$	Maximum Airfoil Lift Coefficient in clean conditions	[-]
$C_{lmax_{rough}}$	Maximum Airfoil Lift Coefficient in rough conditions	[-]
C_m	Moment Coefficient	[-]
D	Drag	$[N]$
G_{Eff}	Effective Glide Ratio	[-]
L	Lift	$[N]$
L_h	Horizontal Stabiliser lift	$[N]$
L_w	Wing lift	$[N]$
M_{ac_w}	Moment around the aerodynamic centre of the wing	$[Nm]$
P	Kite Power	$[W]$
s	Circle centre coordinates Joukowsky transform	[-]
t	Thickness	$[m]$
V_w	Wind velocity	$[m/s]$
V_l	Tether reel-out velocity	$[m/s]$
w	Transformed plane Joukowsky transform	[-]
w_i	Summing weight	[-]
x	Chord-wise position	$[m]$
x_h	Distance from centre of gravity to horizontal stabiliser	$[m]$
x_w	Distance from centre of gravity to wing	$[m]$
z	Original plane Joukowsky transform	[-]

α	Angle of Attack	$[^\circ]$
γ	Joukowsky transformation parameter	[-]
λ	Level of compromise	[-]
ρ	Air Density	$[kg/m^3]$

Abbreviations

AWE	Airborne Wind Energy
BH	Building Height
PP	Power Production
RR	Roughness Resilience

Figures

Tables

Introduction

Every year the need for energy increases, with the International Energy Agency[12] estimating that the global energy demand will rise by 30% by 2040. In addition with the agreements of the Paris Accord to reduce gas emissions, constant innovation in the various fields of energy production is required. To meet the growing energy demands while reducing the effect humanity has on global warming, renewable energy sources such as wind energy will be the future of energy production

A new field of study has arisen in Wind Energy known as Airborne Wind Energy (AWE) which may be part of the solution to meet the rising energy demand. AWE is a collective term for many different systems that aims to convert wind energy into electricity. Among these different systems there is one common denominator, namely that the systems make use of one or more autonomous aerial vehicles linked to the ground by one or more tethers. Detailed descriptions of the various systems in AWE can be found in âĂŸAirborne Wind EnergyâĂŹ by Ahrens, Diehl, and Schmehl[13] or in the review by Cherubini et al[6]. Following the terminology used by Cherubini et al[6] this thesis focuses on designs for Ground-Gen and Fly-Gen systems which can be seen in figure 1.1.

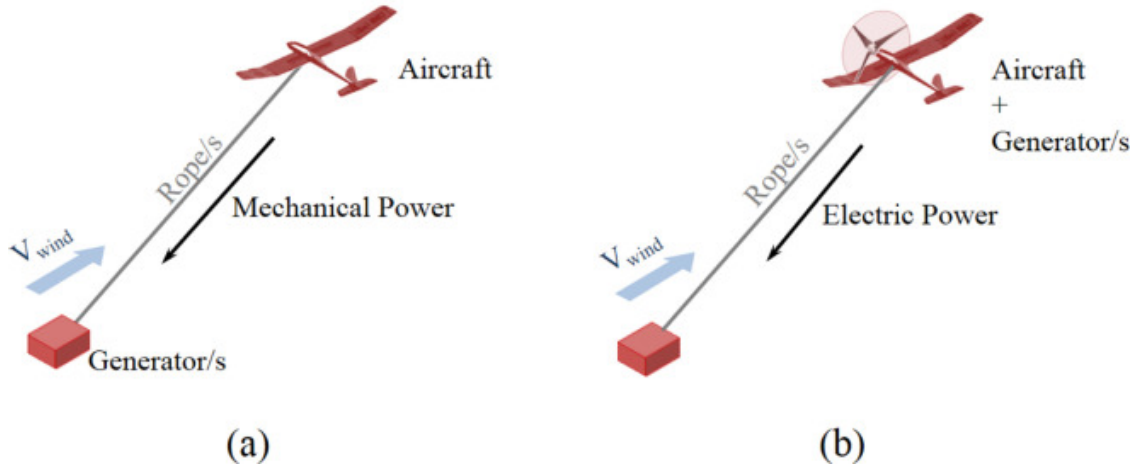

Figure 1.1: *Example of Ground-Gen (a) and Fly-Gen (b) systems.[6]*

The field of AWE is still very new, and companies and research topics in this field change rapidly as a result of the new discoveries still being made. One change that was seen in recent years among multiple companies was that of the transition from a flexible kite to a rigid wing for Ground-Gen systems. One of the reasons for this transition was the extensive knowledge of wing plan-forms and airfoils from standard aircraft and conventional wind turbines.

The different AWE systems all make use of tethered flight. Be it for the transfer of electrical power, mechanical power, or something completely different. Other times when tethers are used by aircraft in flight (outside of AWE systems) are with regards to wildfires, transport, or in-flight refuelling. In all of these situations the tether is relatively short and attached to something that moves along with the aircraft. Whereas for AWE the tether is long and attached to a stationary ground station. When used to transfer mechanical power the tether is also under tension.

It is generally accepted that a tether is a source of aerodynamic drag and weight on the system, but exactly what impact this has on a wing and its components has not been thoroughly researched yet. As such one aim of this thesis is to research the effects of a cable on a wing component (the airfoil). Another aim is to determine what parameters are important for AWE specific airfoils.

In this thesis airfoils will be designed for use in AWE rigid wing systems. The designs are aimed at Ground-Gen systems with rigid wings. As these are simple system that makes use of a rigid wing and a tail, and are well known from standard aircraft. The airfoils will be designed by optimising for two or more goals. Which design goals are of importance for AWE and what kind of airfoils are optimal for these goals will be determined throughout this thesis. In addition the effects of a tether on airfoil design will be investigated.

This thesis is structured as follows. Existing airfoils and their design methods are investigated to provide a deeper insight into airfoils. This is described in chapter 2, together with the optimisation technique that will be used to design airfoils in this thesis. The first airfoils designed for power production and building height in semi-laminar flow are shown in chapter 3. The second set of airfoil designs incorporate a tether and are presented in chapter 4. With initial designs for power production finished the effect of roughness sensitivity is investigated in chapter 5. Following chapter 5 designs purely for turbulent flow are discussed in chapter 6. The main body of this thesis then ends with designs with favourable moment polars in chapter 7. This thesis is rounded off with a final conclusion in chapter 8 and recommendations for future work in chapter 9.

Design Strategy

This chapter will detail the insights gained from a selection of older airfoil designs and design methods. It will also provide a comparison on methods for the synthesis of optimal airfoil designs and which method will be used for the design throughout this thesis. Section 2.1 describes some of the earliest airfoil designs, including the well known NACA series. Section 2.2 presents airfoil designs used on traditional aircraft while section 2.3 shows airfoil designs for wind turbines. Methods for the synthesis of optimal airfoil shapes are introduced and compared in section 2.4. The chapter is rounded off by the code used for optimisation in section 2.5.

2.1 Joukowsky and NACA airfoils

Among the earliest airfoil designs were the Joukowsky airfoils. These airfoils were designed using the Joukowsky transformation in a technique called conformal mapping. With conformal mapping an invertible function is used to map coordinates from a Cartesian reference frame to a curved coordinate system. Allowing airfoil geometries to collapse on to a circle. Analytic solutions of the inviscid flow equations are then available. The Joukowsky transformation is a specific transfer function that maps a circle on to an airfoil shape. The transformation is given in equation 2.1.

$$w(z) = z + \frac{\gamma^2}{z} \tag{2.1}$$

$$\gamma = b + |s| \tag{2.2}$$

Where w is the function of the transformed plane, in this case the airfoil, z the original circle, and γ the transformation parameter that determines the airfoil shape. Both w and z lie in the complex plane. The transformation parameter is given by equation 2.2 where b is the radius of the circle and s the coordinates of the circle centre. The reason that the Joukowsky transformation was used was that the solutions to the flow around the airfoil had to be solved analytically and the solution to a circle or cylinder in an inviscid steady flow was known analytically. Some examples of Joukowsky transformed airfoils are given in Figure 2.1 from Kapania et al.[7]

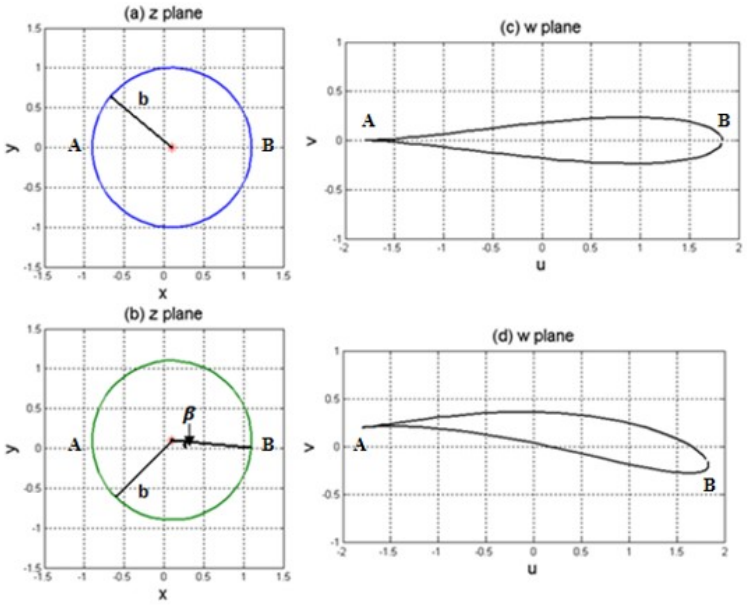

Figure 2.1: *(a) circle in z plane with offset on the x-axis. (b) circle in z plane with offset on x and y with a rotation angle β. (c) Joukowsky transform of a. (d) Joukowsky transform of b. Taken from Kapania et al.[7]*

Perhaps the most well known airfoil family is that of the NACA. These airfoils are widely known from both academic and industrial applications regardless of the age of these airfoils. In "Summary of Airfoil Data"[14] the definitions of many existing NACA airfoils are found. The shapes of NACA airfoils are defined using a mean line camber line and a thickness distribution perpendicular to the mean camber line. With a definition of the airfoil shape the flow around the airfoil had to be calculated to determine the performance. Similar to Joukowsky airfoils this was doing using conformal mapping from a circle but with a transformation that was set up by Theodorsen. The scope and equations of this exact transformation are considered to be too complex for this chapter. However in simple terms the process boils down to adding an extra mapping step. The full process consists of first mapping a circle to an arbitrary circle like shape and then mapping to an airfoil using the Joukowsky transformation. All the calculations for the process can be found in "Summary of Airfoil Data"[14].

Calculating the flow around the airfoil allowed the designers to plot the pressure distributions around the airfoils thus allowing for the study of airfoil variables on the pressure distribution which relates to the forces on an airfoil. For example, from "Summary of Airfoil Data"[14] it was found that increasing thickness resulted in larger pressure differences along most of the chord but smaller differences near the trailing edge. This indicated an increase of maximum velocity over the surface and an increase in relative pressure recovery over the trailing edge as the thickness increased. As the location of minimum pressure along the chord increased, the pressure distribution decreases in magnitude but the pressure recovery region lengthens. This shows that the location of minimum pressure governs the magnitude of the minimum pressure coefficient and the pressure recovery. The effect of camber on the pressure distribution is to separate the pressures on the upper and lower surfaces by an amount that is approximately the same as the design load distribution of the mean line. Furthermore the maximum value of the pressure coefficient on the upper surface increases with the design lift coefficient and for a given design lift coefficient increases with decreasing angle of attack. The result is to cause the critical Mach number at the design lift coefficient to decrease as camber increases.

2.2 Sailplane Airfoils

The NACA airfoils showed that it was possible to relate pressure distributions, with avoidance of flow separation, to airfoil shapes and the need to understand the boundary layer[15]. Since the NACA airfoils better methods for designing airfoils from pressure distributions have been developed. Furthermore methods for calculating characteristics of laminar and turbulent boundary layers have been developed. Laminar separation bubbles have been detected and studied and methods for the potential flow around an airfoil have been developed. With these methods and improved computing power better airfoils than the NACA could be designed with prescribed pressure distributions. Specifically light aircraft and sailplane airfoils by Eppler[8] are looked at. These airfoils are interesting as they can be considered to be the most expressive application of extended laminar flow design principles.

Eppler[8] found that designing an airfoil from a prescribed pressure distribution does lead to certain problems. It is known that the pressure distribution changes with the angle of attack, however when designing for only one angle of attack it can result in different pressure distributions than desired over the entire range of angles of attack. Bowers and Sim[16] agreed with Eppler[8] that laminar separation bubbles[17] become more difficult to account for in the design phase as the angle of attack changes.

When looking at ultralight airplanes it was seen that only the upper part of the airfoil was covered. Which led to airfoils with almost zero thickness and the structure concentrated on the leading edge such as seen in the 368 airfoil by Eppler[8] in figure 2.2. It was desirable to have a high maximum lift coefficient and a gradual stall for takeoff and landing. As such the design goal of airfoils for ultralight airplanes was to exhibit a range of lift coefficients over which the flow is not entirely separated.

From the pressure distribution it can be seen that a high suction peak exists on the lower surface near the leading edge. On the upper surface the suction peak increases as angle of attack increases but it far less sharp. There is a slight concave pressure recovery which together with the rounded upper surface suction peak results in a gradual stall according to Eppler[8].

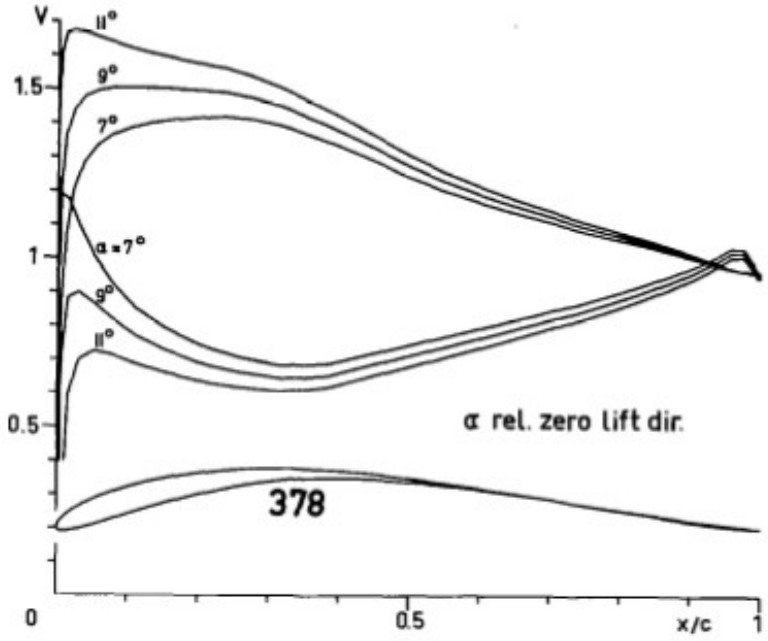

Figure 2.2: *Ultralight airplane airfoil 368 by Eppler[8] with pressure distribution.*

2.3 Wind Turbine Airfoils

The S809 airfoil by Somers[9] was designed using the Eppler Airfoil Design and Analysis Code. The first design goal for this airfoil was to achieve a relatively low maximum lift coefficient of 1 that is restrained due to the limit loads on fixed pitch stall-controlled wind turbines. A derived requirement of this design goal was that the maximum lift coefficient does not decrease due to transition, which was fixed near the leading edge on both surfaces. The second design goal was to obtain low drag coefficient over the range of lift coefficients from 0.2 to 0.8 at a Reynolds number of $2e^6$. Given these design goals a sketch was made of the drag profile as shown in figure 2.3.

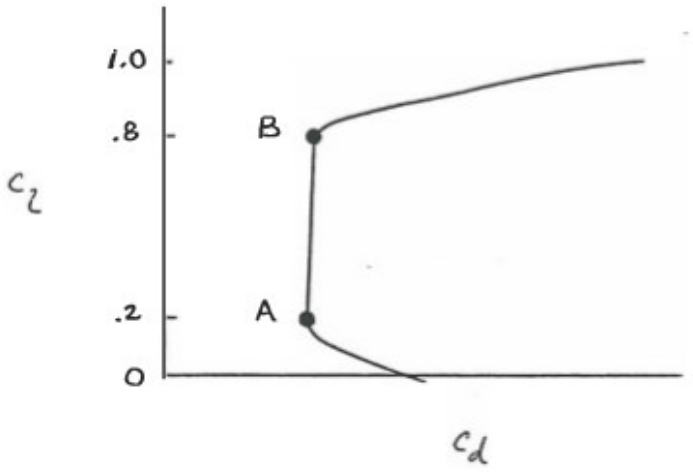

Figure 2.3: *Drag profile sketch of the S809 airfoil by Somers[9].*

Using this sketch Somers[9] related the desired airfoil shape of the S809 to the pressure distributions that occur at the lower and upper limit of the laminar bucket, points A and B respectively. As was seen in figure 2.3 points A and B have similar drag values and are determined by the laminar flow on the upper and lower surface of the airfoil. The drag increases rapidly beyond these points due to the point of transition moving quickly toward the leading edge. This results in a sharp leading edge that produces a suction peak at high

lift coefficients. This peak limits the maximum lift coefficient and ensures early transition as was the design goal. Thus the pressure distributions should look like those in figure 2.4.

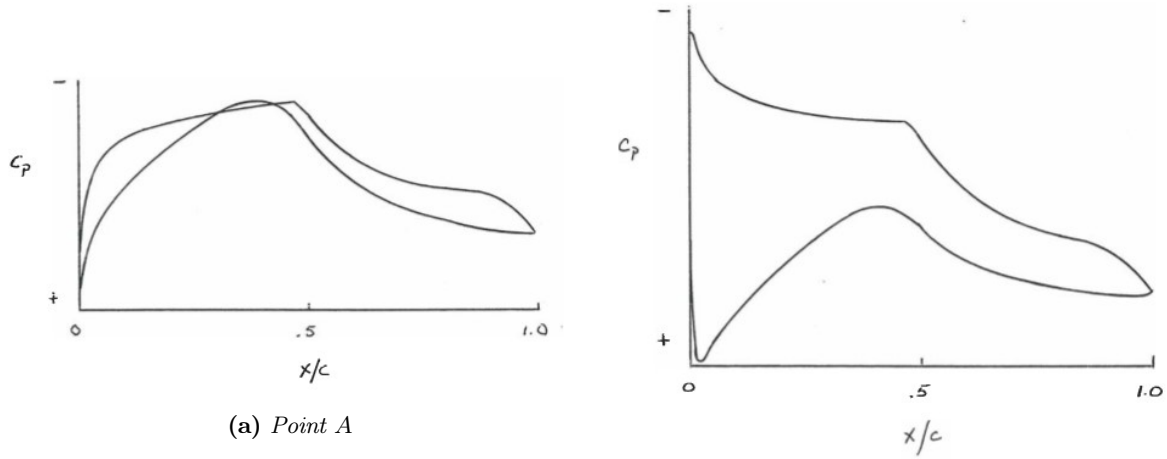

(a) *Point A*

(b) *Point B*

Figure 2.4: *Pressure distribution sketches of the S809 airfoil by Somers[9].*

For low drag at point A it is desirable to have a favourable pressure gradient along the upper surface up to the 0.5 chord length point. Just aft of this point a short region of adverse pressure gradient known as the transition ramp is desirable to ensure a favourable transition from laminar to turbulent flow. As such the initial slope of the pressure recovery is shallow. This transition ramp is then followed by a steep concave pressure recovery region that produces the low drag desired and has a lower tendency to separate. Furthermore a favourable pressure gradient is desired along the lower surface up to 0.4 chord length for low drag. Also to inhibit the formation of large laminar separation bubbles Somers[9] made the initial slope of the pressure recovery on the lower side very shallow. For point B the suction peak does not occur exactly at the leading edge but slightly past it. This is due to incorporating a favourable pressure gradient towards the leading edge which allows for a wider laminar bucket to be achieved. Other airfoils that were developed by Somers and Tangler[18] such as the S825 and S826 also used such an inverse method of determining a desirable pressure distribution and tailoring an airfoil to achieve these distributions.

The DU Wind Turbine airfoils were designed using Xfoil[19] and later on Rfoil[20][4], an updated version of Xfoil, that can take into account rotational effects. Timmer and van Rooij[10] write how the airfoils were designed with the main goal of reducing roughness sensitivity. This is because during their design the most commonly used airfoils were from the NACA 6 series which were very sensitive in performance due to leading edge soiling. These airfoils were designed by adjusting existing NACA series such as the 63-4xx series. As such these airfoils were designed by setting specific goals and then using Xfoil/Rfoil to analyse the flow and change the airfoil in an iterative manner. The goals that were consistent across the airfoils were, high $C_{l,max}$ of around 1.5, thick trailing edges between 0.5% to 1.5% of the chord length, and resistance to soiling. However as written in the paper by Gao et al[21] the resistance to soiling comes with a cost to performance. This is also seen in the paper by Zhang et al[22] where it was seen that, contrary to the high $C_{L,max}$ design goal for the DU airfoil, very thick airfoils in the region of 30% to 40% thickness showed lower lift coefficients due to flow separation. An overlap of several DU Wind Turbine airfoils is given in figure 2.5 in which the thick trailing edges are seen and the broad leading edges of the airfoil that force transition and improve roughness sensitivity. This eliminates the negative effects of a separation bubble occurring naturally. The negative effects from separation are well known and it is often a point of research to improve airfoil behaviour with regards to separation as seen in the papers by Giguére and Selig[23] or by Shah et al[24].

Figure 2.5: *Overlap of DU Wind Turbine airfoils from Timmer and van Rooij[10].*

Important to note is that devices exist that can improve the aerodynamic performances of an airfoil. One of which is a simple vortex generator. A vortex generator can improve stall angle, lift coefficient, and separation. Depending on the position of the vortex generator and the angle of attack the drag coefficient can decrease as seen in the paper by Wang et al[25] or increase as seen in the papers by Manolesos and Voutsinas [26] and Martínez-Filgueira et al[27]. The decrease in drag is only under special circumstances and practical experience teaches that vortex generators generally increase maximum lift and the corresponding angle of attack at the cost of increased drag.

Dahl and Fuglsang[28] write how the RISØ airfoil family was designed using a single point optimisation algorithm. For the algorithm a sequential linear program with move limits was used. This algorithm is simple, robust, and does not take too much computational time. Furthermore Xfoil was used as the aerodynamic panel method for the flow analysis. The RISØ family is a set of seven airfoils with relative airfoil thickness of 12% to 30%. The airfoils are optimised using a objective function which was a weighted sum of lift to drag ratios at angles of attack of 2, 4, 6, 8 and 10 degrees. Furthermore the limits on the lift curve was set to be identical for all the airfoils and the separation points was at a relative chord length of 7% for the three thinnest airfoils and 10% for the other four. This results in a set of airfoils that have near identical aerodynamic performance even with vastly different thicknesses and a good roughness sensitivity due to the early transition points. The family of RISØ airfoils can be seen in figure 2.6.

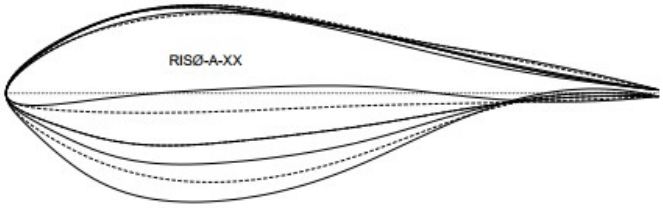

Figure 2.6: *The RISØ airfoil family as seen in Dahl and Fuglsang[11]*

Very little work has yet been done on the design of AWE specific airfoils. In fact as of this writing the only documented cases that have been found are those of Cherubini and Venturato[29] and the presentation of the AWEC 2017 conference by de Oliveira et al[30]. In the case by Cherubini and Venturato[29] the airfoil was designed using a single point optimiser with a genetic algorithm for a performance ratio of C_L^3/C_D^2. However this optimisation did not take into account the drag from a tether and has a lot of room for improvement.

The airfoils by de Oliveira et al[30] were made with a multi-objective optimisation for a variety of airfoil parameters and design goals at fixed C_l. Such as glide ratio, moment coefficient, thickness and resistance to soiling. The designs were also calculated for both free and forced transitions. However, although the effect of a tether was discussed it was not directly taken into account for the simulations.

2.4 Optimisation Techniques

Due to the availability of OptiFlow[1] and the direct supervision of its developer, OptiFlow was set to be the code used in this thesis. However in order to better understand the strengths and weaknesses of the code different optimisation techniques are reviewed. An important distinction to make is that multi-objective optimisation is used and not a single-objective optimisation due to the many parameters involved in airfoil design which naturally favour multi-objective optimisation. Although Mendez et al[31] show it is possible to set up a single-objective optimisation problem for airfoil design by optimising for one goal and setting up constraints for the others, He and Agarwal[32] find that a multi-objective optimisation problem is more suited to dealing with several optimisation goals. Furthermore a multi-objective optimisation allows for better design while taking aerodynamic and structural objectives in to account.

There are multiple different optimisation techniques in existence, however for a multi-objective optimisation there are two well known techniques. These are known as gradient-based optimisation such as used by Carpentieri[33] and genetic-based optimisation used by He and Agarwal[32]. A gradient-based optimisation is deterministic while the genetic-based optimisation is heuristic. In short a gradient-based algorithm uses the gradient of a function to find an optimal solution while the genetic-based algorithm simulates natural evolution to come to an optimum.

Among these options genetic-based algorithms such as NSGA-II[3], MOEA/D[34], and SPEA2[35] are considered the most effective approach to solve a multi-objective optimisation. As the genetic-based algorithm uses a large

gene pool or population size to cover a wider design space it tends to converge more to a global optimum instead of a local optimum unlike a gradient-based algorithm would, who mainly uses local values during calculation. Though it is possible for a genetic algorithm to converge to a local optimum this can be countered by keeping divergent and less- or unfeasible airfoils in the gene pool.[3] Furthermore due to reliance on local values for the gradient-based algorithm well defined initial values would be needed to option a good optimisation. A genetic-based algorithm on the other hand is capable of starting from scratch with random initial values and reach the global optimum although this would increase computational time. This can be alleviated by defining the initial values based on known previous solutions. In the case of airfoil design one could use existing airfoils to define a design space for the initial values.

2.5 OptiFlow

For this thesis the airfoil optimiser known as OptiFlow[1] has been used. It is in a state of constant development and improvement and has been exclusively used for academic purposes since its conception. It has been used for optimal airfoil design for a wide range of applications. Such as Vertical-Axis Wind Turbine airfoils[36][37], conventional Horizontal-Axis Wind Turbine airfoils[38], and airfoils specific for use with plasma actuators[39][40]. A short explanation of the algorithms and models used in OptiFlow will be given here with some of their limitations. However an in depth explanation of the optimiser and the models used can be found in the original MSc. Thesis[1] where OptiFlow was conceived or in a more recent MSc. Thesis by Pieter Dijkstra[41] where it was used for aero-acoustic research.

OptiFlow[1] is a multi-objective optimiser in the MatLab environment that uses a genetic algorithm known as NSGA-II[3]. With multi-objective optimisation it is not possible to obtain only one solution to the set of objectives given. Instead it gives a spectrum of solutions in a Pareto front each of which is a compromise between the objectives. For example, with OptiFLow, which uses two objective functions, one end of the spectrum will be best optimised for one objective function and the other end for the other, with varying degrees of compromise in between. Although this does not result in a single perfect airfoil it provides a set of airfoils from which the best suited airfoil could be chosen depending on the need of an engineer. Logically for optimisation purposes the goal is to maximise something. However OptiFlow requires the objective functions to be structured as a minimisation problem instead of maximisation.

A known issue with NSGA-II[3] is how it represents Pareto fronts. As with most numerical methods it can not represent a true and analytically exact Pareto front.[42] What it does however is display the Pareto front as the largest collection of solutions near the true Pareto front. This has the drawback of not displaying outlying solutions. Thus the Pareto front shown by OptiFlow[1] often does not show the entire range of solutions.

For a genetic algorithm to optimise airfoils a function has to be defined that translates the geometry of an airfoil in to a number of design variables. For this an universal parametric geometry representation method known as CST[2] is used which is capable of representing a variety of aircraft components including airfoils. Kulfan[43] later expanded upon this expanded method allowing it to represent more complex features such as variable camber for airfoil design or flaps.

OptiFlow[1] calculates the properties of an airfoil with the use of Rfoil[4]. There are limitations in Rfoil for the simulation of thick profiles and leading edge soiling. In the paper by van Rooij[20] it is mentioned how Rfoil tends to underestimate the drag of thick profiles by roughly 10%. Furthermore the limitation on leading edge soiling can impact the airfoils to be designed as roughness sensitivity is of great value for conventional wind turbines and might also be for AWE.

Airborne Wind Energy Airfoils

This chapter seeks to determine the goals that AWE airfoils should fulfil and what optimal airfoil fit these goals for a semi-laminar flow. The reasoning used to set up the goals is found in section 3.1. Functions translating these goals into scalar equations are then described in section 3.2. Conditions for the flow that Rfoil requires for calculation are shown in section 3.3. Settings for the simulations are tabulated in section 3.4. The Pareto front showing the spectrum of airfoils is depicted in section 3.5. A selection of airfoils from the Pareto front is then shown in section 3.6 with the pressure distributions and aerodynamic polars in sections 3.7 and 3.8 respectively. Section 3.9 rounds off the chapter by shortly presenting the findings.

3.1 Rationale

The airfoils shown in this chapter were designed by maximising for Power Production (PP) against Building Height (BH). PP is self explanatory as a term and BH is used as a term to describe maximum thickness perpendicular to the chord. BH can also be thought of as the part of the airfoil where the largest structural components could be incorporated such as a spar.

PP was selected for the first goal as for any system that aims to generate electricity the goal is to generate as much energy as efficiently as possible. As a rule of thumb for a wind turbine blade or aircraft wing a thinner airfoil is seen as the better aerodynamic choice while a thicker one is more structurally sound. As such BH was chosen as the second goal. From previous users of OptiFlow[1] it is known that using a thickness based function often results in a well converged Pareto front. Thus using these two goals a spectrum of airfoils ranging from the aerodynamically best performing to the strongest structural shape should present itself.

3.2 Cost Functions

Although the design goals for the first set of airfoils have been determined they cannot be used for optimisation until they are described in the form of cost functions. To optimise for PP the derivation from Loyd[44] will be used. Loyd[44] has written derivations for several models in his original paper including simple kites, crosswind kites, and drag based kites. For the purpose of this thesis the derivation for crosswind kites will be used. The full derivation will not be shown here but from Loyd[44] it can be seen that the lift for a kite in crosswind motion is as shown in equation 3.1. With the corresponding power shown in equation 3.2.

$$L = \frac{1}{2}\rho C_L A_K (V_w - V_l)^2 \left(\frac{L}{D}\right)^2 \tag{3.1}$$

$$P = LV_l \tag{3.2}$$

In equation 3.1 the following variables are used; air density ρ, kite lift coefficient C_L, kite area A_K, free-stream or wind velocity V_w, reel-out velocity of the tether V_l, lift L and drag D of the kite. Looking at equation 3.1 it can be reasoned that the glide ratio of L/D can also be written as C_L/C_D. Thus using equations 3.1 and 3.2 the power of a crosswind kite can be seen to scale with a ratio of $C_L(C_L/C_D)^2$. When assuming that the lift and drag coefficients for an airfoil scale proportionally with those of a finite kite a ratio $C_l(C_l/C_d)^2$ is found instead. This ratio is calculated for a range of airfoil lift coefficients and then weighted and summed which results in the cost function for PP as seen in equation 3.3. With the weights and range of lift coefficients given in table 3.1. This weighted range of lift coefficients is used to ensure that the airfoils have better performance in realistic conditions due to gusts and turbulence which makes the angle of attack a wing or blade experiences fluctuate.

$$Cf_{PP} = \sum_{i=1}^{8} w_i C_{l_i} \left(\frac{C_{l_i}}{C_{d_i}}\right)^2 \tag{3.3}$$

Table 3.1: *Range of airfoil lift coefficients and corresponding weights*

C_{l_i}	0.5	0.6	0.7	0.8	0.9	1.0	1.1	1.2
w_i	0.05	0.1	0.1	0.1	0.1	0.15	0.2	0.2

Equation 3.3 can be used in the airfoil optimisation however, as mentioned in chapter 2, OptiFlow[1] requires the problem to be stated for minimisation instead of maximisation thus the inverse of this function is used.

With PP defined, thanks to the past efforts of Loyd[44], the BH has to be defined as well for optimisation. As mentioned earlier BH is simply defined as the maximum thickness perpendicular to the chord. Another way to see it is as the maximum amount of distance between the suction and pressure side of an airfoil. The location of the BH is not set and can occur anywhere along the chord. The cost function for BH can be seen in equation 3.4 and will be made negative for minimisation.

$$Cf_{BH} = \max_{0 \leq \frac{x}{c} \leq 1} \left(\frac{t}{c} \right) \tag{3.4}$$

3.3 Flow Conditions

In the previous section the functions for optimisation were set up. However, to calculate the coefficients in these functions using Rfoil[4] some properties of the flow have to be known. The flow for this particular optimisation is set to be initially laminar with transition to be free to occur anywhere along the airfoil depending on airfoil shape. To model free transition the artificial transition point of the flow is set at $0.99x/c$ for both the upper and lower sides of the airfoil. With these settings the flow is considered semi-laminar with free transition.

The Reynolds number was set to $6e^6$ for all airfoils computed during this thesis. This number was taken from previous work done by Dijkstra[41] on a wind turbine airfoil. However a quick check was performed to see if this value is also representative for AWE. For this check a kinematic viscosity at sea level of $1.46e^{-5}m^2/s$ was used. Dividing the Reynolds number with the kinematic viscosity a value of around 41 is found. This value should be the product of velocity and length. Which would then be the velocity of the flow the airfoil experiences and the chord length. Often an AWE system flying a circular path is likened to the tip of a conventional wind turbine. Assuming favourable wind conditions based upon conventional wind turbines the free-stream velocity can be estimated to be $10m/s$ and the rotational tip velocity can be set to maximum velocity allowed for onshore applications at $60m/s$. Which roughly leads to a velocity of $61m/s$ that the airfoil experiences. This corresponds of a chord length of approximately $0.7m$. From personal experiences this chord length corresponds to prototypes that are currently in development and have flown at these velocities. As such a Reynolds number of $6e^6$ is a good approximation for flow conditions in AWE applications.

3.4 Simulation Setup

With the conditions for the flow known, settings for the genetic algorithm NSGA-II[3] have to be set up as well. In table 3.2 the settings for the genetic algorithm are shown. In particular the amount of generations and the population size are shown. Where the population size governs the amount of airfoils for each generation and the amount of generations influences convergence. Too little generations will not lead to convergence. The amount of cores used for computational power is also mentioned in the table. The Pareto Fraction and Crossover Fraction are shown together with the Mutation Rate a well. The settings in table 3.2 do not change during the entire thesis with the exception of the population size for chapter 5.

Table 3.2: *Genetic algorithm NSGA-II settings*

Generations	70
Population	200
Cores	4
Pareto Fraction	0.45
Crossover Fraction	0.8
Mutation Rate	0.05

3.5 Pareto Front

The results from the optimisation of the cost functions in section 3.2 can be summarised in a Pareto front, as seen in figure 3.1. A Pareto front is a graph that shows the set of Pareto-optimal airfoils with the goals on the axes. An airfoil is Pareto-optimal if improvement in one goal can only be achieved at the expense of the other goal. The actual values shown on the axes are not of importance as these are adjusted using a simple post function, given between brackets in the figure, to be close in magnitude to each other which gives for easier reading during optimisation.

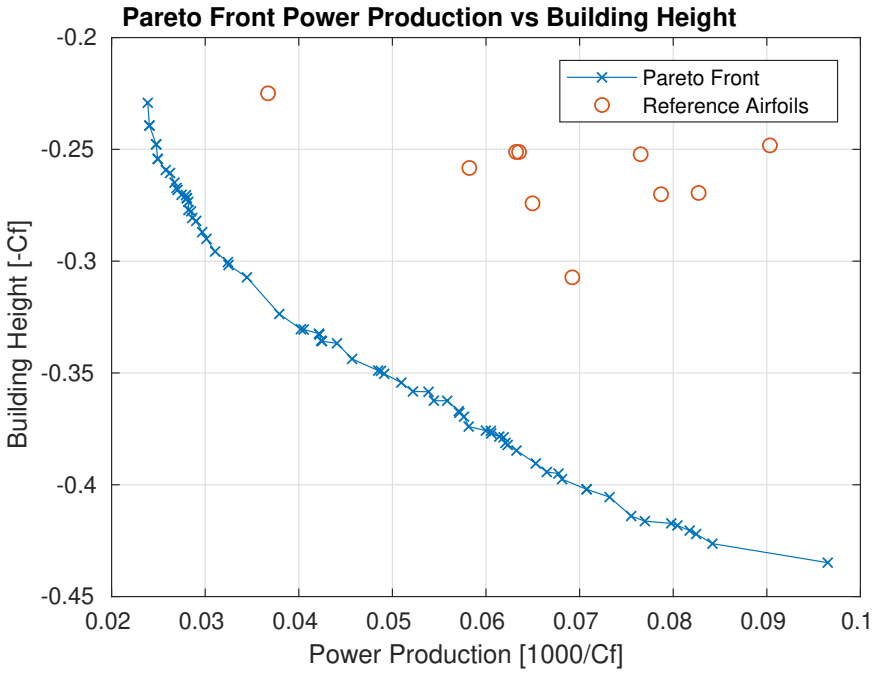

Figure 3.1: *PP vs BH Pareto Front*

The Pareto front shows a curve on which all Pareto-optimal airfoils are found in the design space together with the reference airfoils. In figure 3.1 it can be seen that are 4 reference airfoils with the same BH of 25% with higher values for PP, however remembering that the PP cost function had to be inverted for the optimisation procedure this means that the reference airfoils are performing worse than the optimised airfoil. Seeing that all the reference airfoils in this design space are to the right of the Pareto front it shows that the airfoils serve their purpose in being optimised for PP. Performing better with respect to the defined cost functions when compared to the reference airfoils. The Pareto front shows a large range of airfoils, however a selection of airfoils from the Pareto front will be discussed in detail in the following sections. In particular the airfoils corresponding to 25%, 30%, 35% and 40% thickness were chosen to represent two extremes from the front with intermediate airfoils in between.

3.6 Airfoil Shapes

Several interesting aspects can already be observed by looking at the airfoil shapes. Figure 3.2 shows the shapes of optimal airfoils at 25%, 30%, 35% and 40% thickness. Looking at the 25% to 30% thick airfoils, the thickness increases on both sides of the airfoil but the maximum thickness location does not change. The 35% thick airfoil shows a forward shift in maximum thickness location which can be seen clearest on the pressure side. A small change in the pressure recovery region also starts to be visible at this thickness. This change is more prominent for the 40% thick airfoil. With this airfoil it can be seen that the pressure recovery region has become concave. The maximum thickness location has shifted slightly aft again compared to the 35% thick airfoil but still more forward than the 25% and 30% thick airfoils.

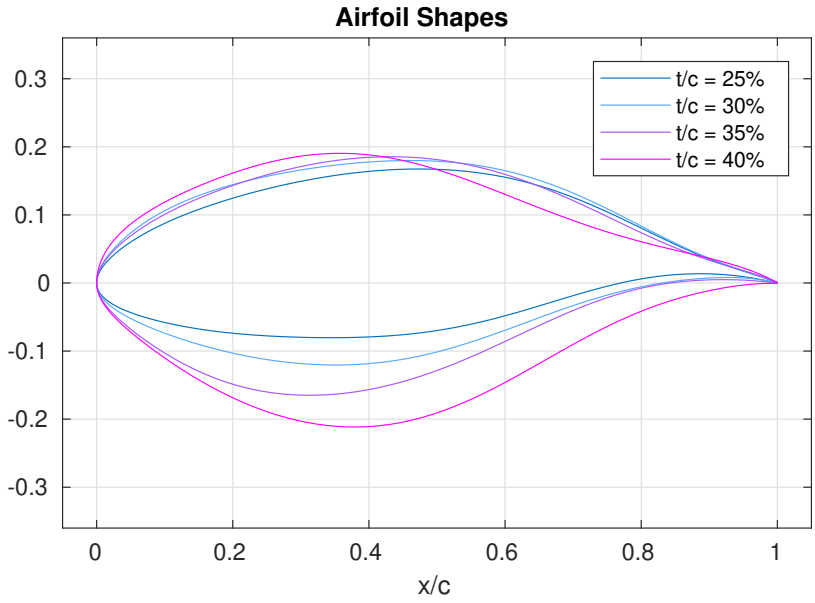

Figure 3.2: *PP vs BH airfoil shapes*

What figure 3.2 shows is that as the thickness increases the point of maximum thickness moves closer to the leading edge. Which at a certain point triggers the pressure recovery region on the suction side to become concave.

3.7 Pressure Distributions

Figure 3.3 shows the pressure distributions of the airfoils from figure 3.2 operating at a lift coefficient (C_l) of 1.2.

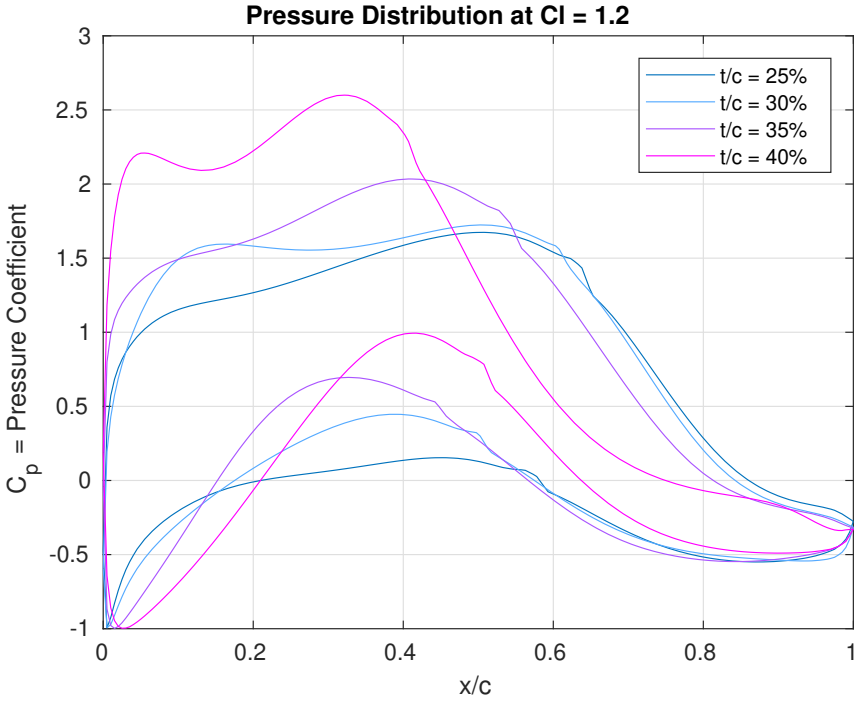

Figure 3.3: *PP vs BH pressure distributions*

It was decided to analyse the pressure distributions at high lifts as these are of the most interest for PP. It can be seen that the 25% and 30% thick airfoils are very similar in pressure along the suction side except for the suction peak at $0.1x/c$ for the 30% thick airfoil. There is also a noticeable difference in the peak at the pressure side.

Both the 35% and 40% thick airfoils show that with the changing point of maximum thickness a forward shift in suction peaks and pressure recovery while the peak on the pressure side keeps increasing. Especially the 40% thick airfoil shows a clear and large shift in suction peak with an extended pressure recovery region. More precisely the pressure recovery starts roughly at a chord position of $0.3x/c$ while the other airfoils start at 0.4 or $0.5x/c$. For these airfoils the pressure recovery starting locations also corresponds to the point of maximum thickness.

3.8 Aerodynamic Polars

The aerodynamic polars are given side by side in figure 3.4. The lift coefficient as a function of angle of attack is given in figure 3.4a and as a function of drag coefficient in figure 3.4b.

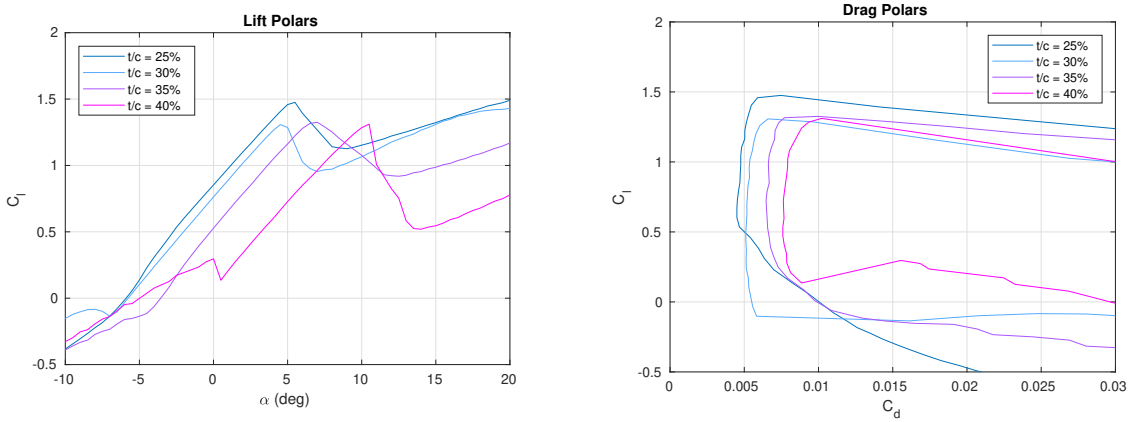

(a) *Lift Polars*

(b) *Drag Polars*

Figure 3.4: *PP vs BH aerodynamic polars*

As expected, observation of the lift and drag polars show that achievable aerodynamic performance decreases when thickness increases. It is shown clearly in the drag polars that with increasing thickness the drag polar worsens as the drag bucket becomes smaller with larger drag values. This can be expected as a larger airfoil simply has more area and thus more wind resistance. Similarly the lift polar worsens as well as the thickness increases. When comparing the 25% thickness curve with the 30% it can be seen clearly that the maximum lift coefficient decreases. However with further increasing thickness the maximum lift coefficient does not decrease but instead shifts towards higher angles of attack. This is due to the larger suction peaks for the thicker airfoils with the forward shift in maximum thickness location. In short the maximum lift coefficient drops down with increasing thickness until the maximum thickness location shift forwards, which moves the maximum lift coefficient to higher angles of attack with more drag. It can also be seen clearly that the 40% airfoil benefits a lot from the given range of lift coefficients in Section 3.2 as the behaviour of the lift polar below 0.5 is not very clean.

3.9 Findings

It can be concluded that, for airfoils optimised for the goals of PP and BH, the aerodynamic performance decreases as the thickness increases unless the maximum point of thickness moves forward. This results in the lift polar shifting towards higher angles of attack with larger drag values.

Interesting to note is that, for AWE systems, some solutions exist to reduce structural loads that are not available for conventional wind energy or aircraft. For example, from personal experience it was found that a bridle can alleviate wing bending by spreading the force from the tether along the wing or to relocate the tether force to the wing tips. Allowing a designer to choose thinner airfoils than usual, which would not be feasible for conventional wind energy or standard aircraft as these do not incorporate tethers. Though a tether and bridle system can have a beneficial effect it is thought that a tether will also have negative effects on an AWE system due to added drag and weight.

Designing for Tethered Flight

In the previous chapter the goal was to optimise for PP in the form of lift cubed divided by drag squared. In this chapter the drag of a tether will be taken in to account for optimal airfoils for PP. The changes that occur in the airfoil designs will then be explained. To take the drag of a tether into account the cost function used for simulation has to be updated in section 4.1. Further constraints on the thickness of the airfoil that were required are explained in section 4.2. The tool of compromise levels are introduced in section 4.3. The effect of increasing tether length on the design space is explained in section 4.4 through a combined Pareto front. Airfoil shapes from the simulations with tethers are shown in section 4.5 and compared to previous results. The corresponding pressure distributions are described in section 4.6. Aerodynamic polars are given in section 4.7 and discussed with regards to chapter 3. The findings on the effect of added tether drag are summarised in section 4.8.

4.1 Tethered Flight Cost Function

To determine the effect of a cable from tethered flight on a wing, the cost functions used for optimisation have to be updated. In particular Cf_{PP} from equation 3.3 will be updated as cable weight and drag are thought to more heavily influence aerodynamic performance. The influence of cable weight and drag on structural performance can simple be countered by choosing a thicker design from the Pareto Front. Thus it is not necessary to update the cost function for BH.

To update the cost function use is made of equation 4.1 proposed by Diehl and Houska[5]. Which states that the effective glide ratio (G^{Eff}) for a kite in tethered flight is a simple function of the lift coefficient of the kite divided by the drag coefficient of the kite and an added estimation for the cable drag. The estimation is based upon the angular momentum of the air friction of the drag of the cable, which can be found in detail in the paper by Diehl and Houska[5].

$$G^{Eff} = \frac{C_L}{C_D + \frac{A_c}{4A_k} C_{D,c}} \tag{4.1}$$

Equation 4.1 shows that the added drag of a cable can be estimated by a simple fraction of the cable area A_c and kite area A_k multiplied by a cable drag coefficient $C_{D,c}$. Equation 4.1 is then rewritten for airfoil parameters using the same assumptions as in section 3.2 and the fraction is simplified to an area ratio AR resulting in equation 4.2.

$$G^{Eff} = \frac{C_l}{C_d + \frac{1}{4} AR C_{D,c}} \tag{4.2}$$

When substituting equation 4.2 in to equation 3.3 the updated cost function for PP is found in equation 4.3.

$$Cf_{PP} = \sum_{i=1}^{8} w_i C_{l_i} \left(\frac{C_{l_i}}{C_{d_i} + \frac{1}{4} AR C_{D,c}} \right)^2 \tag{4.3}$$

From early test runs it was quickly noticed that the added drag tended towards high lift airfoils. As such the range of lift coefficient was increased to the values shown in table 4.1 to accommodate the high lift airfoils. For all simulations performed the cable drag coefficient $C_{D,c}$ was set to 1.1 based of the drag coefficient for a cylinder. This was done as the main focus of the simulations is to compare with existing airfoils and with previous simulations. For practical applications research should be done towards what drag coefficient should be used especially when in conjunction with noise reducers on a cable or other devices that could be attached to a cable.

Table 4.1: *Range of airfoil lift coefficients and corresponding weights for tethered flight*

C_{l_i}	1.0	1.1	1.2	1.3	1.4	1.5	1.6	1.7
w_i	0.05	0.1	0.1	0.1	0.1	0.15	0.2	0.2

4.2 Trailing Edge Constraint

From one of the first test simulations, with added cable drag set at $AR=1$, it was found that the airfoils started to show extremely thin trailing edges. One of these airfoils is shown in figure 4.1 where it can be seen that for the last 10% of the chord the upper and lower curve almost coincide with each other. From a manufacturing point of view this airfoil would be unfeasible as there is hardly any thickness to the trailing edge and thus no structural strength. From an aerodynamic point of view this airfoil could also be seen as a somewhat shorter airfoil going from 0% to 90% of the chord with something that resembles a gurney flap. As such if there method to maintain this particular shape it would have aerodynamic merit. However due to common manufacturing concerns a constraint was constructed to ensure these thin trailing edges would not occur.

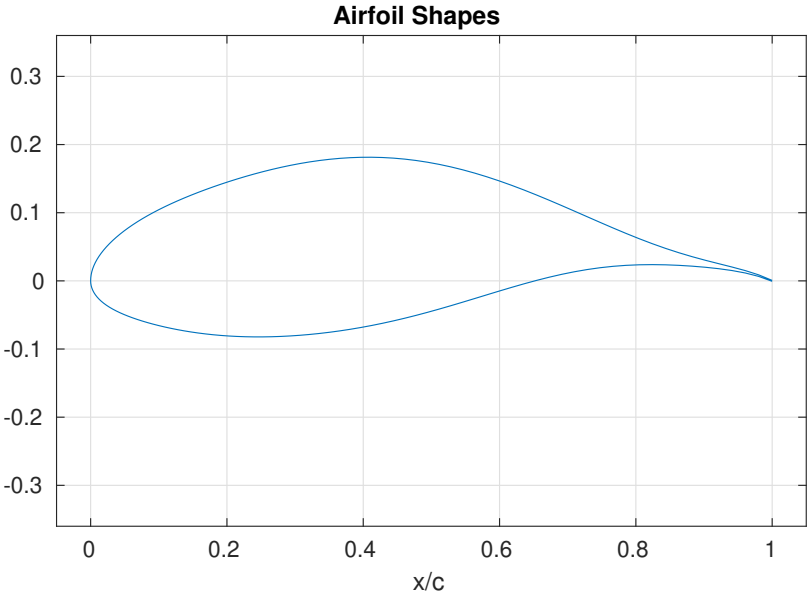

Figure 4.1: *Airfoil shape with thin trailing edge*

The constraint on the trailing edge is implemented as a penalty function. This penalty function is applied to the majority of the simulations from this point on, with the exception being the airfoils in chapter 5. It penalises any airfoil that goes below a certain thickness distribution threshold defined by a reference airfoil. For all simulations with this penalty function the reference was the NACA0006, which was simply chosen for symmetry and thinness. In figure 4.2a the thickness distribution of the NACA0006 is plotted together with the thickness distribution of the airfoil from figure 4.1. In this figure it can be seen that there is some intersection in the last 20% of the chord. When looking closer at the last 20%, as shown in figure 4.2b, it can be seen clearly that around 15% of the example airfoil is below the NACA0006 airfoil. This results in a penalty area that is used to quantify the extent to which the airfoil violates thickness constraint. More specifically a threshold of 10% lower than the NACA0006 is in place at which point the simulated airfoil would be fully discarded and anything in between the threshold and the NACA0006 gains a penalty between 0 and 1 depending on how large the penalty area is.

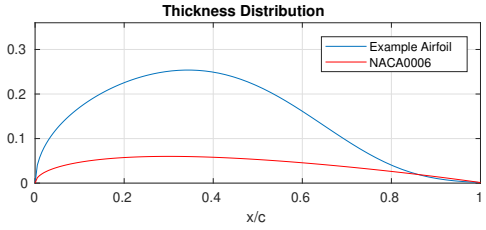

(a) *Full view*

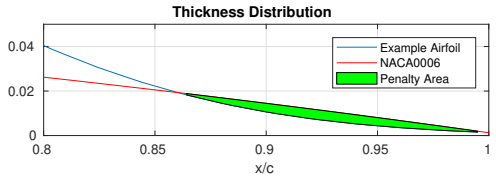

(b) *Close up*

Figure 4.2: *Thickness Distribution of an example airfoil and the NACA0006*

4.3 Compromise Levels

In equation 4.3 the variable AR was used to simplify the ratio between kite are and cable area. By varying AR different cable lengths can be simulated by assuming that cable diameter and kite area stay fixed. In order to analyse the effect of varying cable lengths a new tool to analyse a Pareto front is introduced. This tool is the level of compromise. Levels of compromise represent a certain amount of compromise between the given cost functions. For example for a level of 50% the compromise would be equal between the two cost function. The level of compromise is found by using a composite cost function given in equation 4.4 where λ is the level of compromise. By calculating the composite cost function from equation 4.4 and then determining the minimum (or maximum depending on inverted functions or not) the airfoil corresponding to that level of compromise can be found.

$$Cf_C = (1-\lambda)Cf_{PP} + \lambda Cf_{BH} \tag{4.4}$$

A graphical example of this is given for $AR = 4/3$ in figure 4.3. Where the Pareto front corresponding to $AR = 4/3$ is given together with the composite cost function against airfoil index number n for $\lambda = 15\%$, 30%, and 45%. There were roughly 65 airfoils in this Pareto front. For $\lambda = 15\%$ it looks like the minimum would be around $n = 0$. Which results in the first airfoil from the Pareto front to be taken for a compromise level of 15%. It is also possible that a thinner airfoil not given by the Pareto front would result in a clearer minimum for the composite cost function. But this is not represented in the given Pareto front. For $\lambda = 30\%$ a clearer minimum can be found. Although there seems to be a lot of noise in the graph a clear parabolic trend can be seen which result in a minimum around $n = 35$. For $\lambda = 45\%$ it is again somewhat harder to see if a minimum occurs as the location where the minimum is though to be $n = 60$ is near the end of the Pareto front which only had 65 airfoils in it. If more and thicker airfoils were generated in the Pareto front it would give a clearer picture. However this would require airfoils near 40% thickness which is an extreme value in undesirable in common circumstances.

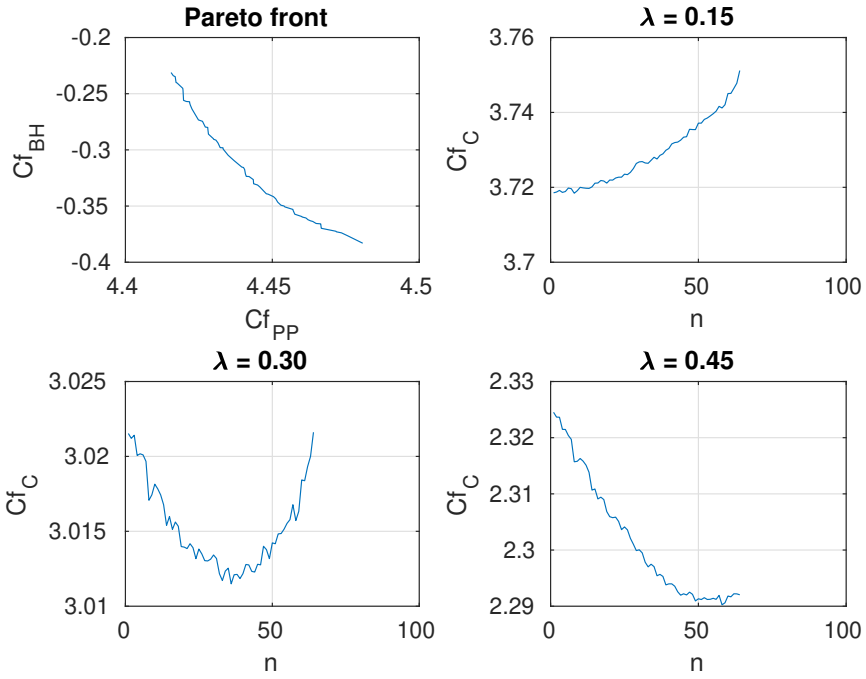

Figure 4.3: *Compromise levels for $AR = 4/3$*

4.4 Pareto Fronts

With the updated cost function from section 4.1 the results from optimisation for several area ratios AR can be seen in figure 4.4. Figure 4.4a shows the original combined Pareto fronts, however in this way it is hard to see the actual shape of each Pareto front due to the differences in magnitude for PP. Thus in figure 4.4b the score values for PP were manipulated in order to get all four Pareto fronts in the same graph without losing their respective shapes. This was done by translating the Pareto fronts for $AR = 2/3$ to $4/3$ to the left by subtracting the values of 0.83, 2.20, and 4.09 from each PP score for $AR = 2/3$, $3/3$, and $4/3$ respectively.

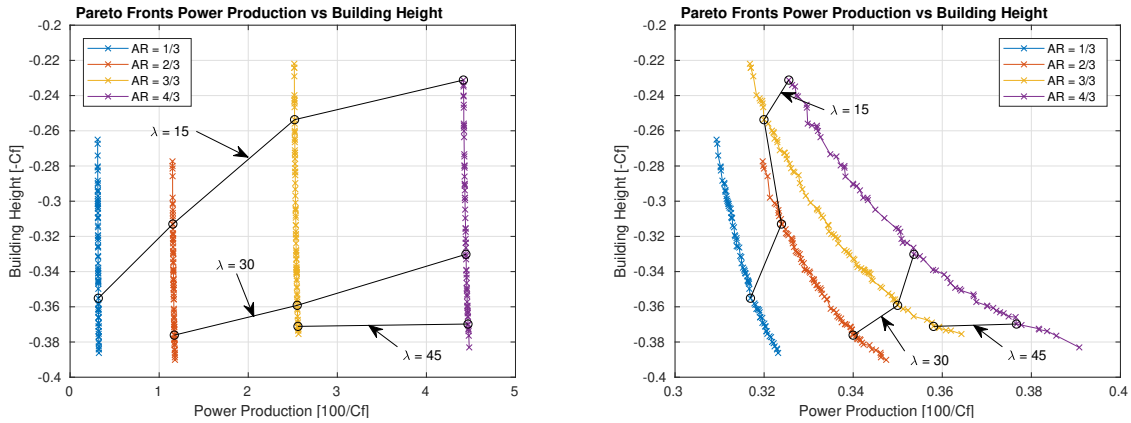

(a) *Original* **(b)** *Translated*

Figure 4.4: *PP vs BH Pareto Fronts for tethered flight*

Furthermore the levels of compromise for 15%, 30%, and 45% are given by the black lines intersecting the Pareto fronts. Interestingly when looking at figure 4.4a it looks like the compromise levels are almost linear in behaviour. The one clear exception to this is due to the compromise level of 15% at $AR{=}4/3$ for which it was not clear if this compromise level existed on the Pareto front. Judging from the apparent linear behaviour of the compromise levels it would indicate that this compromise level should correspond to thinner airfoils not shown on the Pareto front. Similarly for 30% and 45% it can be seen that not all four Pareto fronts show these compromise levels. This is as expected as airfoils past certain thicknesses would be in-feasible and are simply removed from the calculations. For example, the 30% compromise for $AR{=}1/3$ could well be past 40% thickness or more and thus is removed from the calculations as this would result in undesirable behaviour. However, when looking at the levels of compromise it is seen that with increasing AR the level of compromise shifts toward higher index airfoils and higher levels of compromise become available. This could indicate that with increasing AR the possible thickness of airfoils decreases as the cable drag becomes larger compared to the airfoil drag. This could be possible as thinner airfoils generally have better aerodynamic performance and thus to compensate for the increasing cable the airfoil range is pushed to thinner and aerodynamically better shapes.

4.5 Airfoil Shapes

To investigate the effect of tethered flight the airfoils corresponding to $AR{=}1/3$ and $4/3$ are considered in more detail. The shapes for a small selection of these airfoils are given in Figure 4.5. For $AR{=}1/3$ thicknesses of 30% and 35% are shown in figure 4.5a and for $AR{=}4/3$ thicknesses of 25%, 30%, and 35% are shown in figure 4.5b. For $AR{=}1/3$ there is no 25% thick airfoil due to the difficulty NSGA-II[3] has to cover the full Pareto front.

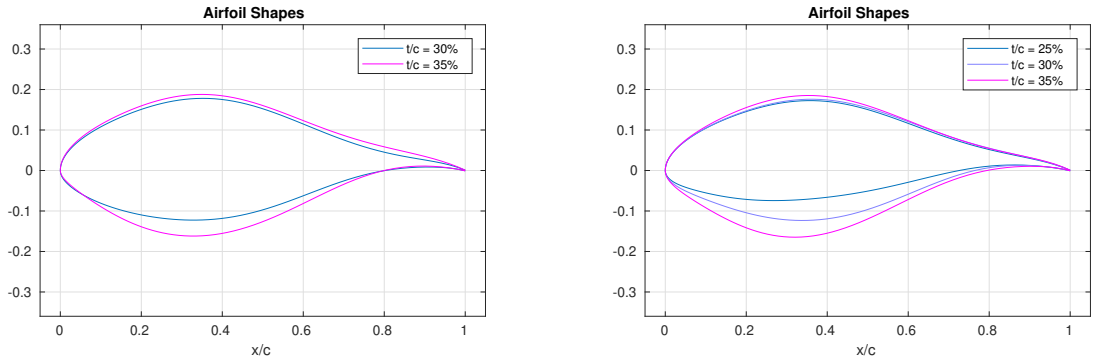

(a) $AR = 1/3$ **(b)** $AR = 4/3$

Figure 4.5: *PP vs BH airfoil shapes for tethered flight*

When comparing the airfoils in figures 4.5a and 4.5b very little difference can be seen. The airfoils corresponding to 30% and 35% thickness are nearly identical to each other. To further investigate the effect of tethered flight

some of the airfoils presented here will be compared to airfoils presented in section 3.6. To distinguish between the different airfoils those from section 3.6 are designated as airfoils for free flight. In particular the 25% and 35% thick airfoils from figures 4.5b and 3.2 will be compared in figure 4.6.

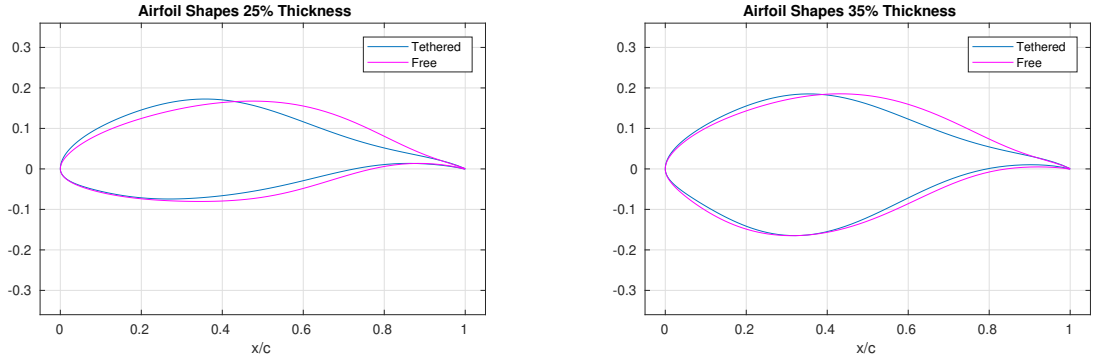

(a) *25%* **(b)** *35%*

Figure 4.6: *Comparison of PP vs BH airfoil shapes for tethered and free flight*

The most noticeable difference between the airfoils for free and tethered flight is the long concave pressure recovery region. This has already been seen before with the 40% thickness airfoil in figure 3.2 in section 3.6. As mentioned in section 3.6 this longer and concave pressure recovery region was indicative of high maximum lift at high angles of attack. Furthermore the leading edge tends to be thicker on the suction side as well for both cases. This is to shift the point of maximum thickness forward. Both airfoils also display a sharper leading edge which for the 25% thick airfoil results in a thinner pressure side and for the 35% thick airfoil the leading edge for 0.2 of the chord is thinner on the pressure side.

4.6 Pressure Distributions

The pressure distributions for the airfoils from figure 4.5 are shown in figure 4.7 operating at $C_l = 1.6$. As expected from the similarities in airfoil shape the pressure distributions for $AR{=}1/3$ and $AR{=}4/3$ are very similar as well. However from the pressure distributions the minute differences can be seen a bit more clearly. The differences show up especially well on the lower curves of the pressure distributions. Figure 4.7b shows a larger pressure peak for the 35% thick airfoil and the 30% thick airfoil which is also slightly shifted forward.

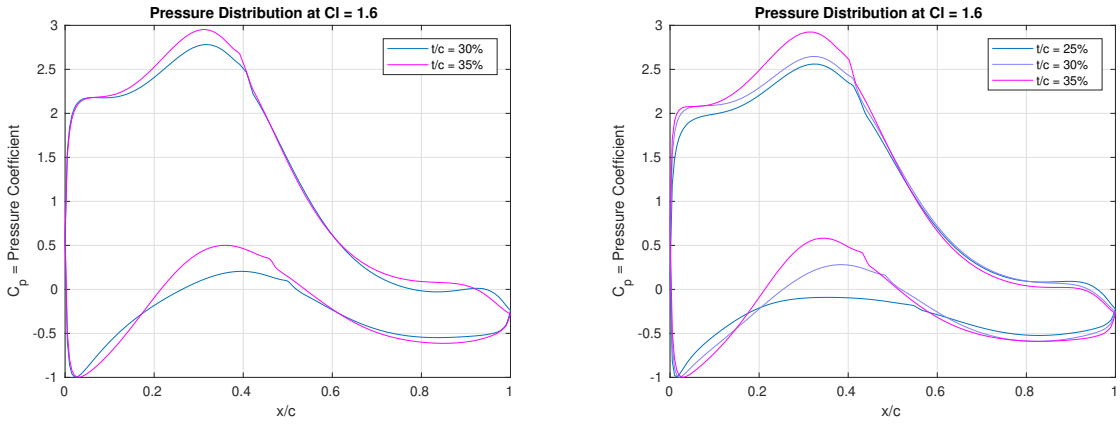

(a) $AR = 1/3$ **(b)** $AR = 4/3$

Figure 4.7: *PP vs BH pressure distributions at $C_l = 1.2$ for tethered flight*

For comparison with the pressure distribution for free flight from section 3.7 the pressure distributions for the 25% and 35% thick airfoils have been calculated for $C_l{=}1.2$ and plotted against their respective counterparts from section 3.7 in figure 4.8.

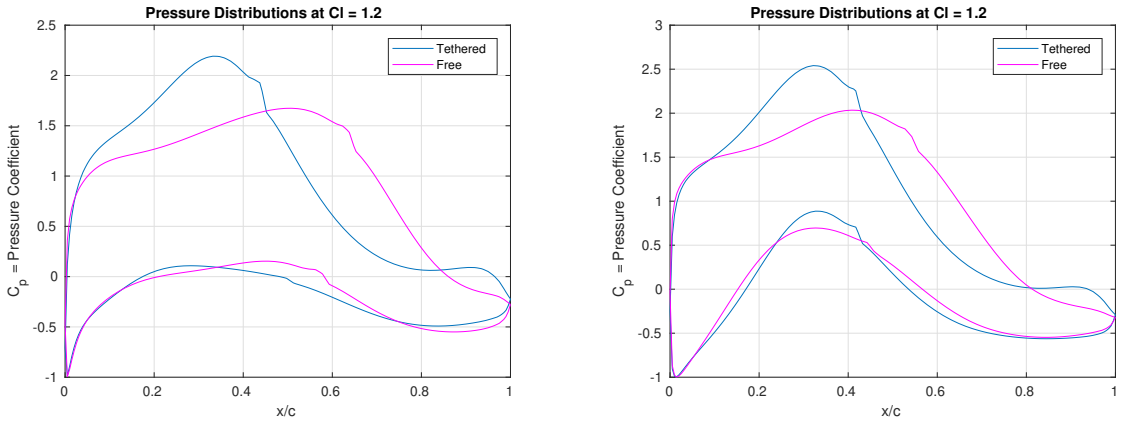

(a) *25%* **(b)** *35%*

Figure 4.8: *Comparison of PP vs BH pressure distributions at $C_l = 1.2$ for tethered and free flight*

Looking at figure 4.8 significantly larger suction peaks on the tethered airfoils can be seen compared to their counterparts. Furthermore the suction peaks are now located slightly after $0.3x/c$ instead of 0.5 and 0.4 for the 25% and 35% thick airfoils respectively. The pressure side is far more similar for the 2 cases. For the 25% thick airfoil the difference in pressure side is very small and can be attributed to how the tethered flight airfoil is thinner on the pressure side from $0.2x/c$ on wards. The difference in pressure peak for the 35% airfoil is due to sharpness of the leading edge on the pressure side. Where the tethered flight airfoil is sharper leading to a larger pressure peak.

4.7 Aerodynamic Polars

The aerodynamic polars for AR=1/3 and 4/3 are given in figures 4.9 and 4.10 respectively. Figures 4.9a and 4.9b show the lift and drag polar respectively for AR=1/3 and figures 4.10a and 4.10b show the same for AR=4/3.

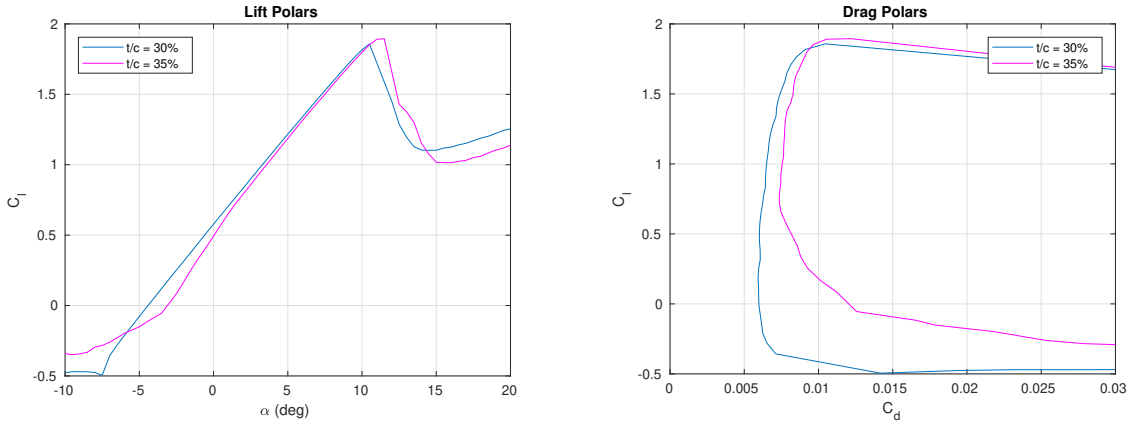

(a) *Lift Polar* **(b)** *Drag Polar*

Figure 4.9: *PP vs BH aerodynamic polars for tethered flight with AR=1/3*

Similar to sections 4.5 and 4.6 the aerodynamic polars show little difference as AR increases. The 25% thick airfoil for AR=4/3 has the best performance as expected due to the lower thickness. When looking at the 30% thick airfoils the difference in lift polars are very small. The maximum lift coefficient is the same but with a slight difference in angle of attack. However when looking at the 35% thick airfoil small differences appear. The small difference in maximum lift coefficient and stall can be attributed to numerical error as calculations near stall are very difficult[1]. The difficulty of calculating stall behaviour imposes inaccuracy on the optimisation procedure. However by focusing the design on lift coefficients in the linear region the optimisation itself is not affected by the inaccuracy. As the lift coefficient at stall is not used in the cost function scores.

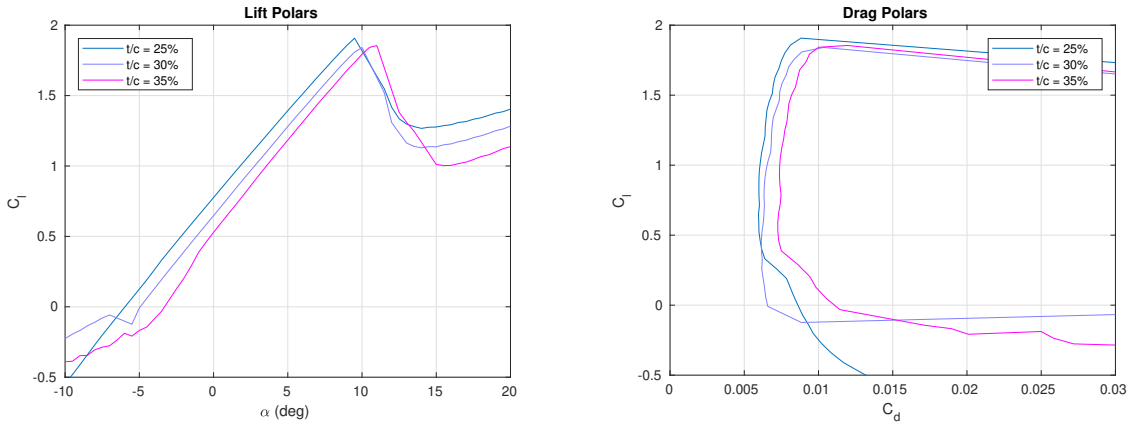

(a) *Lift Polar* **(b)** *Drag Polar*

Figure 4.10: *PP vs BH aerodynamic polars for tethered flight with AR=4/3*

When looking at the drag it can be seen that for AR=4/3 the drag is worse than for AR=1/3. Although this is most obvious for low lift coefficients below 0.5 this will be taken out of account as the range of lift coefficients given in table 4.1 do not take low lift coefficients into account. However, upon close inspection of the drag at high lift coefficients it can be seen that both 30% and 35% thick airfoils have similar drag at AR=4/3 when compared to AR=1/3. This agrees with the small differences seen in the lift polars.

Figure 4.11 shows aerodynamic polars for tethered flight together with polars from section 3.8 for comparison. Figures 4.11a and 4.11b shows the lift and drag polars for the 25% thick airfoils and figures 4.11c and 4.11d shows the polars for 35% thickness.

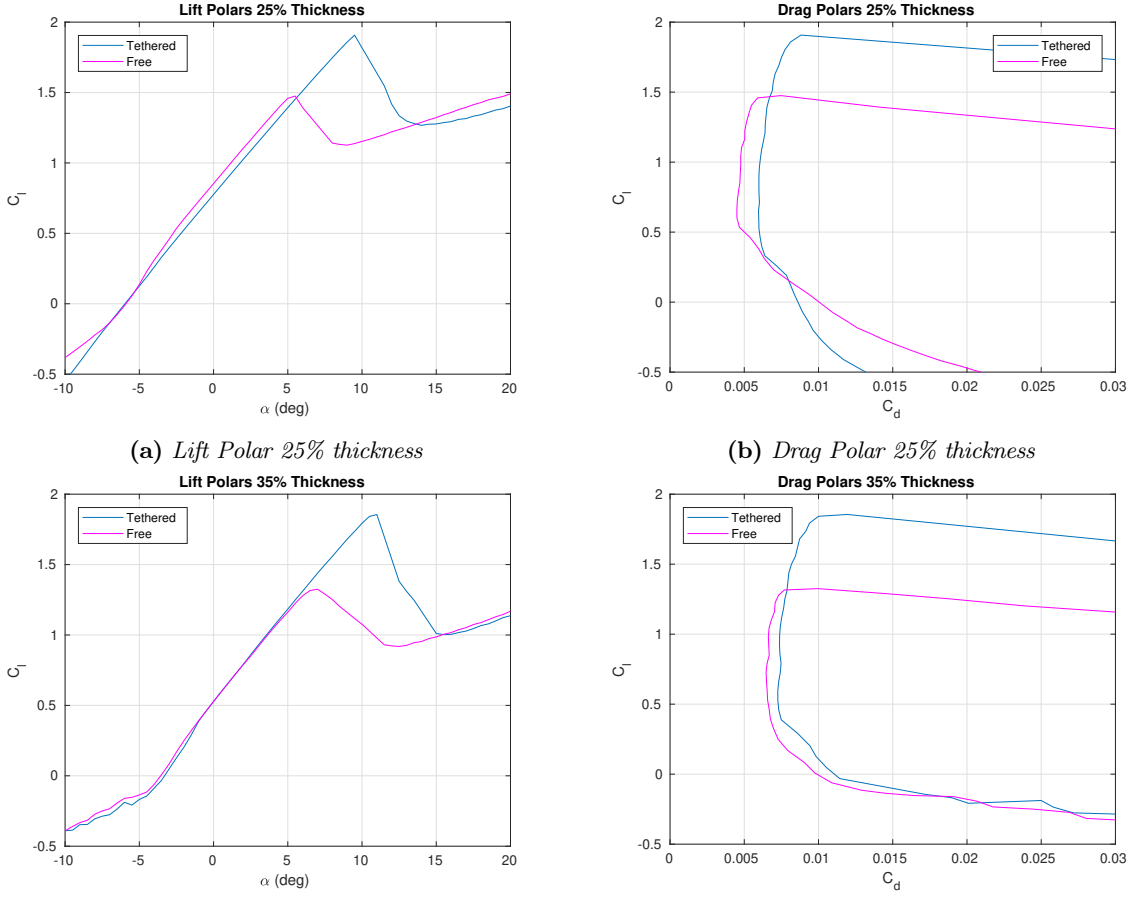

(a) *Lift Polar 25% thickness* **(b)** *Drag Polar 25% thickness*

(c) *Lift Polar 35% thickness* **(d)** *Drag Polar 35% thickness*

Figure 4.11: *Comparison of PP vs BH aerodynamic polars for tethered and free flight*

Differences between tethered and free flight designs are very clear. In both cases tethered flight airfoils display far higher lift and the maximum lift difference reaches 0.5 at higher angles of attack. The drag polars between tethered and free flight airfoils are also different. The maximum lift over drag points are also shifted by around 0.5 on the C_l axis. However the points are also shifted towards higher drag. For example the drag coefficient at maximum lift for the 25% thick airfoil is roughly 0.009 for tethered flight but 0.006 for free flight. The same occurs for the 35% thick airfoil but with values of 0.01 and 0.007 instead.

4.8 Findings

From several comparisons between tethered and free flight it can be seen that the added drag from a tether pushes the airfoil design space towards thinner airfoils with higher lift. Airfoil drag becomes less important due to tether drag being incorporated and high lift is required to compensate for the increased total drag. This results in airfoil designs all featuring maximum thickness locations near the leading edge and concave pressure recovery regions. These airfoils have larger pressure differences at the leading edge for higher lift capabilities.

These designs are Pareto-optimal for PP but airfoil design is multidisciplinary. Other goals should also be taken in to account for AWE airfoils. One of which is resistance to leading edge soiling.

Designing for Roughness Resilience

In this chapter the goal of resistance to leading edge soiling is considered for airfoil design. Resistance to leading edge soiling is shortened to Roughness Resilience (RR). Some of the airfoils presented in this chapter are designed while considering the effect of tether drag on the system, while others are not. Section 5.1 shortly describes why RR was considered. The function for RR is shown in section 5.2. Pareto fronts, for both with and without a tether, are shown in section 5.3. Airfoil shapes corresponding to these Pareto fronts can be found in section 5.4. The pressure distributions are then found in section 5.5 and the aerodynamic polars in section 5.6. The chapter is concluded with the findings in section 5.7.

5.1 Rationale

RR is an important design consideration for conventional wind turbine airfoils, so it is expected that it will be important for AWE systems as well. This is because soiling of leading edges, often caused by ice or contaminations due to bugs and dirt, accelerates transition[45] from laminar to turbulent flow. Figure 5.1 illustrates this phenomenon.

For conventional wind turbines keeping the blades clean from ice and contaminations is a difficult and costly task due to having to shutdown the turbine and the blades themselves are up high and hard to reach. Having airfoils that show little difference in performance between a clean configuration and rough configuration is desirable in this case.

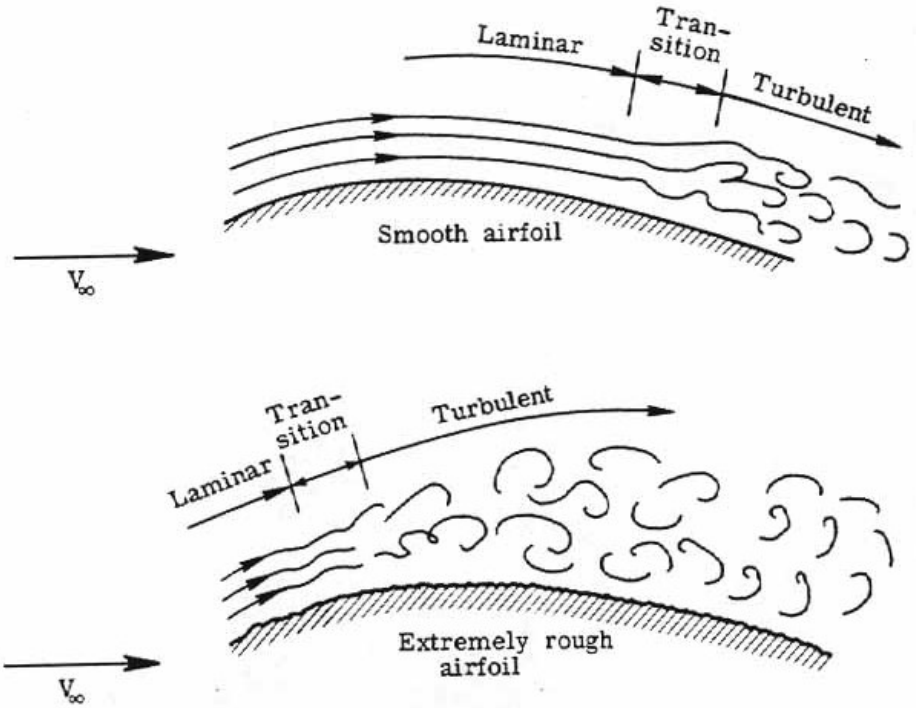

Figure 5.1: *Flow pattern sketches around clean (smooth) and rough airfoils*

The importance of RR remains unclear for AWE systems. This is because of the option of bringing the kite to the ground for maintenance. Which will make cleaning the kite considerable easier when compared to cleaning a wind turbine blade that is high up. The study of RR is relevant nonetheless, because airfoils that are resilient to roughness are also resilient to the substantial manufacturing imperfections encountered on current small scale AWE systems.

5.2 Roughness Resilience Cost Function

In order to design for roughness resilient airfoils a cost function to score this goal has to be set up. The function for RR was defined as the difference in maximum lift coefficient between clean and rough conditions as seen in equation 5.1.

$$Cf_{RR} = C_{lmax_{clean}} - C_{lmax_{rough}} \tag{5.1}$$

The effect of leading edge soiling is simulated by forcing the transition of a laminar flow to a turbulent flow similar to how contaminations would cause early transition. To force the transition for the rough conditions in the calculations the artificial transition point is fixed at $0.05x/c$ and $0.10x/c$ for the suction and pressure side of the airfoil respectively. This is nearly equivalent to imposing that the flow is turbulent over the entire airfoil. For clean conditions the same settings as the free transition mentioned in section 3.3 are used. A Reynolds number of $6e^6$ is prescribed in both cases.

5.3 Pareto Front

Figure 5.2 shows two Pareto fronts. The first front in figure 5.2a was made using the new cost function for RR from equation 5.1 and the updated cost function for PP, described in equation 4.3. The second front in figure 5.2b was made using the same equation for RR but with the old function for PP found in equation 3.3. Thus the second Pareto front does not take the effect of the tether into account. Simulations without a tether were done as it was found during simulations that taking a tether into account resulted in very little solutions and often the airfoils generated showed crossovers between the curves of the suction and pressure side which are not physically possible. This indicated that new solutions were needed to analyse the effect on airfoils when designing for RR. When simulating without a tether it was found that a lot more well converged solutions presented itself for analysis.

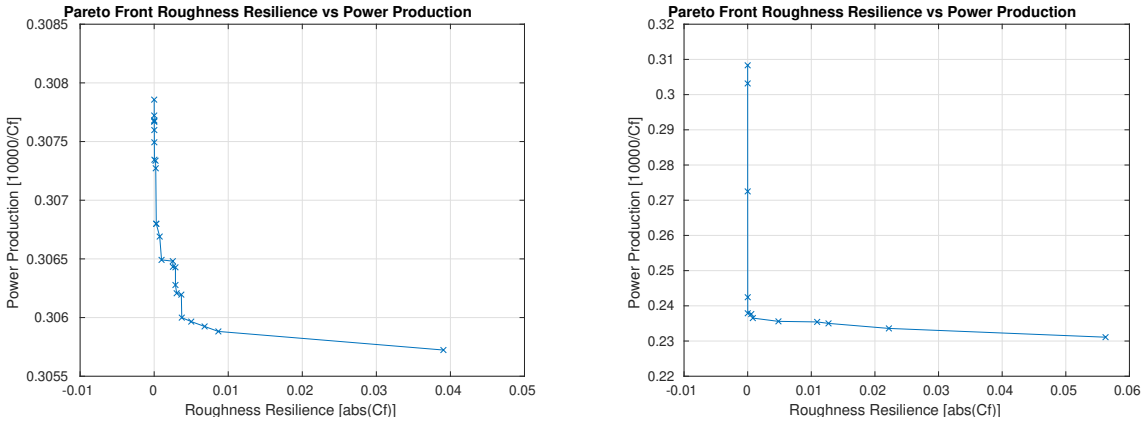

(a) *With tether* **(b)** *Without tether*

Figure 5.2: *RR vs PP Pareto Fronts*

Unlike the Pareto fronts of sections 3.5 and 4.4 the Pareto fronts of figure 5.2 show weak compromises. Both curves are distinctly L-shaped with varying degrees of compromise in the corner. As will be shown in the following sections, and can be seen by looking at the axes of the Pareto front, the compromise in question does show up graphically but is small enough to be negligible. For example when looking at figure 5.2b the highest value on the x-axis for RR is 0.056 which according to equation 5.1 would only mean a difference in C_{lmax} of 0.056. Which for C_{lmax} in the range of 1.3 or higher would results in a difference of less than 5% and for higher C_{lmax} would be less than 5%.

For these Pareto fronts both cost functions of RR and PP can be seen as aerodynamic goals. The function for RR was defined in equation 5.1 as a difference in maximum lift coefficient while the function for PP from section 3.2 was written as $C_l(C_l/C_d)^2$ with an added drag component when taking a tether into account as seen in section 4.1. Thus it can be thought that both functions involve the same goal of obtaining high values for C_l. Whereas before in chapters 3 and 4 there were clear contradictions between the aerodynamic goal of PP and

the structural goal of BH. There cannot be compromise between two goals that aim to achieve similar results. Increase in C_l due to one goal does not lead to a decrease in C_l in the other goal as it is the same parameter.

5.4 Airfoil Shape

As mentioned in the previous section there is very little compromise between the airfoils due to the similarities in the goals for optimisation. A third goal was therefore added to ensure that some compromise between the two goals occurs. This was done by adding a new constraint to the optimisation in the form of fixed thickness. This fixed thickness is at the same time also the maximum thickness of the airfoils and its position was allowed to vary along the chord. Furthermore by running multiple optimisations with varying fixed thickness is it possible to treat the optimisation as if there were three functions to optimise for.

However, when using this fixed thickness in conjunction with a tether it was found that the results worsens. An example of this is given for a fixed thickness of 18% together with $AR{=}1/3$ in figure 5.3. Upon close inspection this airfoil shape shows multiple crossovers at $x/c{=}0.7$ and 0.9. The trailing edge does not even form a closed contour as the ends of the upper and lower curve do not meet at $x/c{=}1$. Furthermore it has extremely high camber and the polars calculated by Rfoil were not converged. As such fixed thickness was discarded for the simulations with a tether.

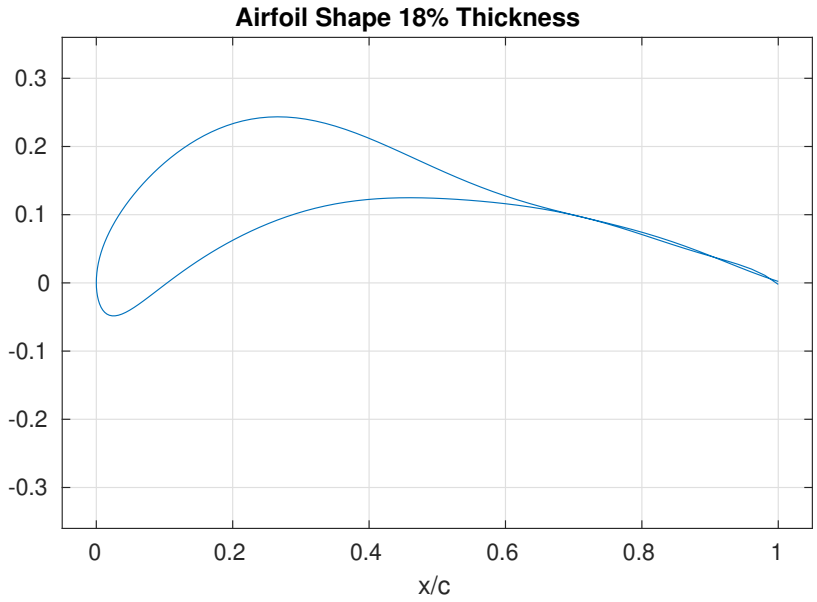

Figure 5.3: *Badly converged RR vs PP airfoil for a fixed thickness of 18% and tether*

Although this shape and others that were similar should be immediately discarded due to being physically unfeasible it is important to note that the shape in figure 5.3 can be likened to that of a leading edge inflatable tube airfoil. Most of the mass is concentrated at the leading edge similar to an inflatable tube and the trailing edge is only a thin line with high camber. A sketch of a leading edge inflatable tube airfoil is given in figure 5.4 for reference. What this signifies though is that there is a link between leading edge inflatable tube kites, used in flexible wing systems for AWE, and the rigid wing systems that are designed for in this thesis.

Figure 5.4: *Sketch of a Leading Edge Inflatable tube airfoil*

Earlier it was mentioned that there is very little compromise between the airfoils due to the similarities in the goals for the optimisation. This can also be seen in figure 5.5 where a selection airfoil shapes is shown. These include airfoils without fixed thickness, named free airfoils here, and with a tether in figure 5.5a. Airfoils without a tether and with fixed thickness of 16%, 18%, and 20% of the chord length are shown in figures 5.5b to 5.5d.

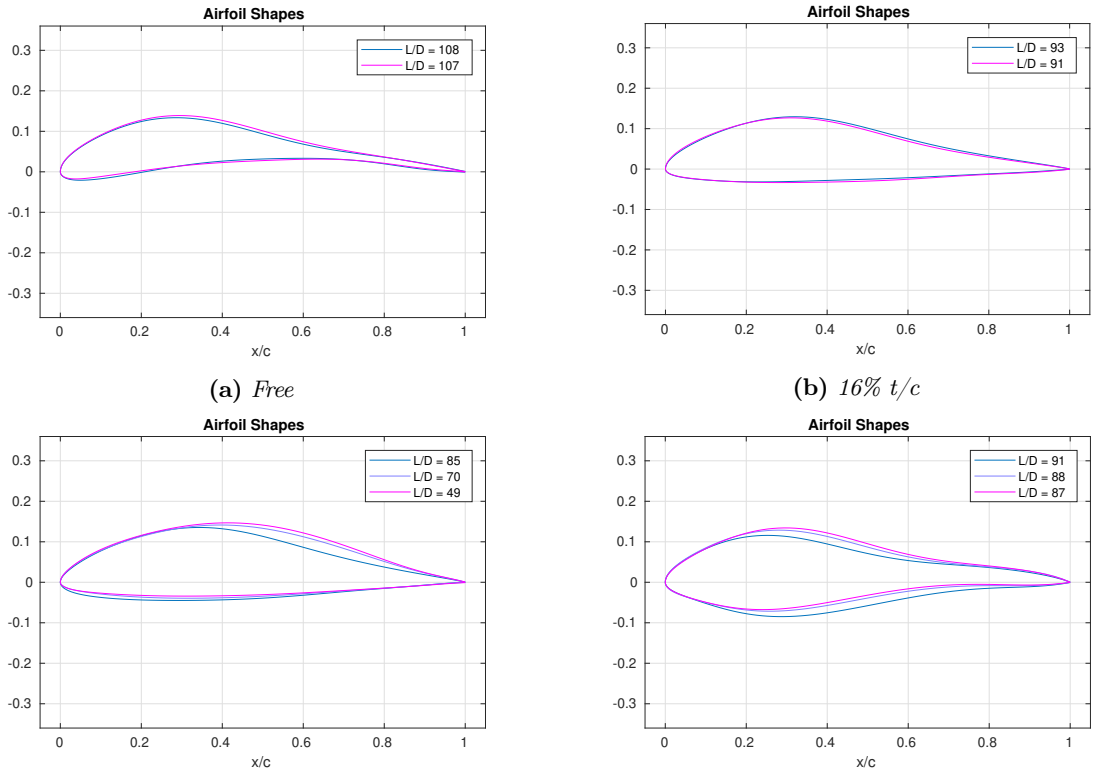

(a) *Free* **(b)** *16% t/c*

(c) *18% t/c* **(d)** *20% t/c*

Figure 5.5: *RR vs PP airfoil shapes for free and fixed thicknesses*

Figure 5.5 contains airfoil shapes with and without a tether in the simulation. In chapter 4 it was concluded that adding a tether tended to shift the location of maximum thickness forward and make the pressure recovery region concave. Interestingly these two characteristics are present in all the shapes shown. The maximum thickness is located in the region $0.2 \leq x/c \leq 0.4$ and the pressure recovery region is concave regardless of a tether being used in the cost function for these RR airfoils.

Figure 5.5a shows tethered airfoils with free thickness. In fact the first and last airfoil given by the Pareto front shown in figure 5.2a are shown. As discussed in section 5.3 very little compromise exists between the two goals and thus hardly any difference between the airfoils exist. Differences on the pressure side at the leading edge and on the suction side at the pressure recovery region are very small. For the airfoils with fixed thickness and without a tether there is little compromise as well but more differences show up especially for thicker airfoils.

In figure 5.5b again only two near identical shapes are shown where the difference is a small decrease in camber leading to a lower glide ratio. In figure 5.5c the first airfoils with clear difference between shapes can be seen. As here the pressure recovery region changes shape significantly and the location of maximum thickness also moves aft. Figure 5.5d shows the first airfoils that also changes in shape on the pressure side as the camber increases together with a slight aft shift of the maximum thickness location.

For further analysis the most similar airfoils among the different fixed thickness are consolidated to generate figure 5.6. These airfoils were chosen based on their shape and location in their respective Pareto fronts. Looking at figure 5.2b this point would be at a RR of 0 and high scores of PP. Or graphically at the top of the L shaped Pareto front.

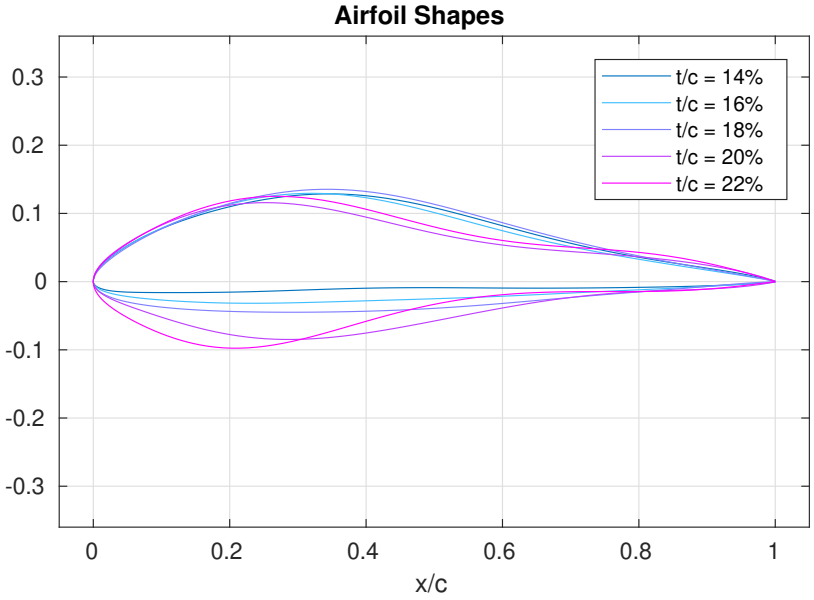

Figure 5.6: *Consolidated RR vs PP airfoil shapes for free flight*

To make figure 5.6 fixed thicknesses of 14%, 16%, 18%, 20% and 22% are used. Similar behaviour as the airfoils shown in section 3.6 can be seen. As the first few airfoils corresponding to 14%, 16%, and 18% only display an increase in thickness along the pressure side. Whereas the airfoils corresponding to 20% and 22% show a large increase in thickness along the pressure side while the pressure recovery region becomes significantly concave with a forward shift in maximum thickness location.

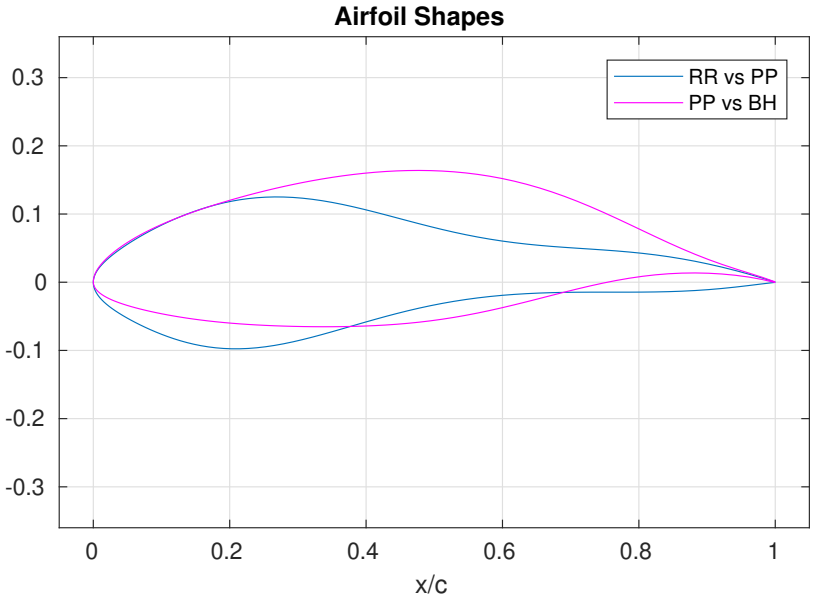

Figure 5.7: *Comparison of RR vs PP and PP vs BH airfoil shapes for free flight*

Figure 5.7 compares airfoil shapes for RR vs PP and PP vs BH from Section 3.6. These designs are similar in thickness as RR vs PP has 22% thickness and PP vs BH has 23% thickness.

It can be seen that there is a very large difference in shape between the new RR airfoil and the older PP airfoil. The two airfoils display very different camber and thickness distributions. There is a difference of about $0.3x/c$ in maximum thickness location. The pressure recovery region is very concave for the RR airfoil and the pressure side of the airfoil also has a large concave region. Considering that the new RR airfoil was optimised using functions for RR and PP these large shape differences are surprising. Although both optimisation cases have one goal that is exactly the same, the RR goal changes the airfoil towards very different shapes.

5.5 Pressure Distributions

In figure 5.8 the pressure distributions for the airfoils operating at $C_l = 1.2$ are shown. These pressure distribution were generated for a turbulent flow over the airfoil as mentioned in section 5.2. As can be inferred from the Pareto fronts in section 5.3 the difference between clean and rough conditions or semi-laminar and turbulent flow are really small. This will be shown later on in this section as well. As such it does not matter whether the pressure distributions are generated with semi-laminar or turbulent flow.

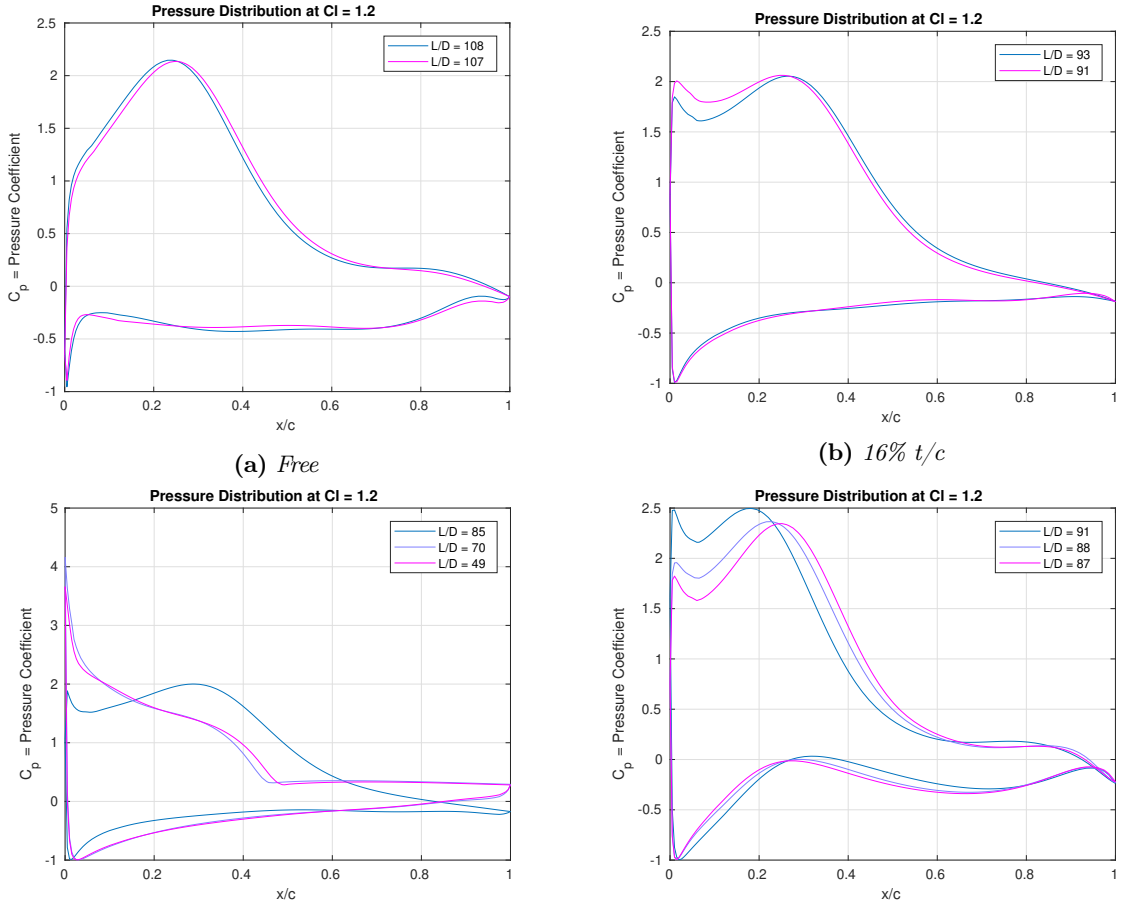

(a) *Free* **(b)** *16% t/c*

(c) *18% t/c* **(d)** *20% t/c*

Figure 5.8: *RR vs PP pressure distributions* $C_l = 1.2$ *for free and fixed thicknesses*

As expected after seeing how little difference there is between the airfoil shapes shown in section 5.4, it can be seen in figure 5.8 that there is also very little difference in pressure distributions. Both the free and 16% thickness pressure distributions show very little difference among their corresponding airfoils. Only for the 18% thickness case in figure 5.8c can a clear difference in pressure distributions be seen as the flow on the suction side of the two airfoils with thicker pressure recovery regions ($L/D = 70$ and 49) seems to separate around $0.5x/c$. For the 20% thickness in figure 5.8d the slight increase in camber and shift of maximum thickness results in a shorter pressure recovery for $L/D = 88$ and 87 with lower maximum pressure coefficients.

Using the same procedure and reasoning as in section 5.4 the pressure distributions, for the similar airfoils as seen in figure 5.6, were plotted together in figure 5.9. Also to prove that the differences between turbulent and semi-laminar flow are indeed very small the pressure distributions were plotted for both flows. This can be seen at a quick glance as the pressure distributions for the two flow conditions are near identical to each other. At most a small difference in magnitude can be spotted at the suction peaks. These are easiest to see for the thicker airfoils of 20% and 22% thickness where there is a difference of around 3% in magnitude.

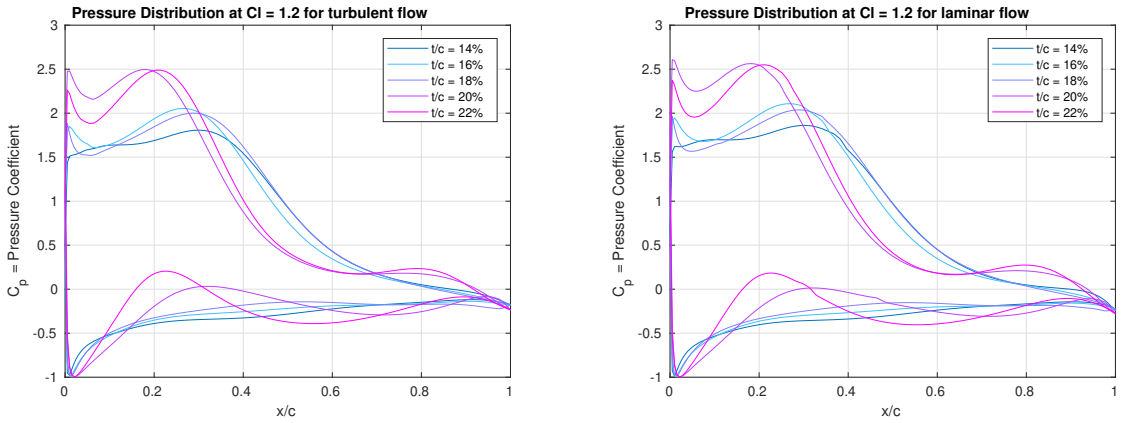

(a) *Turbulent flow* **(b)** *Laminar flow*

Figure 5.9: *Consolidated RR vs PP pressure distributions at* $C_l = 1.2$ *for free flight*

When looking at the pressure distributions in figure 5.9 similar behaviour as in section 3.7 is seen. The pressure distributions corresponding to the 14%, 16%, and 18% thicknesses are very similar with peaks at roughly $0.3x/c$ and a very gradual lower curve. The clearest difference between these thicknesses is seen when comparing 14% thickness with 16% and 18% thickness where the short suction peak at $x/c = 0$ does not occur. This short suction peak seen clearly at 16%, 18%, 20% and 22% thickness is indicative of early transition of the flow. However for 14% thickness it seems that this does not occur as heavily due to the lower thickness. The moment the airfoils change to concave pressure recovery regions, for the thicknesses of 20% and 22%, the peak of the pressure distribution moves toward the trailing edge at $0.2x/c$. Which increases the length of the pressure recovery region. As expected with the shifting of the maximum thickness location toward the leading edge and the corresponding increase in thickness, the peaks for these two airfoils are also higher than the other three. Furthermore the lower curve is no longer gradual but also responds to the increase in leading edge thickness by showing small peaks at $0.3x/c$ and $0.2x/c$ for 20% and 22% thickness respectively.

In figure 5.10 the pressure distributions of the 22% thick airfoil for RR vs PP and the 23% thick airfoil for PP vs BH from section 3.7 are shown together.

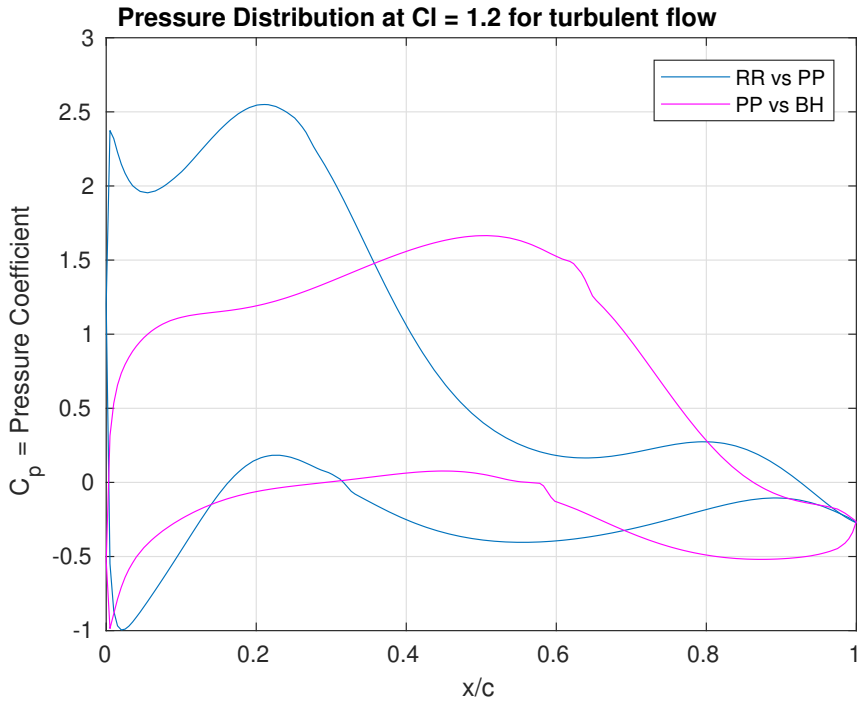

Figure 5.10: *Comparison of RR vs PP and PP vs BH pressure distributions at* $C_l = 1.2$ *for free flight*

As expected from the large differences in airfoil shapes seen earlier the pressure distributions for the two different airfoils are also very different. The suction peaks are both very different in location and in size. Furthermore there is a short peak indicating early transition for the RR airfoil, though this is as expected as a flow with early transition was used in the simulation. As already indicated by the different suction peak locations the pressure recovery regions are different in length. Furthermore the location of the pressure peaks are shifted and for the RR airfoil is more prominent.

5.6 Aerodynamic Polars

The aerodynamic polars are given side by side in figures 5.11 to 5.14. With the lift coefficients given in figures 5.11a to 5.14a as a function of angle of attack and as a function of drag coefficient in figures 5.11b to 5.14b.

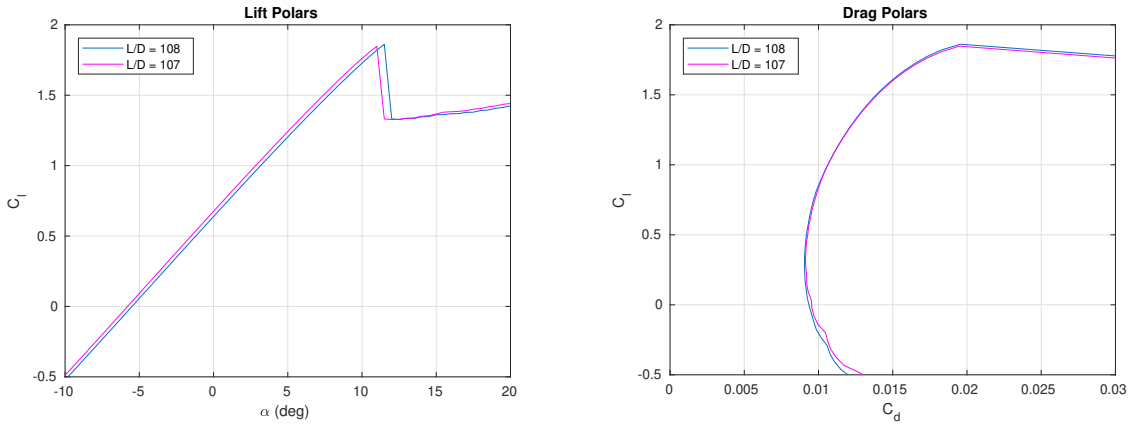

(a) *Lift Polar* **(b)** *Drag Polar*

Figure 5.11: *RR vs PP aerodynamic polars for a tether*

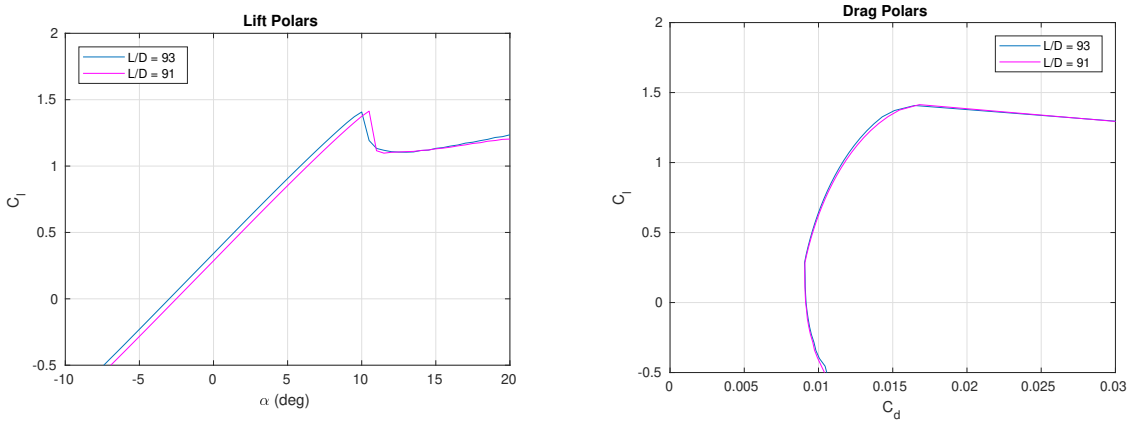

(a) *Lift Polar* **(b)** *Drag Polar*

Figure 5.12: *RR vs PP aerodynamic polars for a fixed maximum thickness of 16%*

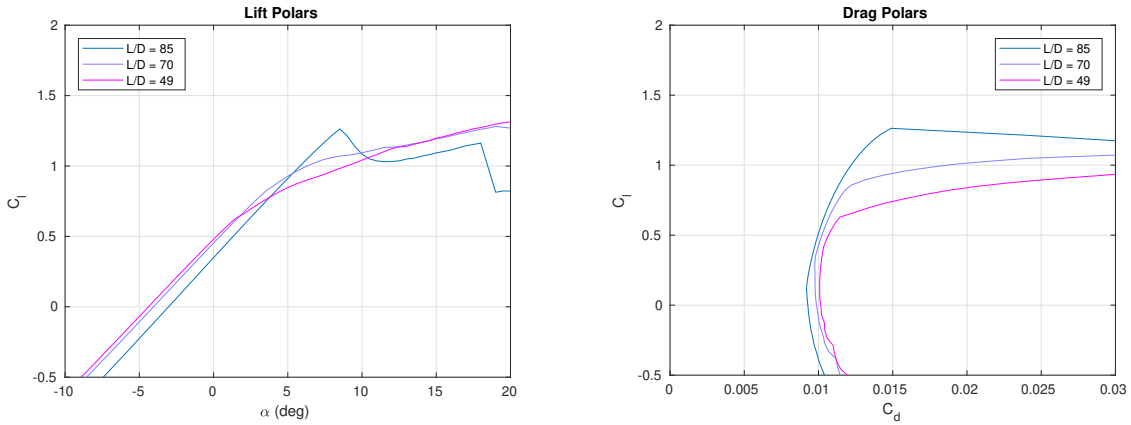

(a) *Lift Polar* **(b)** *Drag Polar*

Figure 5.13: *RR vs PP aerodynamic polars for a fixed maximum thickness of 18%*

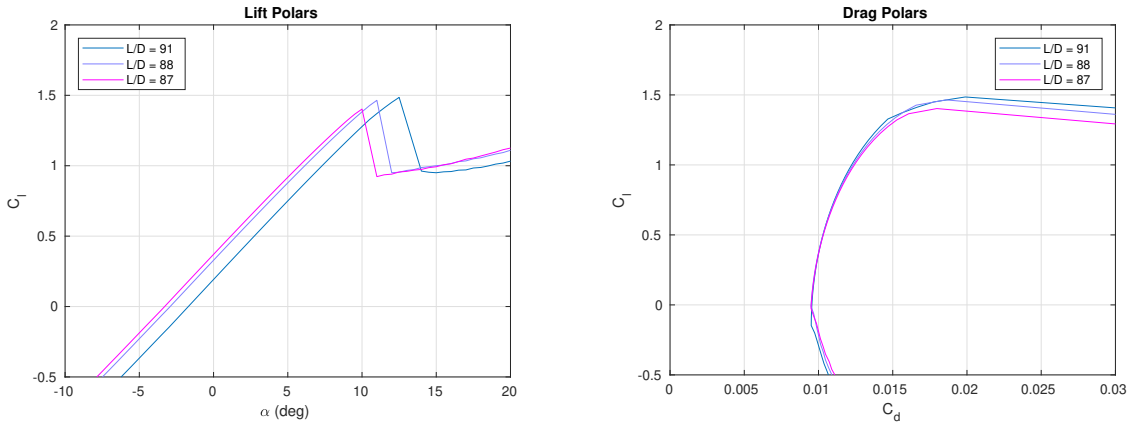

(a) *Lift Polar* **(b)** *Drag Polar*

Figure 5.14: *RR vs PP aerodynamic polars for a fixed maximum thickness of 20%*

Looking at the lift and drag polars there is very little difference between the curves for the tether case in figure 5.11, and the thicknesses of 16% and 20% in figures 5.12 and 5.14. With the tether case having larger lifts and drags as was commented on in section 4.7. The only clear difference is that for 20% the angle of attack for maximum lift coefficient increases as the compromise shifts towards PP. For 18% thickness the aerodynamic polars are interesting. The separations that are seen in figure 5.8b correspond to the stall behaviour shown in the lift polar in figure 5.13a and the increased drag in figure 5.13b.

Consolidating the aerodynamic polars without a tether figure 5.15 is generated. Which shows similar behaviour as seen in section 3.8 but due to the lower thicknesses the lift polars in figure 5.15a show longer linear regions and the drag polars show clean drag buckets in figure 5.15b. In contrast however it does show similar behaviour as in chapter 3 where the airfoils first show a decline in maximum lift coefficient until it increases again only at a higher angle of attack. For the drag polar increasing thickness results in higher drag values across all lift values. The only exception to this is for 18% thickness which shows higher drag values past a C_l of 1 compared to the 20% and 22% thickness.

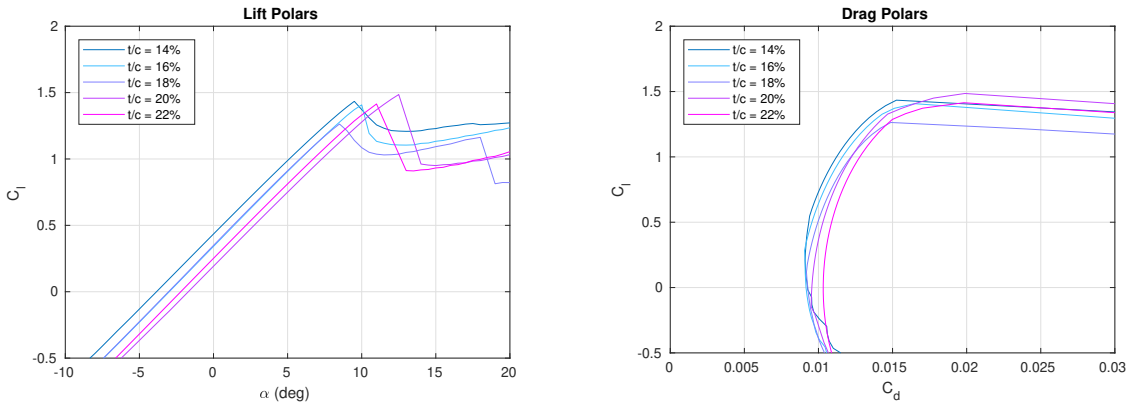

(a) *Lift Polar* **(b)** *Drag Polar*

Figure 5.15: *Consolidated RR vs PP aerodynamic polars for free flight*

In figure 5.16 the aerodynamic polars of the 22% thick airfoil for RR vs PP and 23% thick airfoil for PP vs BH from section 3.8 are shown together. Note that for comparison these polars are for a semi-laminar flow. This leads to a small difference in lift polar but the drag polar shows a clear difference. The difference is caused by the presence of a boundary layer in a turbulent flow which results in higher drag values compared to a semi-laminar flow.

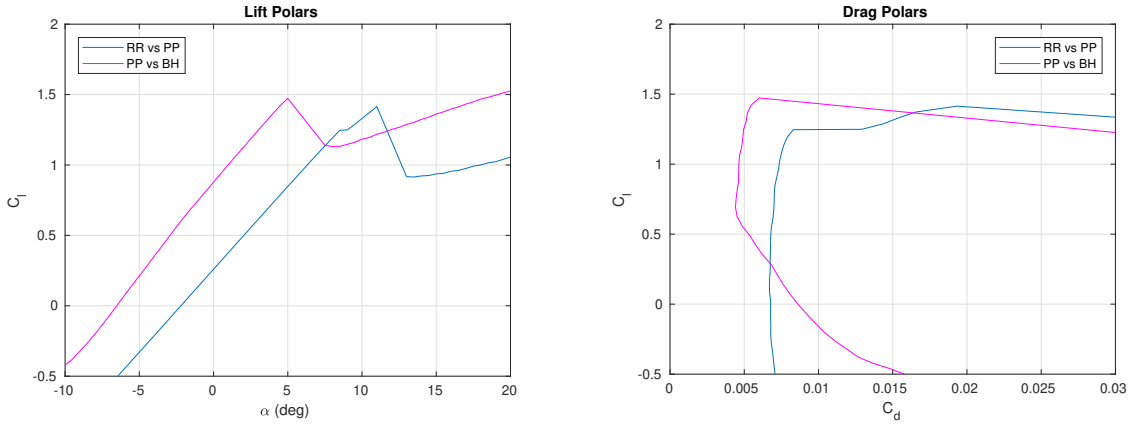

(a) *Lift Polar* **(b)** *Drag Polar*

Figure 5.16: *Comparison of RR vs PP and PP vs BH aerodynamic polars for free flight*

Although there are clear differences between the curves, these are not as large as the differences seen earlier for both the shapes and the pressure distributions. When looking at the lift polars in figure 5.16a the main difference is a shift in angle of attack. But the maximum lift coefficient is very close in value and stall behaviour is similar. The difference in the drag polar are more noticeable where the PP airfoil has better performance for high lift values.

5.7 Findings

The results presented in this chapter show that consideration of RR introduces large differences in the shape and pressure distribution of optimal airfoils. However, the differences in aerodynamic polars are of a smaller scale. Thus it can be concluded that the effect of RR is not very pronounced in phenotype space but it is in genotype space. It was also seen that roughness resilient airfoils exhibit relatively little performance difference between free and forced transition conditions. Thus designing for RR can also be done by designing for rough conditions only, or in other words, by designing for turbulent flow.

However, there were very little solutions when a tether was taken into account for the optimisations with the RR cost function. Thus to obtain airfoils that are resilient to roughness with a tether taken in to account designs in a turbulent flow will be made.

Designing for Turbulent Flow

This chapter will focus on designing airfoils for turbulent flow with a tether incorporated. Thus finding a solution to the convergence problem found in chapter 5 regarding RR and tethers. Section 6.1 details why a design for turbulent flow is generated and which changes to the optimisation have been made for this design. Section 6.2 shows the Pareto fronts of this design set, whereas section 6.3 displays a selection of airfoil shapes from these Pareto fronts. Sections 6.4 and 6.5 detail the pressure distributions and aerodynamic polars respectively. In section 6.6 the airfoils in this chapter are compared with existing airfoils. The chapter is ended with the findings in section 6.7.

6.1 Rationale

As was concluded at the end of chapter 5 it is possible to design for RR by designing for turbulent flow only. By designing for turbulent flow only, computational time can be reduced because it is no longer required to calculate both rough and clean conditions for each airfoil. It was also found in chapter 5 that using the RR cost function in section 5.2 with a tether resulted in several optimisation problems.

Thus by designing for turbulent flow the goal is to circumvent the optimisation problems found earlier in chapter 5 and find airfoils that are not sensitive to rough conditions while having a tether incorporated.

The cost functions and constraints of chapter 4 are recycled. Flow conditions, however are not the same but instead correspond to the rough conditions of chapter 5. Transition is forced at $x/c = 0.05$ and 0.10 for the suction and pressure sides of the airfoil respectively, and a Reynolds number of $6e^6$ is used.

The range of demanded lift coefficients is slightly different. The lower bound of the range was extended in order to produce aerodynamic polars with a longer linear region. The range used can be found in table 6.1. It can be noted that the weights no longer add up to the value 1 in this case but to 0.9. This is an error that was found out near the end of the designs. However due to time limitations it was not possible to redo the simulations that had this error. As such it was chosen to keep this error in the simulations for this chapter.

From a comparison point of view this poses no problem as it only affects the scores of the airfoils used for optimisation. If all scores are equally reduced by 10% it will still converge to the optimal solution, that solution will only have a somewhat smaller value assigned to it. This does not affect the properties of the airfoil, the pressure distributions, and aerodynamic polars will not be changed by this error. The only drawback is that it will be harder to compare the airfoils in this chapter with other airfoils based on score values.

Table 6.1: *Range of airfoil lift coefficients and corresponding weights for tethered flight in turbulent flow*

C_{l_i}	0.5	0.7	0.9	1.1	1.3	1.5	1.7
w_i	0.05	0.1	0.1	0.1	0.15	0.2	0.2

6.2 Pareto Front

Using the same procedure as outlined in section 4.3 the compromise levels for $\lambda = 30\%$ and 45% have been found and plotted in figure 6.1 together with the Pareto fronts for area ratios of $AR = 1/3, 2/3, 3/3$ and $4/3$. In figure 6.1a the Pareto fronts are shown without data manipulations and in figure 6.1b the Pareto fronts with translation. The fronts are translated by subtracting values of 1.20, 3.15, and 5.83 for $AR = 2/3, 3/3$, and $4/3$ respectively from the PP scores. This improves the visualisation of the four fronts.

When looking at figure 4.4a the compromise level lines are not as linear as they were in section 4.4. Instead, the slope decreases clearly with increasing AR for the 30% and 45% lines. Furthermore the compromise levels show similar behaviour as was explained in section 3.5 which could indicate that with increasing AR thicker airfoils are less optimal and thinner airfoils become more desirable. This is completely as expected as the same functions and constraints from chapter 4 were used with only a change in design range of lift coefficients and flow conditions.

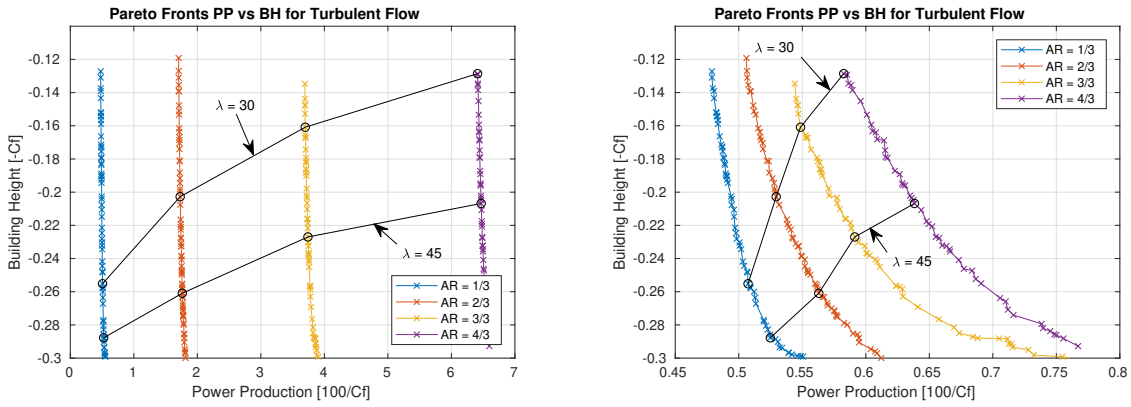

(a) *Original* **(b)** *Translated*

Figure 6.1: *PP vs BH Pareto Fronts for turbulent flow*

The clearest difference between figure 6.1 and figure 4.4 is that the score values for PP in figure 6.1 are higher. This is logical as the airfoils are now designed and calculated for turbulent flow which results in boundary layer growth. The boundary layer increases drag thus decreasing performance and increasing the inverted function scores. The airfoils calculated with semi-laminar flow either do not have a boundary layer when there is no transition or have a smaller boundary layer as the transition occurs further away from the leading edge compared to the forced transition locations of $0.05x/c$ and $0.10x/c$.

6.3 Airfoil Shape

The airfoil shapes for AR=1/3 and 4/3 are chosen for further investigation. The shapes are given in figure 6.2 where AR=1/3 and 4/3 are given in figures 6.2a and 6.2b respectively. Thicknesses of 15%, 20%, and 25% are displayed.

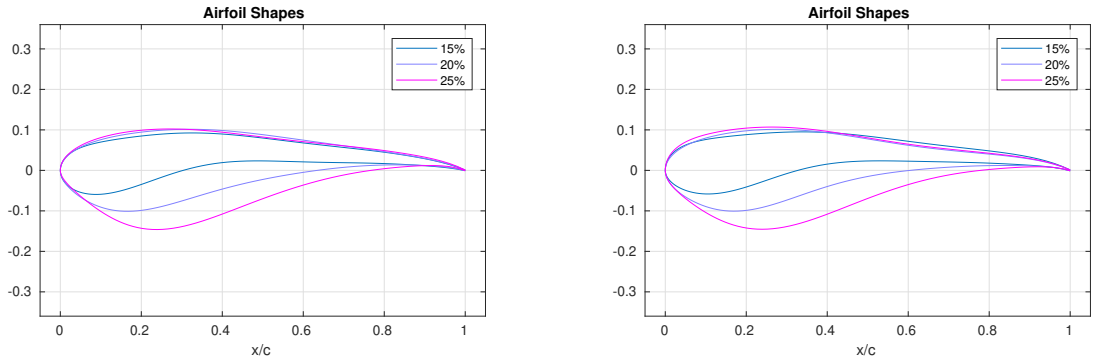

(a) *AR = 1/3* **(b)** *AR = 4/3*

Figure 6.2: *PP vs BH airfoil shapes for turbulent flow*

It can be seen from figure 6.2 that increasing AR has very little influence on the shape of the airfoils. The clearest differences are seen on the suction side for the 25% airfoil in figure 6.2b. Where a small increase in thickness near the leading edge and a small concavity around $0.7x/c$ in the pressure recovery region are visible. Furthermore, similar to the trends observed in section 4.5, all thickness increases occurred on the pressure side of airfoils. Increasing thickness also shifts the point of maximum thickness aft. The suction side hardly changes with increasing thickness and is kept small with a blunt leading edge.

Figure 6.3 compares the 25% thick airfoil from Figure 6.2b to the 25% thick airfoil with AR=4/3 from chapter 4. The airfoil from chapter 4 is designated as semi-laminar, due to the semi-laminar flow conditions, and the airfoil from this chapter is designated as turbulent.

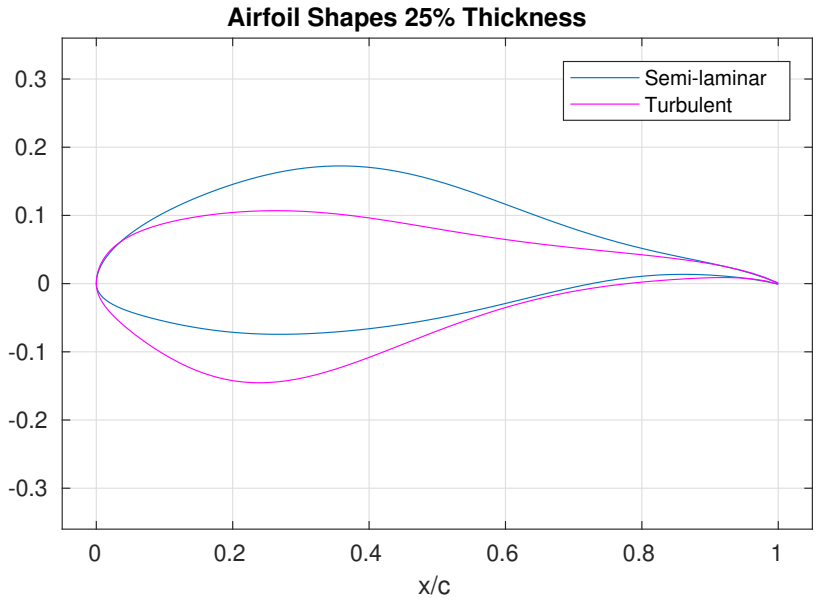

Figure 6.3: *Comparison of PP vs BH airfoil shapes for semi-laminar and turbulent flow*

Interestingly when looking at figure 6.3 it appears that the two airfoils closely resemble horizontally flipped versions of each other with different maximum thickness locations. The curvature at the leading edge is very similar for both airfoils and the trailing edge is nearly identical. Though the similarity in trailing edge can be ascribed to the constraint explained in section 4.2.

The main differences between the airfoils are the location of maximum thickness, the camber, and the thickness distribution. The forward shift in the location of maximum thickness is something that was already seen in chapter 5 and is favourable for flows with early transition. It seems that the design for turbulent flow has a negative camber which coupled with the thickness distributions results in a curve on the pressure side that resembles a whale. Whereas a design for a semi-laminar flow prefers a more common positive camber and a thickness distribution that is less focused on the leading edge.

6.4 Pressure Distributions

The pressure distributions of the airfoils from figure 6.2 are given in figure 6.4 for $C_l = 1.6$. The pressure distributions for $AR{=}1/3$ are given in figure 6.4a and $AR{=}4/3$ are given in figure 6.4b.

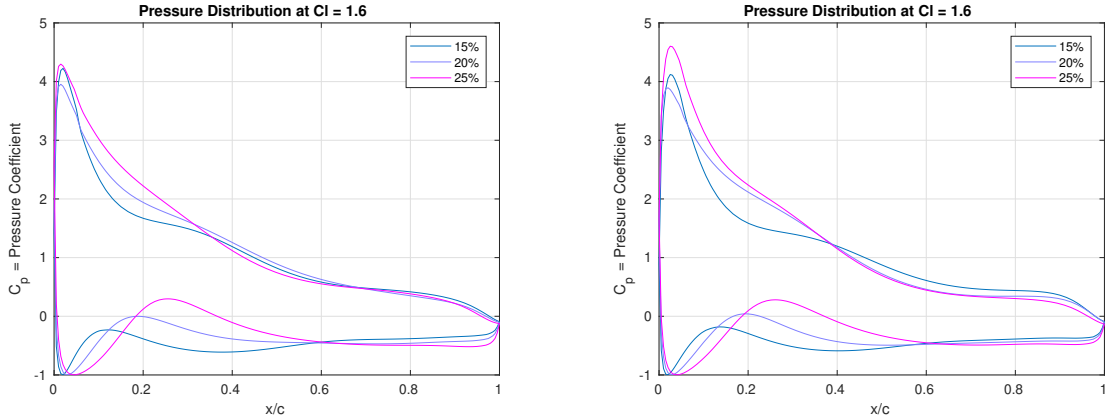

(a) *AR = 1/3* **(b)** *AR = 4/3*

Figure 6.4: *PP vs BH pressure distributions at* $C_l{=}1.6$ *for turbulent flow*

As the airfoil shapes are very similar so are the pressure distributions. The small differences on the suction side for the 25% airfoil in the concave pressure recovery region for $AR{=}4/3$ results in the larger suction peak that is seen in figure 6.4b. On the pressure side it can be seen that the pressure stays roughly constant past $0.6x/c$.

The pressure distribution at $C_l = 1.6$ for the 25% thick airfoil in figure 6.4b is compared to the pressure distribution of a 25% thick airfoil with $AR{=}4/3$ from chapter 4 in figure 6.5.

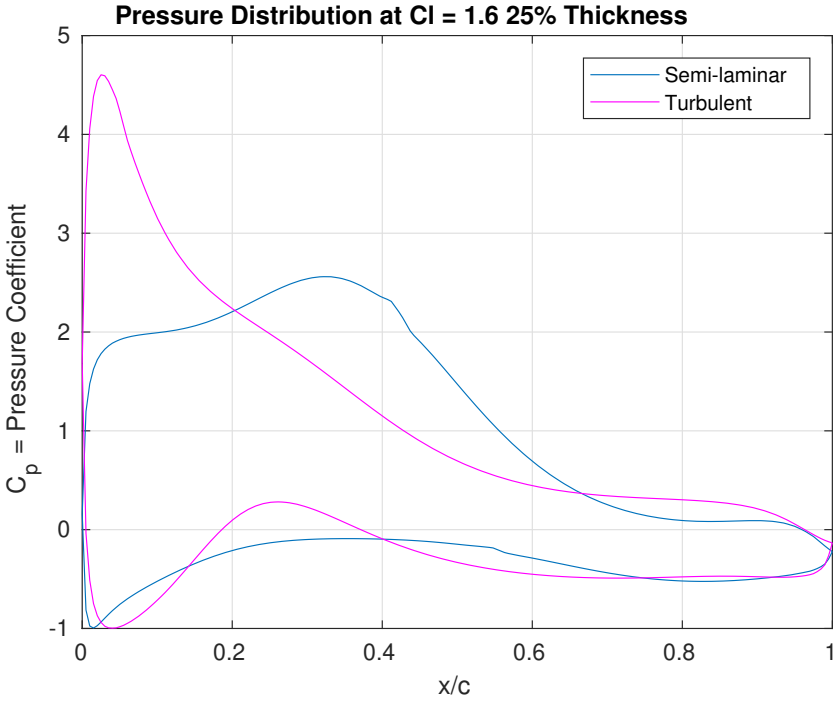

Figure 6.5: *Comparison of PP vs BH pressure distributions at $C_l{=}1.6$ for semi-laminar and turbulent flow*

The clearest differences can be seen with the suctions peaks. The location of the suction peak for the semi-laminar flow design corresponds to the location of maximum thickness for that airfoil. For the turbulent design the suction peak is at the leading edge at the point of forced transition and with almost twice the magnitude. The turbulent design does have a clear peak on the pressure side corresponding to the location of maximum thickness.

Both airfoils display constant pressure at the trailing edge on the pressure side. For the turbulent design however the constant pressure occurs at $0.6x/c$ instead of $0.8x/c$. Furthermore the semi-laminar does not feature a clear pressure peak as the turbulent design does.

As such the difference between the two airfoils can be summarised by the tendency of the turbulent design to focus on obtaining large pressure differences at the leading edge and small differences for the rest of the airfoil. While the semi-laminar design has a more even distribution of pressure differences for the leading edge and the mid-section until pressure recovery occurs.

6.5 Aerodynamic Polars

The aerodynamic polars for $AR{=}1/3$ and $4/3$ are given in figure 6.6. Figures 6.6a and 6.6b show the lift and drag polar respectively for $AR{=}1/3$ and figures 6.6c and 6.6d show the same for $AR{=}4/3$.

Firstly, when observing these aerodynamic polars, it is seen in the lift polars for the thinnest airfoils around 15% that the maximum lift coefficient have gone past 2.0. Which is usually not achieved unless high lift devices are used. Upon close inspection though the linear region of the lift polar stops at 2.0 or just below it. After which it is thought that soft stall occurs but this then results in a small increase in lift coefficient past 2.0 over a region of 5 degrees of angle of attack before which stall occurs fully.

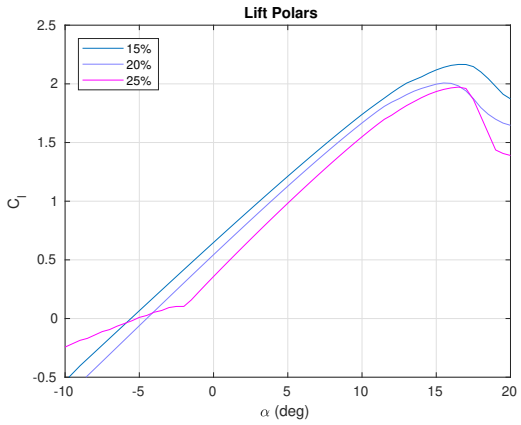

(a) *Lift Polar AR = 1/3*

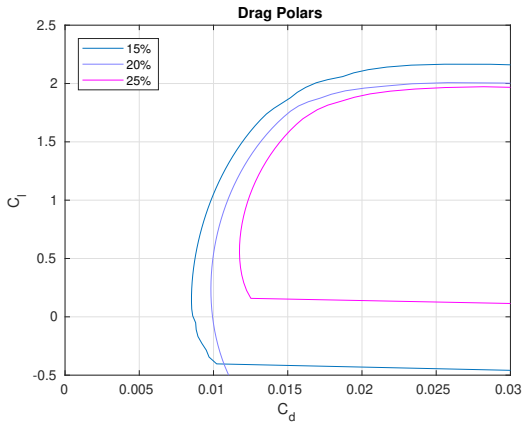

(b) *Drag Polar AR = 1/3*

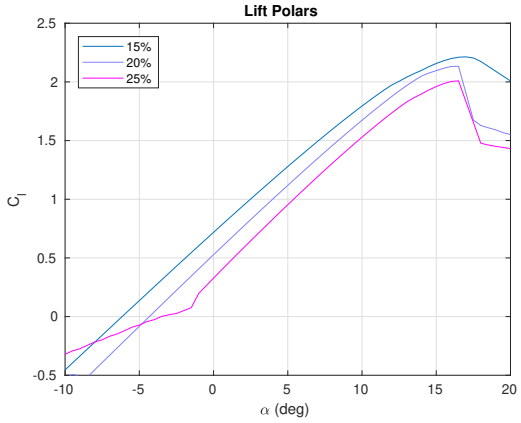

(c) *Lift Polar AR = 4/3*

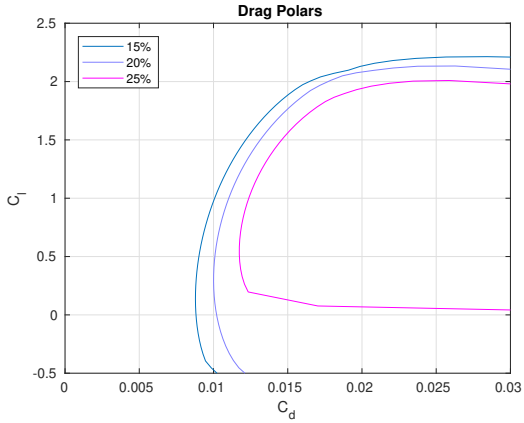

(d) *Drag Polar AR = 4/3*

Figure 6.6: *PP vs BH aerodynamic polars for turbulent flow*

Secondly, the drag polars have the highest values seen so far in this thesis which reinforce the idea that with a tether taken into account the airfoil drag becomes less important and high lift becomes the driving factor.

Important to note is that separation occurs at low angles of attacks, specifically around -2 degrees and lower, for the 25% thick airfoil. From the shape of this airfoil in section 6.3 it can be deduced that the separation occurs on the pressure side. The separation means that this airfoil can not be used for low angles of attack.

The aerodynamic polars for the 25% thick airfoil are compared to the aerodynamic polars for the 25% thick airfoil from chapter 4 in figure 6.7 with AR=4/3 for both airfoils.

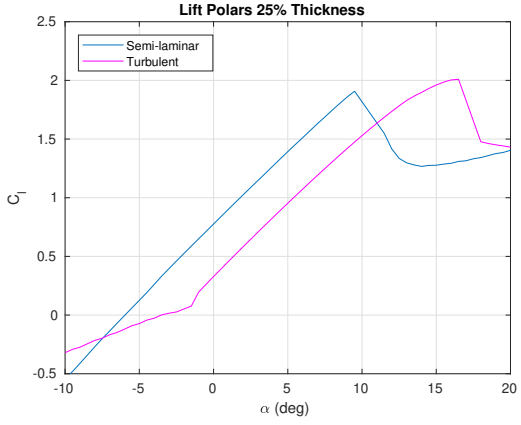

(a) *Lift Polar*

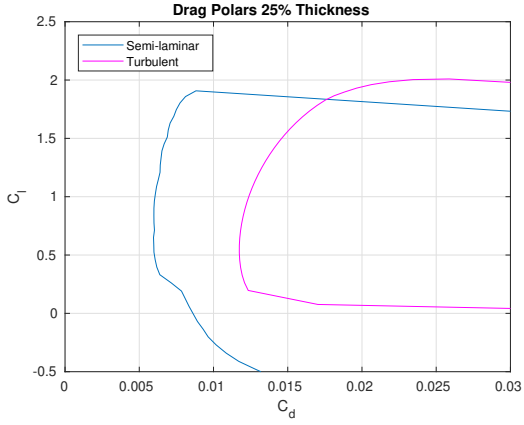

(b) *Drag Polar*

Figure 6.7: *Comparison of PP vs BH aerodynamic polars for semi-laminar flow and turbulent flow*

Looking at figure 6.7a the differences in lift polar are most clear in the linear region where the semi-laminar design has a linear region up to −10 degrees angle of attack and the turbulent design does not due to separation. The highest lift coefficient of the linear region is similar in value for both designs, however the turbulent design features a soft stall leading to a higher maximum lift coefficient before a sharp drop off. Furthermore the turbulent design requires higher angles of attack compared to the semi-laminar design.

As was touched upon earlier the turbulent design has very high drag values. As can be seen in figure 6.7b the drag values of the turbulent design is more than twice that of the semi-laminar design. The increased drag value is mostly due to the presence of a turbulent boundary layer. Furthermore the drag bucket does not extend to values below the linear region.

6.6 Comparison with existing airfoils

Up till now all comparisons done were between airfoils that were designed in this thesis. However, the airfoils in this chapter are considered to be optimised for AWE for the most important goals. Namely PP with a tether, BH, and RR in the form of the turbulent design case. It is therefore time to compare the airfoils designed in this thesis with well-known designs of comparable thickness and purpose.

The aerodynamic polars for the turbulent flow conditions in this chapter are used for comparison. The reference airfoils are calculated for turbulent flow conditions as well. Figure 6.8 shows the lift polars for the 15% and 25% thick airfoils with similar existing airfoils and figure 6.9 does the same for the drag polars. The existing airfoils are the S1223 and SD7037 for thin airfoils around 15% thickness and the DU 91-W2-250[10] and FFA-W3-241[46] for airfoils at 25% thickness. The coordinates for the S1223 and SD7037 were pulled from the UIUC Airfoil Database from the aerospace engineering department at the University of Illinois. The airfoils from this chapter are designated DU 18-Kxx. This designation is based upon Delft University of Technology (DU), the year of design (18), the author of thesis (K) and the thickness (xx).

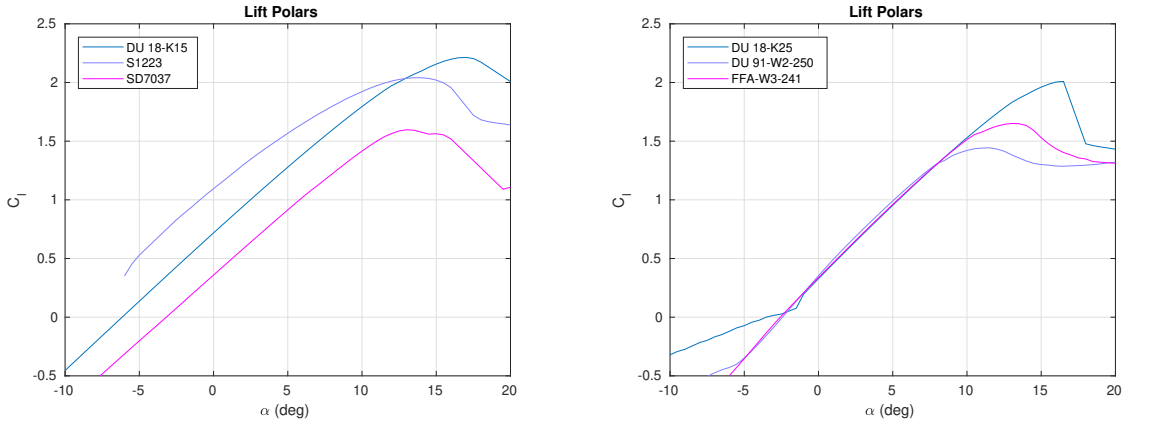

(a) *15% thickness, S1223, and SD7037* **(b)** *25% thickness, DU 91-W2-250, and FFA-W3-241*

Figure 6.8: *Comparison of lift polars with existing airfoils*

In figure 6.8a it can be seen that the 15% thick airfoil has higher maximum lift than both reference airfoils. The entire linear region is shifted towards lower angles of attack when compared to the SD7037. However, the S1223 has higher lift coefficients for angles between −5 and 12 degrees than the 15% thick airfoil. But past 12 degrees the 15% thick airfoil outperforms the S1223 with its capability of reaching a higher maximum lift coefficient.

In figure 6.8b all the airfoils have similar linear regions. The main difference is when separation occurs for low angles of attack, where the 25% thick airfoil separates around −1 degrees and the DU 91-W2-250 around −5 degrees. Furthermore the 25% thick airfoil goes up to a lift coefficient of roughly 1.8 in the linear region while the FFA-W3-241 goes up to 1.5 and the DU 91-W2-250 to 1.3. Both reference airfoils have a soft stall slightly increasing the maximum lift coefficient by 0.1 to 1.6 and 1.4 respectively however for the 25% thick airfoil the maximum lift coefficient is increase by 0.2 up to 2.0 before stall sets in.

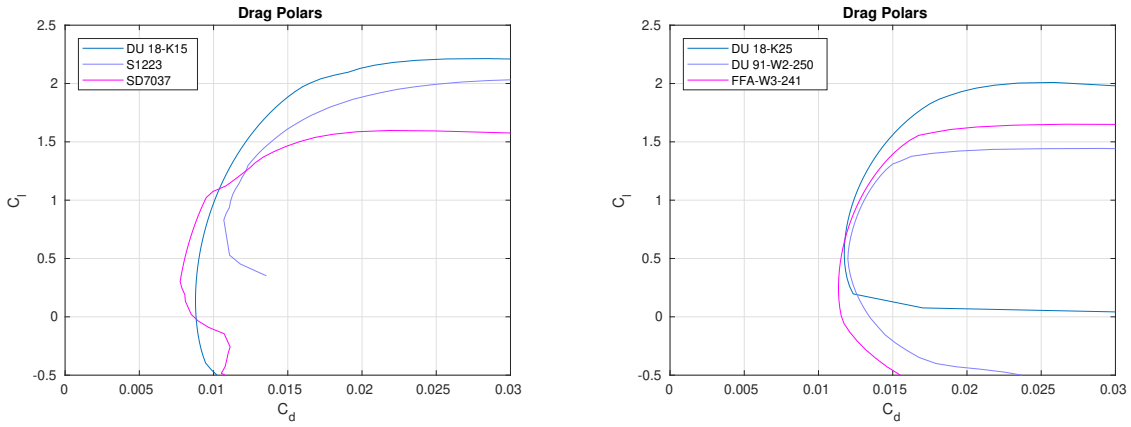

(a) *15% thickness, S1223, and SD7037* **(b)** *25% thickness, DU 91-W2-250, and FFA-W3-241*

Figure 6.9: *Comparison of drag polars with existing airfoils*

In figure 6.9a it can be seen that the S1223 has higher drag than the 15% thick airfoil for all lift coefficients. So that even when the S1223 has better lift performance between -5 and 12 degrees angle of attack the drag performance is worse. The SD7037 on the other hand has better drag values for lift coefficients between 0 and 1, but past a lift coefficient of 1 the 15% thick airfoil performs better again.

In figure 6.9b it seems that, similar to the linear region overlapping in the lift polars, the drag polars have a lot of common ground as well. For medium lift coefficients between 0.5 and 1 the difference in drag coefficient is very small. Outside these values the difference become clearer. The 25% thick airfoil is capable of going to higher maximum lift which results in less drag at the maximum lift coefficients for the reference airfoils. However as mentioned before the 25% thick airfoil separates earlier at low angles of attack compared to the reference airfoils leading to larger drag values at low angles of attack.

6.7 Findings

In conclusion designing for turbulent flow with a tether results in high lift designs. As high as possible pressure difference is generated at the leading edge for high lift in a turbulent flow. High lift is generated at high angles of attack which results in large amounts of drag. However as was concluded earlier airfoil drag is considered less important due to a tether being included in the calculations.

When comparing to existing airfoils the airfoils designed have higher maximum lift coefficients and similar drag coefficients as the reference airfoils. From purely a lift and drag perspective the airfoil designed in this chapter would be better than the references.

Designing for Longitudinal Stability

Up to this chapter the moment polar of an airfoil has not been taken into consideration. This chapter takes the moment polar into consideration and focuses on designs for longitudinal stability. Section 7.1 explains why the new designs focus on longitudinal stability. The design approach is outlined in section 7.2 and section 7.3 presents the Pareto fronts for the new designs. The shapes of the designs are in section 7.4. Pressure distributions for the airfoils are shown in section 7.5. The aerodynamic polars are then shown in section 7.6 with moment polars in section 7.7. The new designs are compared to existing ones in section 7.8 and the chapter is ended in section 7.9.

7.1 Rationale

It was decided to design airfoils focused on moment polars to improve the performance of AWE systems flying at constant attitude. Flying at constant attitude requires that the aerodynamic moment of the aircraft is zero. In a general longitudinal static setting the aerodynamic moment, located at the centre of gravity, consists of four parts. Namely, the moments of the wing and tail and the lifts of the wing and tail multiplied with their respective arms. For simplification it is assumed that the tail moment is zero because the tail airfoil is symmetric. The general case with this simplification is illustrated in figure 7.1.

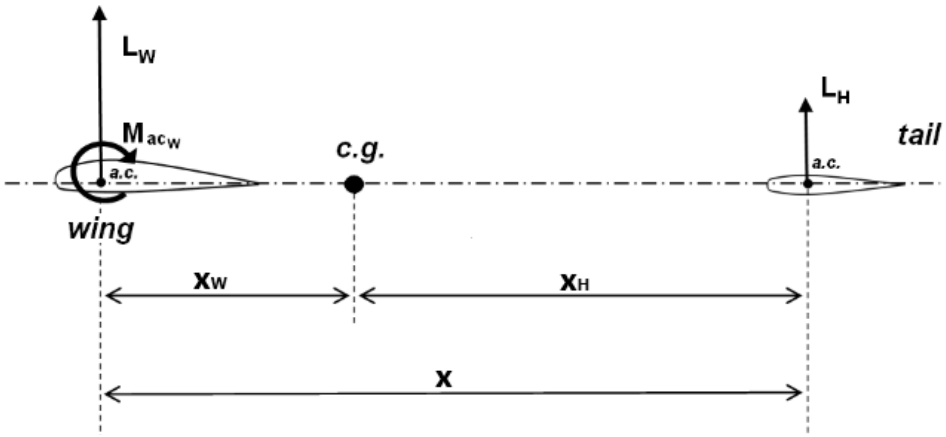

Figure 7.1: *Longitudinal static stability with zero tail moment*

Taking the moment balance around the centre of gravity in figure 7.1, with clockwise moments being positive, and setting this to zero for constant attitude equation 7.1 is found.

$$0 = L_w x_w - L_h x_h + M_{ac_w} \tag{7.1}$$

To analyse equation 7.1 it is assumed that the lift of the wing (L_w) and the distances between the wing (x_w) and tail (x_h) with respect to the centre of gravity do not change. The lift of the tail (L_h) is allowed to vary and the wing moment (M_{ac_w}) will be considered for three cases. For the first case M_{ac_w} is zero, equation 7.1 then shows that L_w x_w and L_h x_h have to be equal in value to achieve a zero aerodynamic moment. For the second case M_{ac_w} is set to be a positive value, now L_h has to increase in magnitude to offset this positive moment. For the third case M_{ac_w} is set to a negative value which results in L_h decreasing in value. From these three cases it can be seen that the wing moment influences the tail lift and thus also the total lift of the aircraft. The total lift of the aircraft is directly linked to the performance of the system.

In principle tethered aircraft may have more relaxed aerodynamic moment constraints than untethered ones. The tether can namely be used to counter-act at least part of the aerodynamic moments with the right placement. Placing a tether in front of the centre of gravity in figure 7.1 will create a negative moment which can offset

the wing moment. This is not easily achieved in practice however. The moments produced by the tether vary with the forces the tether apply to the aircraft.

In contrast to previous chapters it was decided to design for moment polars by fixing the moment coefficient and then optimising for PP and BH with the same cost functions used throughout this thesis. As such a constraint was applied to optimise only for airfoils near a specific value for moment coefficient as input.

7.2 Moment Constraint

In order to implement a moment constraint it is necessary to know what moment polar is desired for the airfoils. It was reasoned that a constant moment coefficient in the linear region would be desirable. If the moment coefficient does not change with angle of attack no adjustments for control have to be made during flight. Outside the linear region effects such as stall and separation occur and moments outside the linear region are not considered for design. Taking this into account the goal becomes to keep the moment coefficient C_m constant for given C_l values. However, it is impossible to design airfoils with a perfect constant C_m and as such the airfoils are allowed to deviate by 20% of the desired C_m.

A threshold value of 20% is used for a given desired C_m. Past this threshold the airfoil would be fully discarded and between the threshold and the desired C_m the airfoil is penalised depending on the difference. For example if the desired C_m would be -0.10 then any airfoil at -0.10 would be given a score of 1 and any airfoil outside the range $-0.08 \leq C_m \leq -0.12$ would be given a score of 0 with a linear distribution of score in the range itself.

The constraint applies to each C_m at the C_l given by the C_l ranges used in the PP cost function. Furthermore to each C_m the same weights in the C_l range are applied. This would allow for some of the C_m checked to be given a 0 score with the total score still being higher than 0. However this is not desired and thus when one of the C_m in the C_l range has a score of 0 the airfoil is discarded. An example of the constraint is given in figure 7.2 where the airfoil only goes past the threshold bounds at very low angle of attack outside of the C_l range.

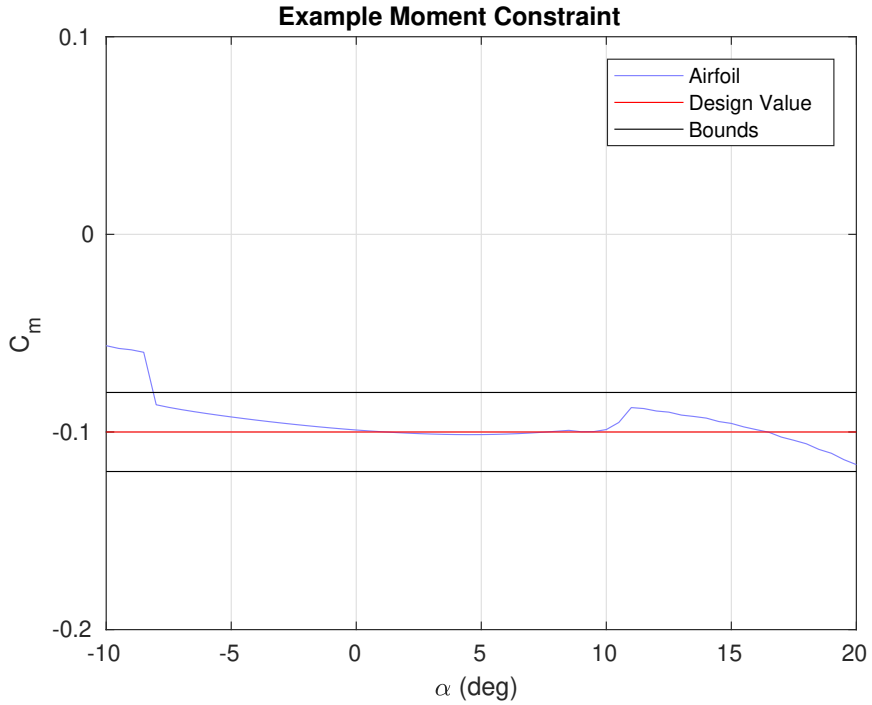

Figure 7.2: *Example Moment Constraint*

Furthermore using a % threshold does bring some issues, especially for extreme cases such as a neutrally stable airfoil at $C_m = 0$. When $C_m = 0$ the 20% threshold would still be at 0. This would then result in optimisation problems as a perfect 0 C_m for a range of C_l is unfeasible. Thus when the 20% threshold results in differences between the desired C_m and the outer bounds of less than 0.01 the difference is set to 0.01. So for the neutrally stable example this would result in 0 scores at a C_m of 0.01 or -0.01.

7.3 Pareto Front

The flow settings and the cost functions used are mostly the same as in chapter 6. However, optimisation results differ because of the imposition of the moment constraint. Another difference is that AR was fixed at the value of 3/3 or 1, whereas in chapters 4 and 6 it varied from 1/3 to 4/4. It is anticipated that using the moment constraint explained in section 7.2 will results in airfoils with less lift. Early tests confirmed this insight and so the range of lift coefficients used for the PP cost function has been updated to better fit this. Furthermore it is desired to have a constant moment coefficient over a large range of lift coefficients thus resulting in the values shown in table 7.1.

Table 7.1: *Range of airfoil lift coefficients and corresponding weights for tethered flight in turbulent flow with fixed moment coefficient*

C_{l_i}	0.0	0.2	0.4	0.6	0.8	1.0	1.2	1.4
w_i	0.05	0.1	0.1	0.1	0.0	0.15	0.2	0.2

Using the moment constraint and the updated range of lift coefficients figure 7.3 is generated. Where the Pareto front for three different fixed moment coefficients are shown. Where moderate unstable values of $C_m = -0.10$ and -0.05 were used together with the neutrally stable value of $C_m = 0.00$.

When looking at figure 7.3 it seems all three Pareto fronts share common ground for thin airfoils around 18% to 19% thickness, but diverge as thickness increases. A trend can be seen that as the C_m goes toward neutrally stable the thicker airfoils perform worse in an aerodynamic sense as seen by the increase in the PP score. This also results in a thickness limit of 26% for the neutrally stable front where the other two fronts can go up to 30% thickness.

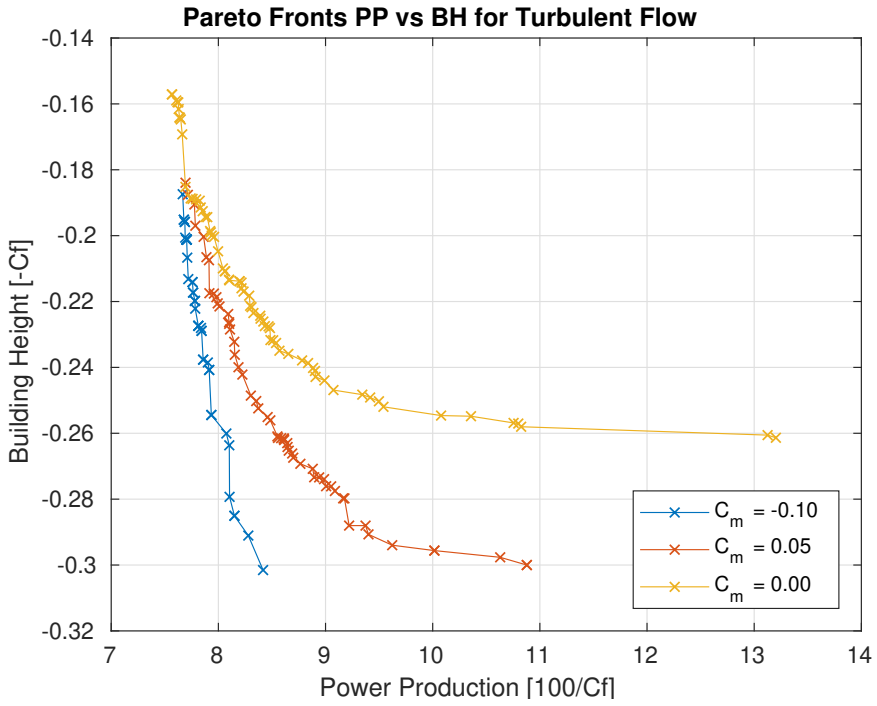

Figure 7.3: *PP vs BH Pareto Fronts for fixed moment coefficients*

7.4 Airfoil Shape

In figure 7.4 airfoil shapes from the Pareto fronts in figure 7.3 are shown for thicknesses of 20%, 25%, and 30%. Figure 7.4c which corresponds to a C_m of 0.00 does not have a 30% thickness airfoil due to a limit of 26% as was seen in the Pareto front.

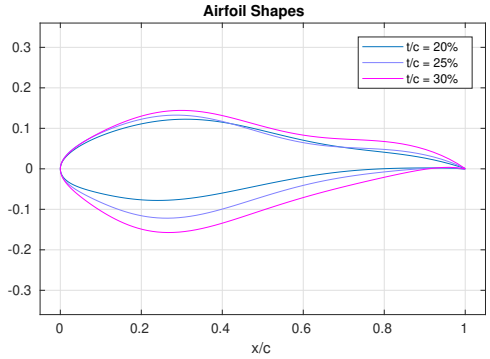

(a) $C_m = -0.10$

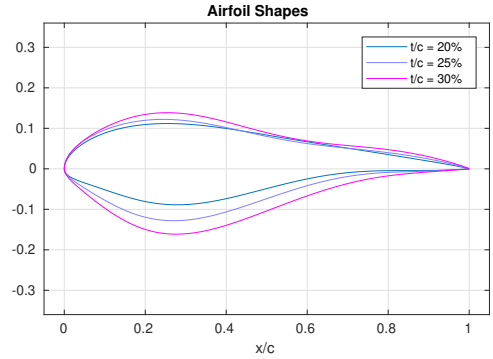

(b) $C_m = -0.05$

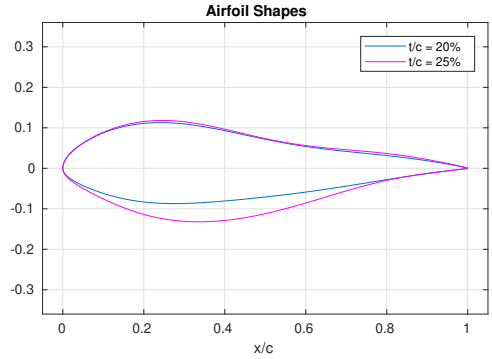

(c) $C_m = 0.00$

Figure 7.4: *PP vs BH Airfoil shapes for fixed moment coefficients*

Similar to the airfoils shown in chapters 4 and 6 the clearest changes to airfoil shape with increasing thickness occur on the pressure side. For $C_m = 0.10$ and -0.05 there are small increases in thickness on the suction side for the location of maximum thickness for the 20% and 25% airfoils. However when going to a more extreme 30% the trailing edge increases in thickness as well. Whereas for $C_m = 0.00$ the change on the suction side is negligible and the pressure is the focus.

Interesting to note is that for $C_m = 0.10$ and -0.05 the location of maximum thickness does not change, but for $C_m = 0.00$ it does change marginally, around $0.1x/c$ difference.

The airfoils with 20% thickness are compared to each other together with the 20% thickness airfoil with $AR = 3/3$ from the designs explained in chapter 6. These shapes are found in figure 7.5. The shapes can be identified by their C_m design value and for the airfoil from chapter 6 no constraint was used on the moment coefficient which results in a free C_m for designation.

The clearest difference can be found on the pressure side of the airfoil. Where the free airfoil shows a rounder and thicker leading edge with a large concave curve for $0.2 \leq x/c \leq 0.6$ after which the airfoil goes straight towards the leading edge. This curve goes slightly above the centre line which results in a small dip at very end of the trailing edge. $C_m = -0.10$ and -0.05 are similar on the pressure side, both have a sharper leading edge compared to the free airfoil and the concave curve occurs from $0.3 \leq x/c \leq 0.7$ before going straight to the leading edge. However these curves do not go above the centre line. For $C_m = 0.00$ the pressure side is similar at the leading edge but past $0.3x/c$ the curve to the leading edge is convex which results in more thickness for this part of the airfoil.

The differences on the suction side are less clear. The free airfoil is less rounded on the leading edge which transitions to less thickness along the entire suction side except for the trailing edge which was pushed upwards from the centre line. The three fixed C_m have similar leading edges up till $0.2x/c$ after which the curves diverge. $C_m = -0.10$ is thicker on the suction side before the pressure recovery region. $C_m = -0.05$ and 0.00 are similar till the pressure recovery. The difference then lies in the pressure recovery region where $C_m = 0.00$ is more concave.

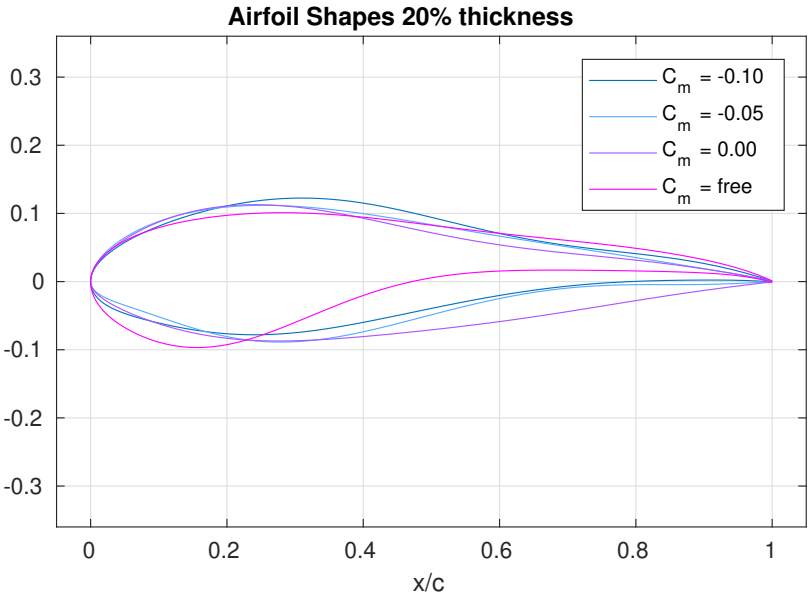

Figure 7.5: *Comparison of PP vs BH airfoil shapes for fixed and free moment coefficients*

7.5 Pressure Distributions

The pressure distributions of the airfoils in figure 7.4 were generated for turbulent flow at $C_l = 1.2$ and are shown in figure 7.6.

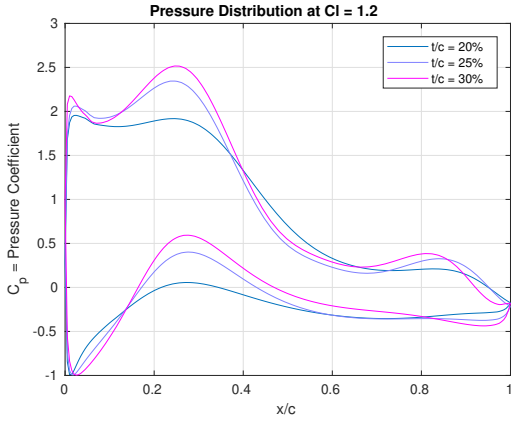

(a) $C_m = -0.10$

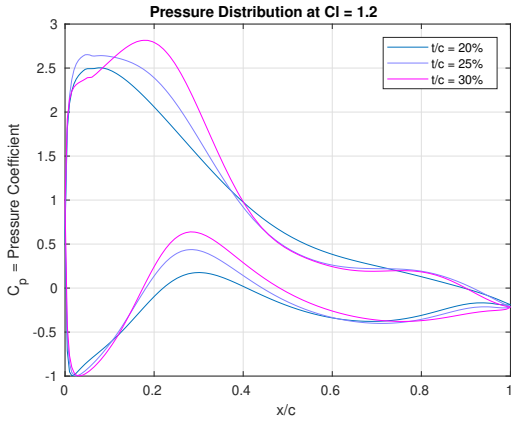

(b) $C_m = -0.05$

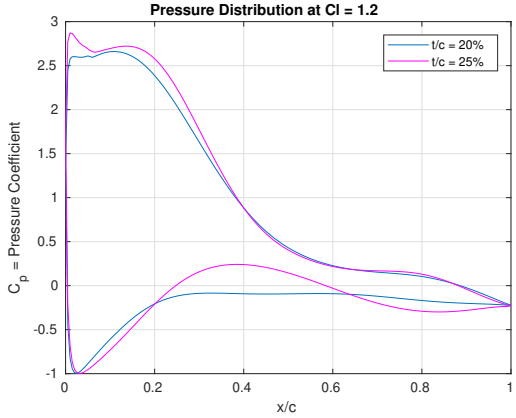

(c) $C_m = 0.00$

Figure 7.6: *PP vs BH pressure distributions at* $C_l = 1.2$ *for fixed moment coefficients*

Although these airfoils were designed for turbulent flow similar to chapter 6 it seems that the suctions peaks are not directly at the leading edge. Transition does occur at the leading edge indicated by the adverse pressure gradients, which is seen clearest for the $C_m = -0.10$ case, however the suction peaks occur at the point of maximum thickness around $0.2x/c$. For $C_m = -0.05$ it seems the suction peaks occur near transition for thicknesses of 20% and 25%, for 30% the suction peak occurs at maximum thickness. $C_m = 0.00$ shows adverse pressure gradients at transition for 25% thickness and for both thicknesses the suction peak is located at maximum thickness.

The three moment coefficients seem to maintain similar pressure distributions. In all cases there are large pressure differences up to the maximum thickness point, upon which there are strong adverse gradients for the pressure recovery until half chord. A difference is that for $C_m = 0.00$ the suction and pressure peak do not align with each other at the point of maximum thickness while for $C_m = -0.10$ this occurs for all three airfoils and for $C_m = -0.05$ this occurs for the thickest airfoil.

The pressure distributions at $C_l = 1.2$ for the three moment coefficients for the 20% thick airfoil are plotted together with the pressure distribution for the 20% thick airfoil at $AR = 3/3$ from chapter 6. These pressure distributions are found in figure 7.7.

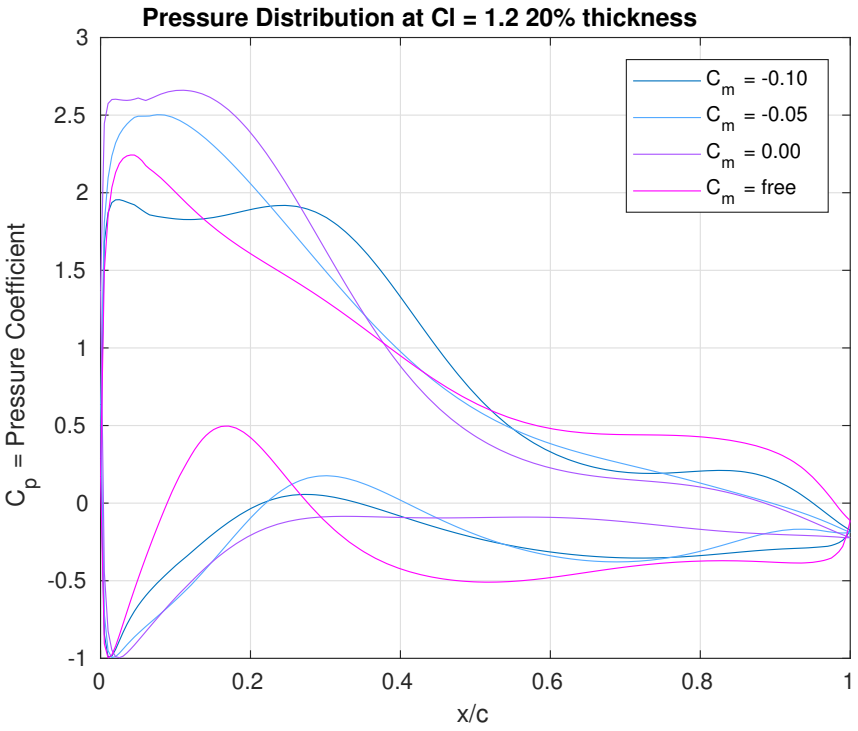

Figure 7.7: *Comparison of PP vs BH pressure distributions at $C_l = 1.2$ for fixed and free moment coefficients*

In figure 7.7 it can be seen that the distributions are very different from each other. The free airfoil has larger pressure differences past $0.4x/c$ but due to the smaller suction peak and the larger pressure peak it has smaller pressure differences before $0.4x/c$. $C_m = -0.10$ has the smallest suction peak but this occurs more aft than the other airfoils and the pressure recovery region is thus also smaller. Although $C_m = -0.05$ and 0.00 have larger suction peaks and longer pressure recovery regions their pressure curves tend towards the same pressure as $C_m = -0.10$ just past $0.6x/c$ after which they drop further towards the leading edge. On the suction side $C_m = -0.10$ and -0.05 are similar with a small difference towards the suction peak and magnitude. Where as for $C_m = 0.00$ with the convex shape shows a smooth pressure curve without a clear peak on the suction side.

7.6 Aerodynamic Polars

In figures 7.8 to 7.10 the lift and drag polars for the three moment coefficients are found.

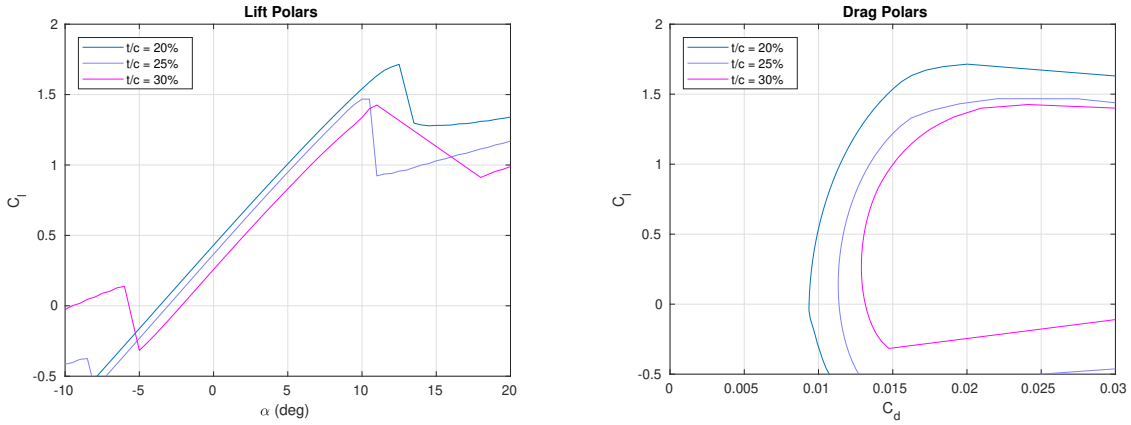

(a) *Lift Polar* **(b)** *Drag Polar*

Figure 7.8: *PP vs BH aerodynamic polars for a fixed moment coefficient of -0.10*

It is seen that in figure 7.8 there is a noticeable drop in maximum lift coefficient as the thickness increases past 20%. Furthermore there is a shift in the polar to go towards higher angle of attack as the thickness increases and the linear region decreases in length as well. The increase of thickness results in higher drag values as expected. The separation around a C_l of -0.3 for the 30% airfoil is also clearly seen in the drag polar.

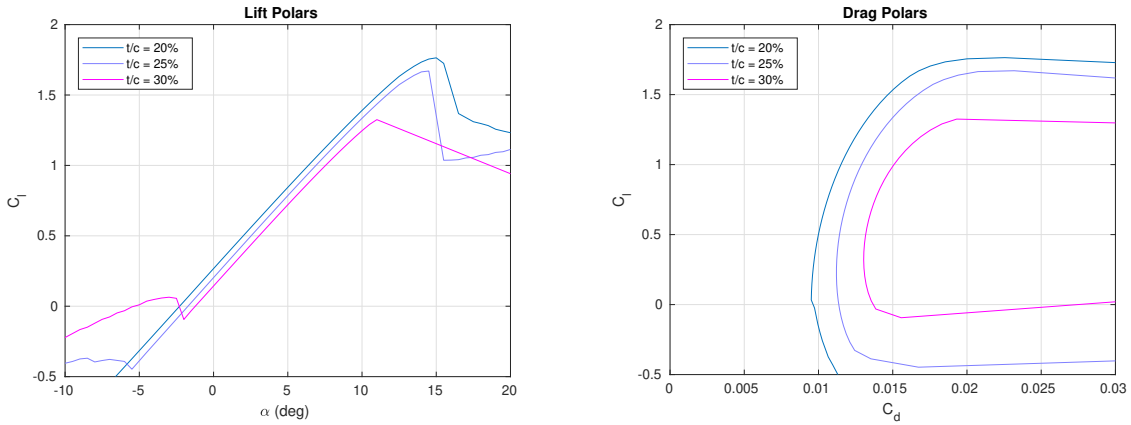

(a) *Lift Polar* **(b)** *Drag Polar*

Figure 7.9: *PP vs BH aerodynamic polars for a fixed moment coefficient of -0.05*

In figure 7.9 the drop in maximum lift coefficient occurs past 25% thickness instead of 20%. It is thought that this is the case because for $C_m = -0.10$ the 20% and 25% pressure distributions showed suction peaks at the point of transition instead of maximum thickness. Leading to larger pressure differences and thus more lift. The drag polar reflects the points of separation and stall clearly for the 30% airfoil.

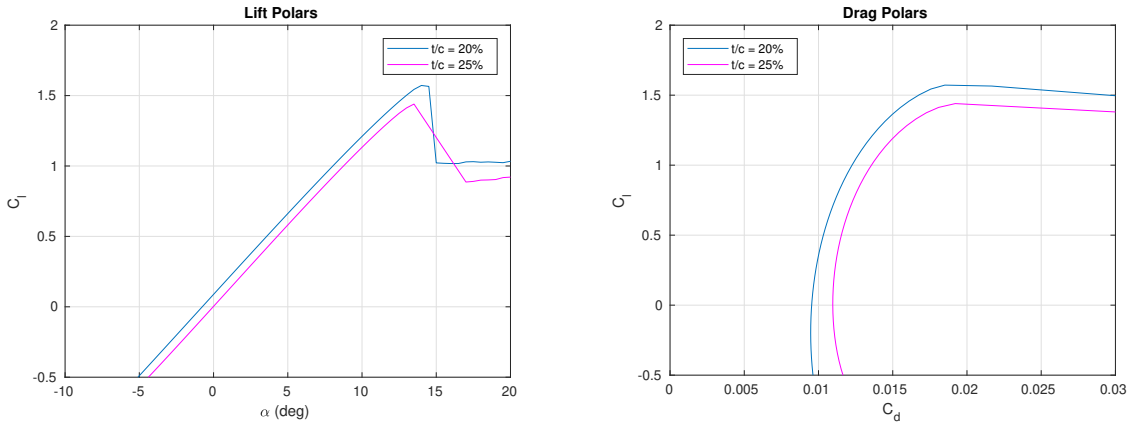

(a) *Lift Polar* **(b)** *Drag Polar*

Figure 7.10: *PP vs BH aerodynamic polars for a fixed moment coefficient of 0.00*

Figure 7.10 does not show as large a drop in maximum lift coefficient as in figures 7.8 and 7.9 however the maximum lift coefficients are clearly lower. Unlike the airfoils for $C_m = -0.10$ and -0.05 there are no cases of separation at negative angles of attack.

The aerodynamic polars for the 20% thick airfoils at $AR = 3/3$ for the three fixed moment coefficient and the free moment coefficient from chapter 6 are shown in figure 7.11 for comparison.

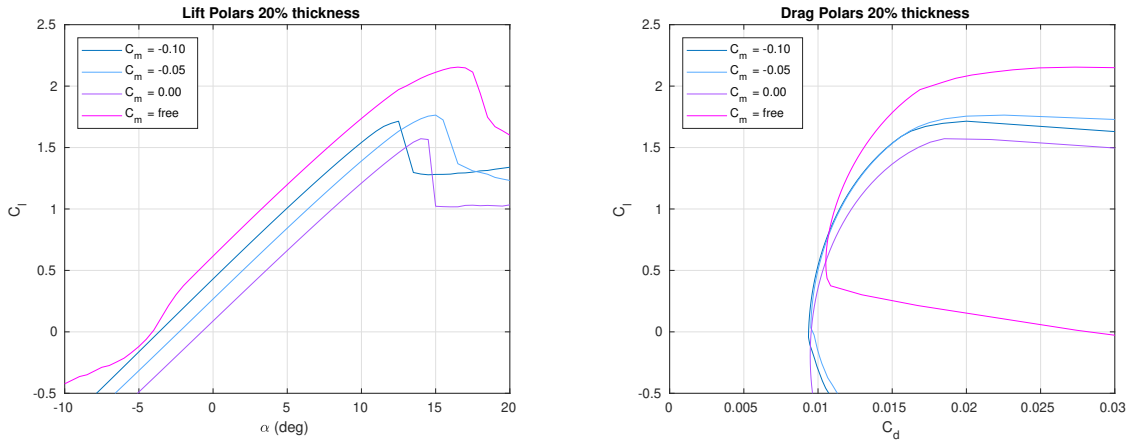

(a) *Lift Polar* **(b)** *Drag Polar*

Figure 7.11: *Comparison of PP vs BH aerodynamic polars for fixed and free moment coefficients*

It can be seen clearly that with increasingly positive C_m, *free* has a maximum C_m of -0.18, the lift polar shifts towards higher angles of attack. Furthermore the maximum lift coefficient also decreases as the airfoil becomes more stable. Without a constraint on stability the maximum lift is above 2.0 and with it the maximum lift tends to lower values above 1.5. It is shown that $C_m = -0.10$ and -0.05 are similar in maximum lift. The constraint on moment coefficient does lead to a longer linear region with no separation in the considered range of angles of attack.

The drag values are similar for low angles of attack and when disregarding the separation that occurs for the free airfoil. Past a C_l of 0.5 however the drag values diverge. For the neutrally stable airfoil the drag increases compared to the other two fixed moment airfoils. The free airfoil has less drag compared to all other three airfoil at higher angles of attack.

7.7 Moment Polars

In figure 7.12 the moment polars for the three moment coefficients are shown as confirmation that indeed the designs function as they should, with near constant moment coefficient in the linear region.

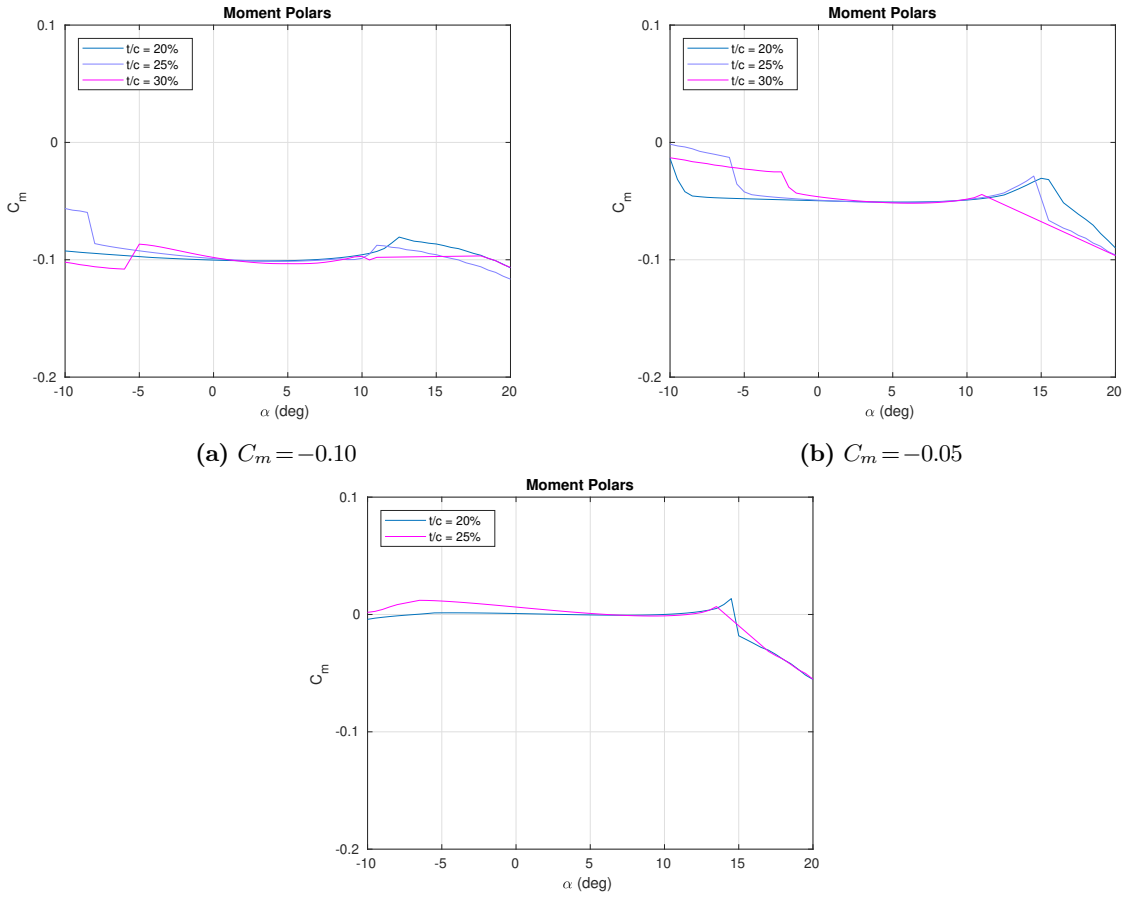

(a) $C_m = -0.10$ **(b)** $C_m = -0.05$

(c) $C_m = 0.00$

Figure 7.12: *PP vs BH moment polars at* $C_l = 1.2$ *for fixed moment coefficients*

Figure 7.12 shows that the airfoils designed are extremely close to the design values for the linear regions. The deviations from the design value tend to increase as the thickness increases. Which is clearest for $C_m = 0.00$ which shows the largest deviations in the linear region around an angle of attack of -5 degrees.

The moment polars for the three fixed moment coefficients and free moment coefficient is given in figure 7.13 with $AR = 3/3$ and airfoil thickness of 20%.

As was mentioned for fixed moment coefficient the moment polars are nearly constant in the linear region as was the design goal. The free airfoil on the other hand shows increasing stability as the angle of attack increases in the linear region. The linear region of this airfoil is at an angle of attack of roughly -2 up to 13 degrees. In this region C_m increase from -0.18 to -0.15.

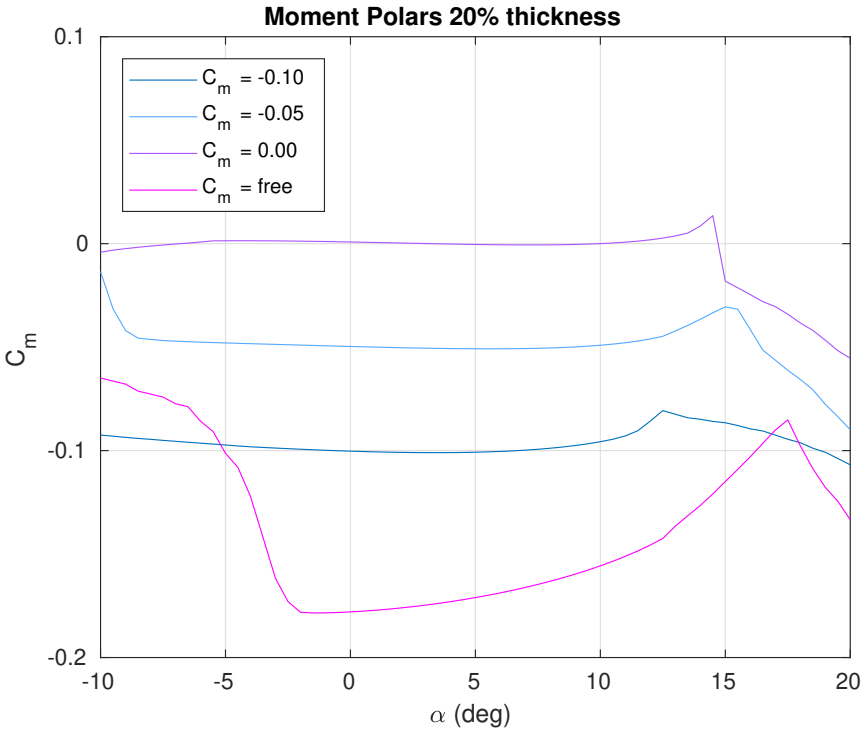

Figure 7.13: *Comparison of PP vs BH moment polars for fixed and free moment coefficients*

7.8 Comparison with existing airfoils

Similar to chapter 6 the airfoils in this chapter will be compared with existing airfoils. As the focus of this chapter was on moment coefficients this will be used as the benchmark for comparison. Thus in figure 7.14 the three moment coefficient design values of -0.10, -0.05, and 0.00 are shown with comparable airfoils. With figures 7.15 and 7.16 showing the lift and drag polars. For the airfoils from this chapter the 20% thick airfoils were chosen. These airfoils follow the same designation as in chapter 6 but with two added numbers indicating the moment coefficient design value. For reference airfoils the SD7037 and FFA-W3-241 from chapter 6 are reused. The MH92 airfoil has been added as it is a well known flying wing airfoil and thus would make for a good comparison for $C_m = 0.00$. Furthermore a selection of NACA airfoils have been used. From Dadone[47] it was found that the NACA2412 and NACA4412 had moment coefficients of roughly -0.05 and -0.10. However these were far thinner than the 20% airfoil displayed here, thus the NACA2421 and NACA4421 were also used for comparison. Furthermore two symmetrical 6-series with 18% thickness have been chosen for $C_m = 0.00$ as symmetrical airfoils should be neutrally stable. Which resulted in the NACA66018 and NACA633018.

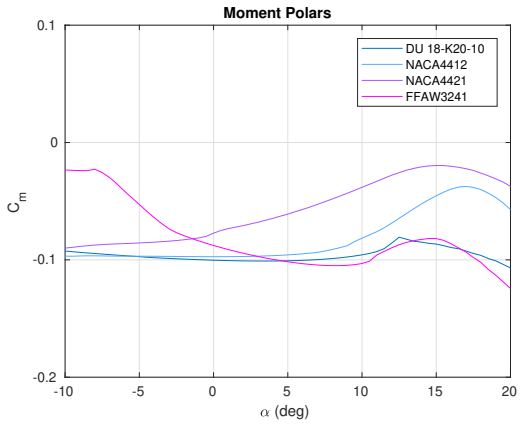

(a) C_m = *-0.10*

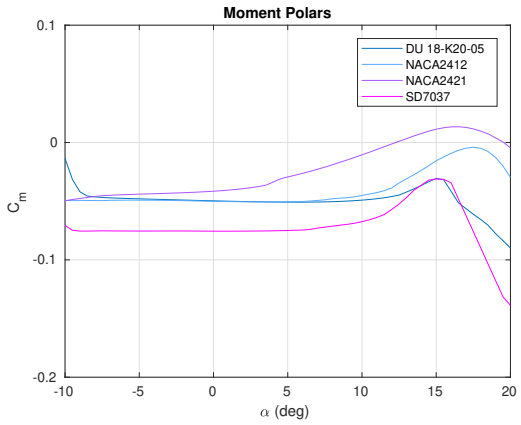

(b) C_m = *-0.05*

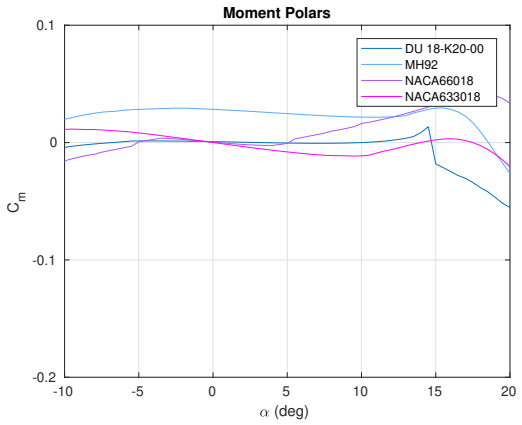

(c) C_m = *0.00*

Figure 7.14: *Comparison of moment polars with existing airfoils*

In figure 7.14a it can be seen only the NACA4412 is really similar in keeping a constant moment coefficient around -0.10. The FFA-W3-241 airfoil has a decaying moment coefficient to -0.10 while the NACA4421 has an increasing moment coefficients starting at -0.10. Figure 7.14b shows that the NACA2412 is very similar in the linear region compared to the DU 18-K20-05 airfoil. The SD7037 also displays a constant moment coefficient albeit at a value of -0.08. The NACA2421 displays a curve that stays near the value of -0.05 up to 2 degrees angle of attack after which it increases in value. Figure 7.14c shows the most consistency between airfoils. As expected the symmetric airfoils of NACA66018 and NACA633018 are close to the $C_m = 0.00$ line while the MH92 line has a constant positive moment coefficient around 0.03.

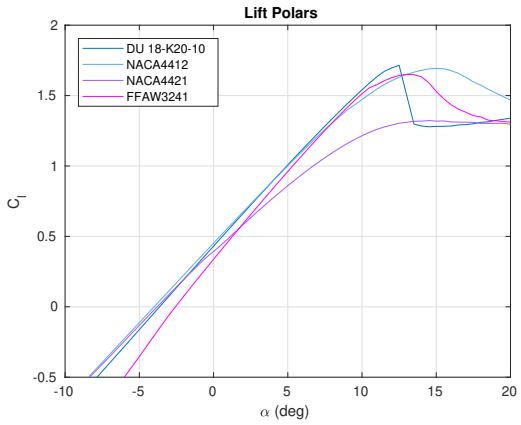

(a) C_m = *-0.10*

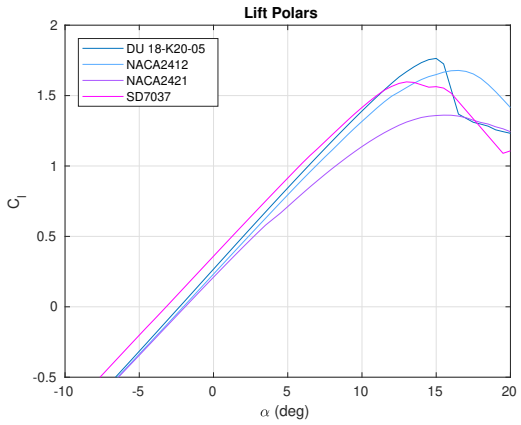

(b) C_m = *-0.05*

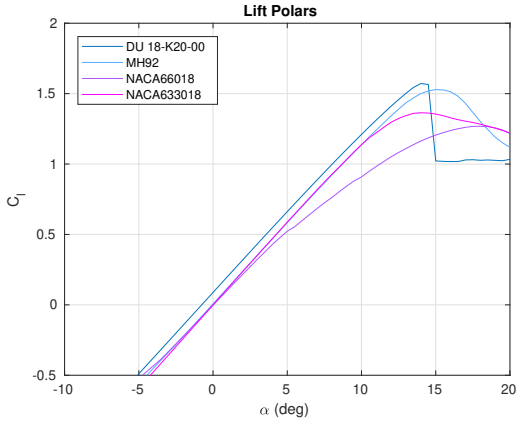

(c) C_m = *0.00*

Figure 7.15: *Comparison of lift polars with existing airfoils*

Unlike the moment polars the lift polars are far closer to each other as can be seen in figure 7.15. In figure 7.15a the linear region of DU 18-K20-10 and the NACA4412 are almost the same, as was expected after looking at the moment polar. The FFA-W3-241 has a different slope to the linear region but for angles of attack between 5 and 10 degrees is very similar. The NACA4421 starts similar at negative angles of attack but quickly loses out in slope and maximum lift coefficient. In figure 7.15b the same behaviour as for $C_m = -0.10$ can be seen, DU 18-K20-05 and the NACA2412 are very similar in the linear region with a slight difference in maximum lift coefficient. SD7037 which also showed a constant moment coefficient has a slightly different slope to the linear region and a larger difference in maximum lift coefficient while the thicker NACA2421 again shows a decrease in slope and a decrease in maximum lift coefficient. Figure 7.15c shows that the MH92 and NACA633018 have very similar linear regions that are shifted by 1 degree angle of attack compared to DU 18-K20-00. DU 18-K20-00 and MH92 are also very close in maximum lift coefficient while NACA633018 is significantly lower and NACA66018 is even lower with a worse slope.

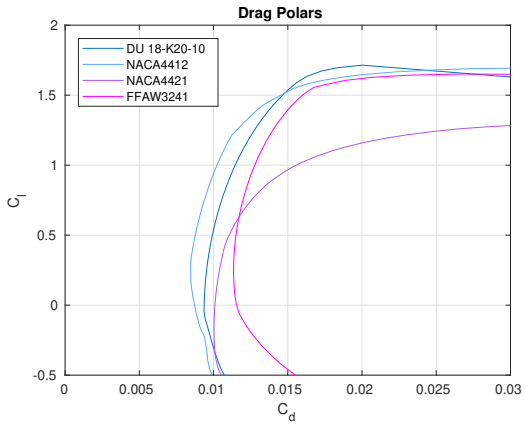

(a) C_m = *-0.10*

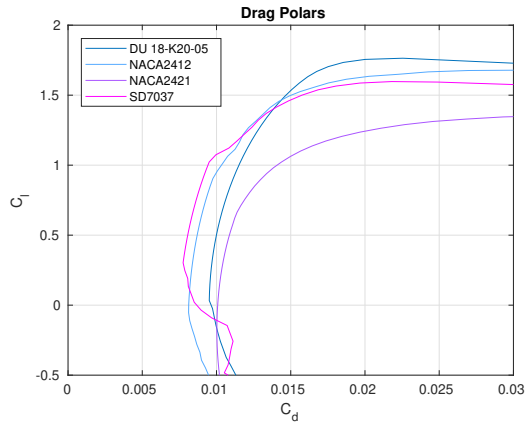

(b) C_m = *-0.05*

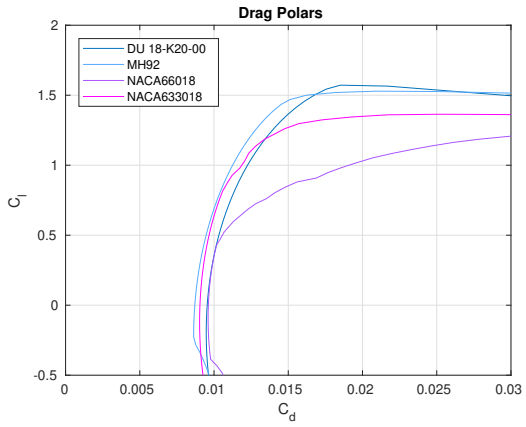

(c) C_m = *0.00*

Figure 7.16: *Comparison of drag polars with existing airfoils*

The drag polars in figure 7.16 show clear differences even when the moment polar and lift polar are similar. For example in figure 7.16a the NACA4412 has lower drag values in the region of 0 to 1.5 C_l compared to the DU 18-K20-10. This is mostly as expected due to the 8% thickness difference. This is also confirmed by the thicker NACA4421 and FFA-W3-241 both having higher drag values. Similarly in figure 7.16b the thinner NACA2412 and SD7037 have better drag values for intermediate lift coefficient, but past 1.5 the DU 18-K20-05 performs better while NACA2421 has the highest drag. Figure 7.16c on the other hand shows very similar drag values for all four airfoils. There are small shifts around 0.001 between the DU 18-K20-00 and the NACA66018 compared to the MH92 and the NACA633018. Another difference lies with what the maximum lift coefficient was and thus where the drag values end.

7.9 Findings

Designing airfoils for longitudinal stability through a constraint on the optimisation procedure resulted in designs with constant moment coefficient in the linear region. The moment coefficients were constant for values of -0.10, -0.05, and 0.00. The airfoil designs featured a spread out thickness distribution with lower camber when compared to the designs of previous chapters. Which lead to smaller pressure differences and a loss in lifting capabilities.

When comparing to existing airfoils it can be seen that for constant moment coefficient values of -0.10 and -0.05 the designed airfoils are better when it comes to lift and stability. The thinner existing airfoils that were used in the comparison have lower drag values as expected due to their thinness. There are also existing airfoils, such as the MH92, that are similar in lift, better in stability, and have less drag when compared to the most stable airfoil at $C_m = 0.00$.

Conclusion

This thesis discussed the optimal design of airfoils specific to airborne wind energy applications. Numerical optimisation techniques were used to generate these designs. In particular the code known as OptiFlow[1] was used, which makes use of a genetic algorithm called NSGA-II[3] for optimisation and the flow solver Rfoil[4] to calculate airfoil properties.

Firstly, objective functions for power production and building height were created for use in optimisation. The function for power production was a simple performance ratio of lift cubed divided by drag squared based upon the derivations by Loyd[44]. The function for building height was simply the maximum thickness of an airfoil at any point along the chord. Using these functions the first airfoils were designed for semi-laminar flow conditions. Which resulted in airfoils capable of reaching lift coefficients of 1.5 at low angles of attack around 5 degrees with low drag values of 0.005.

Secondly, the effect of tethers used in AWE systems was taken into account. The lift over drag ratio was changed based upon an estimation by Houska and Diehl[5]. The performance ratio became lift cubed divided by the square of airfoil drag plus an estimation of cable drag. Using this new ratio the function for power production was updated and new designs were generated. It was found that the optimiser presented airfoil designs with infinitely thin trailing edges which were unfeasible from a manufacturing point of view. Requiring a specific constraint to be set up that ensures the trailing edge does not go below a certain thickness. With the constraint the designs started to feature higher lift coefficients of 1.8 to 2 at higher angles of attack of 10 degrees. Drag also increased to 0.008 or 0.01 depending on the thickness of the airfoil.

Thirdly, the design implications of roughness sensitivity were investigated. At first a new function was set up which replaced the building height function. This function was simply the difference between rough and clean maximum lift coefficients. The function raised convergence issues that required a fixed thickness constraint for the optimiser to yield valid results. However, this only worked when the tether was not taken into account. Based upon the results with this new function, for airfoils without a tether, it was concluded that it was also possible to design for turbulent flow conditions only, in order to obtain airfoils that are not sensitive to rough conditions.

Fourthly, the functions for power production with a tether and building height were used again with turbulent flow conditions instead of semi-laminar conditions. This then resulted in airfoils optimised for power production and capable of performing well in rough conditions. These airfoils showed even higher lift coefficients up to 2.2 at higher angles of attack of 15 degrees. Similarly the drag increased again resulting in values of 0.01 to 0.015. These designs were shown to outperform existing high lift designs such as the S1223 with a higher maximum lift coefficient and less drag.

Lastly, it was decided to design airfoils with a small constant moment coefficient in the linear region. The small constant moment coefficient would reduce the need for a horizontal stabiliser and can improve the performance of the entire system instead of just the main wing. In order to keep using the same functions as before a new constraint was set up to ensure that the moment coefficient was near a reference value for the linear region of the airfoil. Three moment coefficients from unstable to neutrally stable were then used to generate three sets of airfoils. These airfoils showed lift coefficients between 1.4 and 1.8 at angles of 10 to 15 degrees with drag values of 0.01 to 0.015. The more unstable airfoils showed higher lift and drag values than the neutrally stable airfoils. These airfoils were compared to existing designs and it was found that they were better than some but airfoils such as the MH92 were still better in performance.

Thus it can be concluded that in general the added drag from a tether results in designs that start to neglect airfoil drag in favour of high lift. This is seen as the first design values without tether had half the drag or less compared to the other designs at maximum lift coefficient. The maximum lift coefficient also changed drastically as a tether was introduced going from values of 1.5 without tether to values of 2.2 with tether. When the moment coefficient was constrained the maximum lift coefficient dropped down to values between 1.4 and 1.8 while the drag stayed high due to tether drag dominating the design.

Recommendations

Very little work has been done regarding airfoils in the field of AWE. So far there has been the work of Cherubini and Venturato[29], that of de Oliveira, Pereira, and Fechner[30], and this thesis. Of which this thesis is the first to investigate the effects of a tether on airfoil design. As such there are plenty of recommendations to make for future works.

Firstly, the effects of the tether drag should be further investigated. This thesis makes use of a simple estimation using angular momentum but the accuracy of this estimation should be researched. And then based upon this research the question whether or not cable drag truly dominates airfoil drag should reexamined.

Secondly, it should be investigated how important roughness sensitivity is for AWE. For conventional wind turbines roughness sensitivity is considered far more important than for standard aircraft due to the difficulty of maintenance and downtime. Although downtime would still be an issue for AWE maintenance should be easier as the system would be on the ground for maintenance. In fact it might be possible to use the downtime of a system during low speeds or high speeds, when a conventional turbine also would not operate, for maintenance as the system has to be reeled in and stored during this time. Thus taking into account the costs of maintenance and downtime would it be desirable to generate designs for laminar or semi-laminar flow that might result in higher performance?

Thirdly, the effects of a tether on more than just drag and weight should be investigated. From personal experience it was already found that a bridle system could reduce wing bending on a prototype. Could a bridle and tether be used to reduce other problems? If a bridle was attached to the leading edge and trailing edge could this be used to influence the moment behaviour of the airfoil? Thus allowing for control options outside conventional methods, such as ailerons, which influence airfoil behaviour.

Fourthly, it was found that existing airfoils such as the MH92, which has positive moment coefficients, performs similar or better than the zero moment coefficient designs in this thesis. It should be investigated if optimised designs for positive moment coefficients can outperform the zero moment coefficient designs in this thesis as the MH92 does.

Lastly, during this thesis it was found that high lift designs would be best for power production. Thus airfoil designs taking high lift devices into account should be looked into. If it possible to obtain maximum lift coefficients around 2.2 for airfoils without high lift devices using optimisation techniques, how high could the maximum lift coefficient become when optimising an airfoil for use with a high lift device?

Bibliography

[1] de Oliveira Andrade, G., *Wind Turbine Airfoils with Boundary Layer Suction A Novel Design Approach*, MSc. Thesis, Delft University of Technology, 2011.

[2] Kulfan, B. M., "A Universal Parametric Geometry Representation Method - CST," 45th AIAA Aerospace Sciences Meeting and Exhibit, American Institute of Aeronautics and Astronautics, 2007.

[3] Deb, K., Pratap, A., Agarwal, S., and Meyarivan, T., "A Fast and Elitist Multiobjective Genetic Algorithm: NSGA-II," Tech. rep., Institute of Electrical and Electronics Engineers, 2002.

[4] de Oliveira, G., Pereira, R., Timmer, N., and van Rooij, R., "Improved airfoil polar predictions with data-driven boundary-layer closure relations," *Journal of Physics: Conference Series*, Vol. 1037, No. 2, 2018.

[5] Houska, B. and Diehl, M., "Optimal Control of Towing Kites," Proceedings of the 45th IEEE Conference on Decision & Control, Institute of Electrical and Electronics Engineers, 2006.

[6] Cherubini, A., Papini, A., Vertechy, R., and Fontana, M., "Airborne Wind Energy Systems: A review of the technologies," *Renewable and Sustainable Energy Reviews*, Vol. 51, No. 1, 2015, pp. 1461–1476.

[7] Kapania, N. R., Terraciano, K., and Taylor, S., "Modeling the Fluid Flow around Airfoils Using Conformal Mapping," Tech. rep., Society for Industrial and Applied Mathematics, August 29, 2008.

[8] Eppler, R., "Some New Airfoils," Tech. rep., Universität Stuttgart, 1979.

[9] Somers, D. M., "Design and Experimental Results for the S809 Airfoil," Tech. rep., National Renewable Energy Laboratory, 1997.

[10] Timmer, W. A. and van Rooij, R. P. J. O. M., "Summary of the Delft University Wind Turbine Dedicated Airfoils," Tech. rep., American Institute of Aeronautics and Astronautics, 2003.

[11] Dahl, K. S. and Fuglsang, P., "Design of the Wind Turbine Airfoil Family RISØ-A-XX," Tech. rep., Riso National Laboratory, Roskilde, Denmark, 12-1998.

[12] International Energy Agency, "World Energy Outlook 2016 Executive Summary," 2016.

[13] Uwe Ahrens, Moritz Diehl, R. S., *Airborne Wind Energy*, Springer-Verlag, Heidelberg, Germany, 2013.

[14] Abbott, I. H., von Doenhoff, A. E., and Stivers, L. S., "Summary of Airfoil Data," Tech. rep., National Advisory Committee for Aeronautics, 1945.

[15] Hermann Schlichting, K. G., *Boundary-Layer Theory*, Springer-Verlag, Heidelberg, Germany, 2017.

[16] Bowers, A. H. and Sim, A. G., "A Comparison of Wortmann Airfoil Computer-Generated Lift and Drag Polars With Flight and Wind tunnel Results," Tech. rep., National Aeronautics and Space Administration, 1984.

[17] Gaster, M., "The Structure and Behaviour of Laminar Separation Bubbles," Tech. rep., Aeronautical Research Council Reports and Memoranda, March 1967.

[18] Somers, D. M., "The S825 and S826 Airfoils," Tech. rep., National Renewable Energy Laboratory, 2005.

[19] Drela, M., "XFOIL:An Analysis and Design System for Low Reynolds Number Airfoils," Tech. rep., Massachusetts Institute of Technology, 1989.

[20] van Rooij, R., "Modification of the boundary layer calculation in RFOIL for improved airfoil stall prediction," Tech. rep., Delft University of Technology, 1996.

[21] Gao, L., Zhang, H., Liu, Y., and Han, S., "Effects of vortex generators on a blunt trailing-edge airfoil for wind turbine," *Renewable Energy*, Vol. 76, No. 1, 2014, pp. 303–311.

[22] Zhang, L., Li, X., Yang, K., and Xue, D., "Effects of vortex generators on aerodynamic performance of thick wind turbine airfoils," *Journal of Wind Engineering and Industrial Aerodynamics*, Vol. 156, No. 1, 2016, pp. 84–92.

[23] Giguére, P. and Selig, M. S., "New Airfoils for Small Horizontal Axis Wind Turbines," Tech. rep., American Society of Mechanical Engineers, 1998.

[24] Shah, H., Bhattarai, N., Mathew, S., and Lin, C. M., "Low Reynolds Number for Small Horizontal Axis Wind Turbine Blades," Sustainable Future Energy 2012 and 10th See Forum, Innovations for Sustainable and Secure Energy, 2012.

[25] Wang, H., Zhang, B., Qiu, Q., and Xu, X., "Flow control on the NREL S809 wind turbine airfoil using vortex generators," *Energy*, Vol. 118, No. 1, 2016, pp. 1210–1221.

[26] Manolesos, M. and Voutsinas, S. G., "Experimental investigation of the flow past passive vortex generators on an airfoil experiencing three-dimensional separation," *Journal of Wind Engineering and Industrial Aerodynamics*, Vol. 142, No. 1, 2015, pp. 130–148.

[27] Martínez-Filgueira, P., Fernandez-Gamiz, U., Zulueta, E., Errasti, L., and Fernandez-Gauna, B., "Parametric study of low-profile vortex generators," *Hydrogen Energy*, Vol. 42, No. 1, 2017, pp. 17700–17712.

[28] Rezaeiha, A., Pereira, R., and Kotsonis, M., "Fluctutations of angle of attack and lift coefficient and the resultant fatigue loads for a large Horizontal Axis Wind Turbine," *Renewable Energy*, Vol. 114, No. 1, 2017, pp. 904–916.

[29] Venturato, A., *Analisi fluidodinamica del profilo alare Clark-Y ed ottimizzazione multi-obbiettivo tramite algoritmo genetico*, MSc. Thesis, Università degli studi di Padova, 2013.

[30] Fechner, U., Pereira, R., and de Oliveira Andrade, G., "Multi-objective airfoil design for airborne wind energy," Airborne Wind Energy Conference, 2017.

[31] M'endez, B., Munduate, X., and Miguel, U. S., "Airfoil family design for large offshore wind turbine blades," *Journal of Physics: Conference Series*, Vol. 524, 2014.

[32] He, Y. and Agarwal, R. K., "Shape Optimization of NREL S809 Airfoil for Wind Turbine Blades Using a Multiobjective Genetic Algorithm," *International Journal of Aerospace Engineering*, 2014.

[33] Carpentieri, G., van Tooren, M. J., and Koren, B., "Aerodynamic Shape Optimization by Means of Sequential Linear Programming Techniques," Tech. rep., Delft University of Technology, 2006.

[34] Zhang, Q. and Li, H., "MOEA/D A Multiobjective Evolutionary Algorithm Based on Decomposition," *IEEE Transactions on Evolutionary Computation*, Vol. 11, No. 6, 2007, pp. 712–713.

[35] Zitzler, E., Laumanns, M., and Thiele, L., "SPEA2 Improving the Strength Pareto Evolutionary Algorithm," Tech. rep., Swiss Federal Institute of Technology Zurich, 2001.

[36] Ragni, D. and Correale, C. S. F. G., "Experimental investigation of an optimized airfoil for vertical-axis wind turbines," *Wind Energy*, Vol. 18, No. 9, 2015, pp. 1629–1643.

[37] Kemp, R., *Airfoil Optimization for vertical axis wind turbines*, MSc. Thesis, Delft University of Technology, 2015.

[38] Vila, M. C. and Alfaro, D. M., "New Airfoil Family Design for Large Wind Turbine Blades," 33rd Wing Energy Symposium, American Institute of Aeronautics and Astronautics, 2015.

[39] Pereira, R., Timmer, W., de Oliveira, G., and van Bussel, G., "Design of HAWT airfoils tailored for active flow control," *Wind Energy*, Vol. 20, No. 1, 2017, pp. 1569–1583.

[40] Batlle, E. C., Pereira, R., Kotsonis, M., and de Oliveira, G., "Airfoil Optimisation for DBD Plamsa Actuator in a Wind Energy Environment: Design and Experimental Study," Tech. rep., American Institute of Aeronautics and Astronautics, 2017.

[41] Dijkstra, P., *Rotor noise and aeroacoustic optimization of wind turbine airfoils*, MSc. Thesis, Delft University of Technology, 2015.

[42] Deb, K. and Jain, H., "An Evolutionary Many-Objective Optimization Algorithm Using Reference-Point-Based Nondominated Approach, Part I: Solving Problems with Box Constraints," *IEEE Transactions on Evolutionary Computation*, Vol. 18, No. 4, 2013, pp. 577–601.

[43] Kulfan, B. M., "Recent extensions and applications of the CST universal parametric geometry representation method," *The Aeronautical Journal*, Vol. 114, No. 1153, 2010, pp. 157–176.

[44] Loyd, M. L., "Crosswind Kite Power," *Journal of Energy*, Vol. 4, No. 3, 1980, pp. 106–111.

[45] van Ingen, J. L., "The e^N method for transition prediction. Historical review of work at TU Delft," 38th Fluid Dynamics Conference and Exhibit, American Institute of Aeronautics and Astronautics, 2008.

[46] Bjorck, A., "Coordinates and Calculations for the FFA-Wl-xxx, FFA-W2-xxx and FFA-W3-xxx Series of Airfoils for Horizontal Axis Wind Turbines," Tech. rep., The Aeonautical Research Institute of Sweden, 1990.

[47] Dadone, L. U., "Design and Analytical Study of a Rotor Airfoil," Tech. rep., National Aeronautics and Space Administration, May 1978.

Selection of DU 18-K Airfoils

In this appendix the coordinates for a selection of DU 18-K airfoils can be found. The shapes for each airfoil is depicted and the coordinates of each airfoil can be found in the following pages following the same order as the figures.

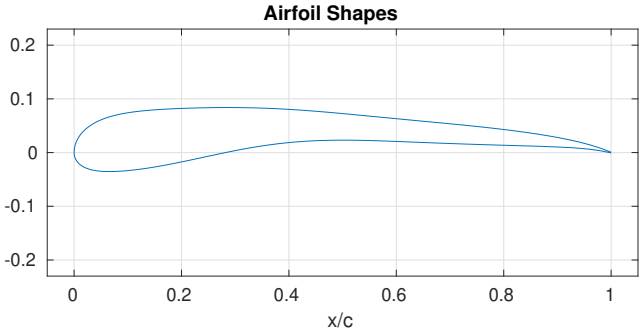

(a) *DU 18-K12*

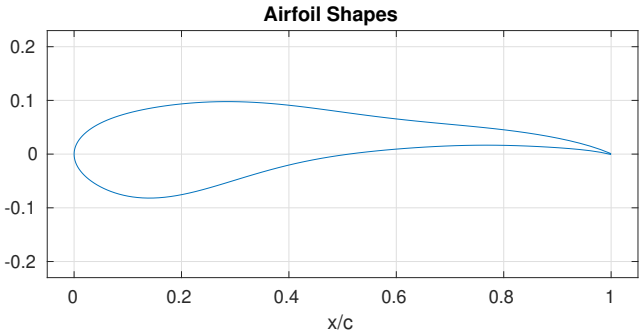

(b) *DU 18-K18*

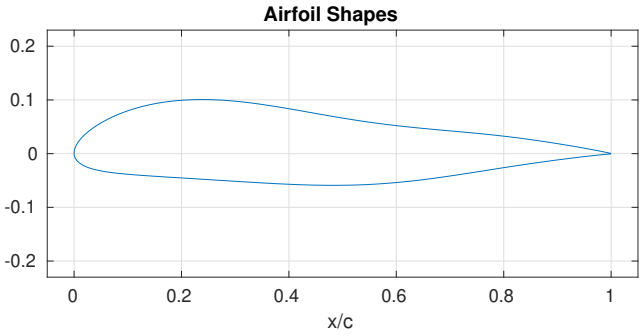

(c) *DU 18-K16-00*

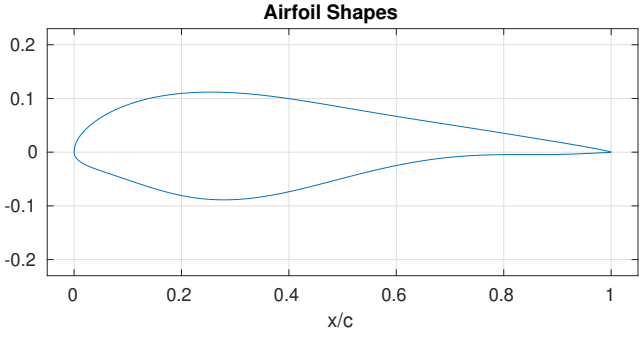

(d) *DU 18-K20-05*

DU 18-K12

Coordinates for the DU 18-K12 airfoil. Reading two columns at a time is the same as tracing the airfoil from trailing edge to leading edge along the suction side back to trailing edge along the pressure side.

suction				pressure			
x/c	y/c	x/c	y/c	x/c	y/c	x/c	y/c
1.0000	0.0007	0.2929	0.0838	0.0002	-0.0032	0.3069	0.0050
0.9804	0.0082	0.2791	0.0838	0.0008	-0.0064	0.3212	0.0076
0.9607	0.0143	0.2657	0.0838	0.0017	-0.0096	0.3357	0.0101
0.9411	0.0195	0.2525	0.0836	0.0031	-0.0126	0.3506	0.0125
0.9215	0.0239	0.2396	0.0834	0.0048	-0.0155	0.3656	0.0146
0.9020	0.0278	0.2270	0.0831	0.0069	-0.0183	0.3809	0.0166
0.8825	0.0313	0.2147	0.0827	0.0094	-0.0209	0.3964	0.0183
0.8630	0.0344	0.2027	0.0823	0.0123	-0.0233	0.4122	0.0197
0.8436	0.0373	0.1910	0.0819	0.0156	-0.0255	0.4282	0.0209
0.8242	0.0399	0.1796	0.0813	0.0192	-0.0275	0.4444	0.0218
0.8049	0.0424	0.1685	0.0808	0.0232	-0.0293	0.4609	0.0225
0.7857	0.0447	0.1578	0.0801	0.0276	-0.0308	0.4775	0.0229
0.7666	0.0468	0.1474	0.0794	0.0324	-0.0321	0.4943	0.0231
0.7475	0.0489	0.1373	0.0786	0.0375	-0.0332	0.5114	0.0231
0.7286	0.0508	0.1275	0.0776	0.0431	-0.0340	0.5286	0.0229
0.7097	0.0527	0.1181	0.0766	0.0489	-0.0347	0.5460	0.0225
0.6910	0.0545	0.1090	0.0755	0.0552	-0.0351	0.5636	0.0220
0.6724	0.0563	0.1003	0.0742	0.0618	-0.0353	0.5813	0.0214
0.6539	0.0580	0.0919	0.0727	0.0688	-0.0353	0.5993	0.0208
0.6355	0.0597	0.0838	0.0711	0.0761	-0.0352	0.6173	0.0201
0.6173	0.0614	0.0761	0.0694	0.0838	-0.0348	0.6355	0.0193
0.5993	0.0632	0.0688	0.0674	0.0919	-0.0343	0.6539	0.0186
0.5813	0.0649	0.0618	0.0653	0.1003	-0.0335	0.6724	0.0179
0.5636	0.0666	0.0552	0.0630	0.1090	-0.0326	0.6910	0.0172
0.5460	0.0683	0.0489	0.0604	0.1181	-0.0316	0.7097	0.0165
0.5286	0.0699	0.0431	0.0577	0.1275	-0.0303	0.7286	0.0159
0.5114	0.0716	0.0375	0.0549	0.1373	-0.0289	0.7475	0.0153
0.4943	0.0731	0.0324	0.0518	0.1474	-0.0273	0.7666	0.0147
0.4775	0.0747	0.0276	0.0485	0.1578	-0.0255	0.7857	0.0141
0.4609	0.0761	0.0232	0.0451	0.1685	-0.0236	0.8049	0.0135
0.4444	0.0774	0.0192	0.0415	0.1796	-0.0215	0.8242	0.0129
0.4282	0.0786	0.0156	0.0378	0.1910	-0.0193	0.8436	0.0124
0.4122	0.0797	0.0123	0.0340	0.2027	-0.0169	0.8630	0.0118
0.3964	0.0807	0.0094	0.0300	0.2147	-0.0143	0.8825	0.0111
0.3809	0.0815	0.0069	0.0259	0.2270	-0.0117	0.9020	0.0103
0.3656	0.0822	0.0048	0.0217	0.2396	-0.0090	0.9215	0.0093
0.3506	0.0828	0.0031	0.0175	0.2525	-0.0062	0.9411	0.0080
0.3357	0.0832	0.0017	0.0132	0.2657	-0.0034	0.9607	0.0061
0.3212	0.0835	0.0008	0.0088	0.2791	-0.0006	0.9804	0.0034
0.3069	0.0837	0.0002	0.0044	0.2929	0.0022	1.0000	-0.0007
		0.0000	0.0000				

DU 18-K18

Coordinates for the DU 18-K18 airfoil. Reading two columns at a time is the same as tracing the airfoil from trailing edge to leading edge along the suction side back to trailing edge along the pressure side.

suction				pressure			
x/c	y/c	x/c	y/c	x/c	y/c	x/c	y/c
1.0000	0.0008	0.2929	0.0977	0.0002	-0.0041	0.3069	-0.0463
0.9804	0.0085	0.2791	0.0977	0.0008	-0.0081	0.3212	-0.0419
0.9607	0.0149	0.2657	0.0975	0.0017	-0.0121	0.3357	-0.0376
0.9411	0.0204	0.2525	0.0971	0.0031	-0.0162	0.3506	-0.0333
0.9215	0.0252	0.2396	0.0965	0.0048	-0.0201	0.3656	-0.0292
0.9020	0.0294	0.2270	0.0958	0.0069	-0.0241	0.3809	-0.0251
0.8825	0.0331	0.2147	0.0948	0.0094	-0.0281	0.3964	-0.0212
0.8630	0.0365	0.2027	0.0937	0.0123	-0.0320	0.4122	-0.0175
0.8436	0.0395	0.1910	0.0925	0.0156	-0.0358	0.4282	-0.0141
0.8242	0.0422	0.1796	0.0912	0.0192	-0.0396	0.4444	-0.0108
0.8049	0.0447	0.1685	0.0897	0.0232	-0.0434	0.4609	-0.0078
0.7857	0.0470	0.1578	0.0881	0.0276	-0.0470	0.4775	-0.0050
0.7666	0.0490	0.1474	0.0864	0.0324	-0.0506	0.4943	-0.0024
0.7475	0.0510	0.1373	0.0845	0.0375	-0.0541	0.5114	0.0000
0.7286	0.0528	0.1275	0.0826	0.0431	-0.0575	0.5286	0.0022
0.7097	0.0546	0.1181	0.0806	0.0489	-0.0608	0.5460	0.0042
0.6910	0.0563	0.1090	0.0784	0.0552	-0.0639	0.5636	0.0060
0.6724	0.0580	0.1003	0.0762	0.0618	-0.0669	0.5813	0.0077
0.6539	0.0598	0.0919	0.0739	0.0688	-0.0696	0.5993	0.0092
0.6355	0.0617	0.0838	0.0714	0.0761	-0.0722	0.6173	0.0107
0.6173	0.0636	0.0761	0.0688	0.0838	-0.0745	0.6355	0.0120
0.5993	0.0656	0.0688	0.0662	0.0919	-0.0766	0.6539	0.0131
0.5813	0.0677	0.0618	0.0634	0.1003	-0.0783	0.6724	0.0141
0.5636	0.0698	0.0552	0.0605	0.1090	-0.0797	0.6910	0.0150
0.5460	0.0721	0.0489	0.0576	0.1181	-0.0808	0.7097	0.0157
0.5286	0.0744	0.0431	0.0545	0.1275	-0.0816	0.7286	0.0162
0.5114	0.0767	0.0375	0.0513	0.1373	-0.0819	0.7475	0.0165
0.4943	0.0790	0.0324	0.0480	0.1474	-0.0818	0.7666	0.0166
0.4775	0.0813	0.0276	0.0447	0.1578	-0.0813	0.7857	0.0165
0.4609	0.0835	0.0232	0.0412	0.1685	-0.0804	0.8049	0.0162
0.4444	0.0857	0.0192	0.0377	0.1796	-0.0790	0.8242	0.0157
0.4282	0.0877	0.0156	0.0341	0.1910	-0.0772	0.8436	0.0150
0.4122	0.0896	0.0123	0.0305	0.2027	-0.0750	0.8630	0.0141
0.3964	0.0914	0.0094	0.0268	0.2147	-0.0724	0.8825	0.0130
0.3809	0.0929	0.0069	0.0231	0.2270	-0.0695	0.9020	0.0118
0.3656	0.0943	0.0048	0.0193	0.2396	-0.0662	0.9215	0.0103
0.3506	0.0954	0.0031	0.0155	0.2525	-0.0626	0.9411	0.0086
0.3357	0.0963	0.0017	0.0116	0.2657	-0.0588	0.9607	0.0063
0.3212	0.0970	0.0008	0.0078	0.2791	-0.0548	0.9804	0.0034
0.3069	0.0975	0.0002	0.0039	0.2929	-0.0506	1.0000	-0.0008
		0.0000	0.0000				

DU 18-K16-00

Coordinates for the DU 18-K16-00 airfoil. Reading two columns at a time is the same as tracing the airfoil from trailing edge to leading edge along the suction side back to trailing edge along the pressure side.

suction				pressure			
x/c	y/c	x/c	y/c	x/c	y/c	x/c	y/c
1.0000	0.0004	0.2929	0.0983	0.0002	-0.0026	0.3069	-0.0519
0.9804	0.0045	0.2791	0.0993	0.0008	-0.0051	0.3212	-0.0528
0.9607	0.0082	0.2657	0.1001	0.0017	-0.0076	0.3357	-0.0537
0.9411	0.0117	0.2525	0.1005	0.0031	-0.0100	0.3506	-0.0545
0.9215	0.0151	0.2396	0.1007	0.0048	-0.0124	0.3656	-0.0554
0.9020	0.0183	0.2270	0.1006	0.0069	-0.0147	0.3809	-0.0561
0.8825	0.0214	0.2147	0.1002	0.0094	-0.0170	0.3964	-0.0569
0.8630	0.0243	0.2027	0.0996	0.0123	-0.0191	0.4122	-0.0575
0.8436	0.0270	0.1910	0.0986	0.0156	-0.0211	0.4282	-0.0581
0.8242	0.0296	0.1796	0.0974	0.0192	-0.0230	0.4444	-0.0586
0.8049	0.0320	0.1685	0.0960	0.0232	-0.0248	0.4609	-0.0589
0.7857	0.0341	0.1578	0.0943	0.0276	-0.0264	0.4775	-0.0590
0.7666	0.0362	0.1474	0.0924	0.0324	-0.0280	0.4943	-0.0590
0.7475	0.0381	0.1373	0.0903	0.0375	-0.0294	0.5114	-0.0587
0.7286	0.0398	0.1275	0.0879	0.0431	-0.0308	0.5286	-0.0583
0.7097	0.0415	0.1181	0.0854	0.0489	-0.0320	0.5460	-0.0576
0.6910	0.0432	0.1090	0.0827	0.0552	-0.0331	0.5636	-0.0566
0.6724	0.0449	0.1003	0.0798	0.0618	-0.0342	0.5813	-0.0554
0.6539	0.0466	0.0919	0.0768	0.0688	-0.0351	0.5993	-0.0539
0.6355	0.0484	0.0838	0.0737	0.0761	-0.0360	0.6173	-0.0522
0.6173	0.0502	0.0761	0.0704	0.0838	-0.0369	0.6355	-0.0502
0.5993	0.0523	0.0688	0.0671	0.0919	-0.0377	0.6539	-0.0480
0.5813	0.0544	0.0618	0.0636	0.1003	-0.0384	0.6724	-0.0456
0.5636	0.0567	0.0552	0.0601	0.1090	-0.0392	0.6910	-0.0430
0.5460	0.0591	0.0489	0.0566	0.1181	-0.0399	0.7097	-0.0402
0.5286	0.0617	0.0431	0.0530	0.1275	-0.0406	0.7286	-0.0373
0.5114	0.0644	0.0375	0.0493	0.1373	-0.0413	0.7475	-0.0344
0.4943	0.0671	0.0324	0.0457	0.1474	-0.0419	0.7666	-0.0314
0.4775	0.0700	0.0276	0.0420	0.1578	-0.0426	0.7857	-0.0284
0.4609	0.0729	0.0232	0.0384	0.1685	-0.0433	0.8049	-0.0254
0.4444	0.0758	0.0192	0.0348	0.1796	-0.0440	0.8242	-0.0224
0.4282	0.0787	0.0156	0.0312	0.1910	-0.0447	0.8436	-0.0195
0.4122	0.0815	0.0123	0.0276	0.2027	-0.0454	0.8630	-0.0167
0.3964	0.0842	0.0094	0.0241	0.2147	-0.0462	0.8825	-0.0140
0.3809	0.0868	0.0069	0.0205	0.2270	-0.0469	0.9020	-0.0114
0.3656	0.0893	0.0048	0.0171	0.2396	-0.0477	0.9215	-0.0089
0.3506	0.0915	0.0031	0.0136	0.2525	-0.0485	0.9411	-0.0066
0.3357	0.0936	0.0017	0.0102	0.2657	-0.0493	0.9607	-0.0043
0.3212	0.0954	0.0008	0.0068	0.2791	-0.0502	0.9804	-0.0022
0.3069	0.0970	0.0002	0.0034	0.2929	-0.0510	1.0000	-0.0004
		0.0000	0.0000				

DU 18-K20-05

Coordinates for the DU 18-K20-05 airfoil. Reading two columns at a time is the same as tracing the airfoil from trailing edge to leading edge along the suction side back to trailing edge along the pressure side.

suction				pressure			
x/c	y/c	x/c	y/c	x/c	y/c	x/c	y/c
1.0000	0.0004	0.2929	0.1108	0.0002	-0.0024	0.3069	-0.0879
0.9804	0.0047	0.2791	0.1114	0.0008	-0.0049	0.3212	-0.0867
0.9607	0.0085	0.2657	0.1118	0.0017	-0.0073	0.3357	-0.0851
0.9411	0.0120	0.2525	0.1119	0.0031	-0.0096	0.3506	-0.0830
0.9215	0.0154	0.2396	0.1117	0.0048	-0.0120	0.3656	-0.0806
0.9020	0.0186	0.2270	0.1113	0.0069	-0.0142	0.3809	-0.0777
0.8825	0.0218	0.2147	0.1106	0.0094	-0.0164	0.3964	-0.0745
0.8630	0.0250	0.2027	0.1097	0.0123	-0.0185	0.4122	-0.0709
0.8436	0.0282	0.1910	0.1085	0.0156	-0.0205	0.4282	-0.0672
0.8242	0.0313	0.1796	0.1071	0.0192	-0.0225	0.4444	-0.0631
0.8049	0.0345	0.1685	0.1055	0.0232	-0.0245	0.4609	-0.0589
0.7857	0.0375	0.1578	0.1037	0.0276	-0.0265	0.4775	-0.0546
0.7666	0.0406	0.1474	0.1016	0.0324	-0.0284	0.4943	-0.0502
0.7475	0.0436	0.1373	0.0994	0.0375	-0.0303	0.5114	-0.0458
0.7286	0.0465	0.1275	0.0969	0.0431	-0.0323	0.5286	-0.0414
0.7097	0.0494	0.1181	0.0943	0.0489	-0.0344	0.5460	-0.0371
0.6910	0.0523	0.1090	0.0914	0.0552	-0.0365	0.5636	-0.0329
0.6724	0.0552	0.1003	0.0884	0.0618	-0.0388	0.5813	-0.0288
0.6539	0.0581	0.0919	0.0853	0.0688	-0.0411	0.5993	-0.0250
0.6355	0.0610	0.0838	0.0820	0.0761	-0.0436	0.6173	-0.0214
0.6173	0.0639	0.0761	0.0786	0.0838	-0.0462	0.6355	-0.0182
0.5993	0.0668	0.0688	0.0750	0.0919	-0.0489	0.6539	-0.0152
0.5813	0.0698	0.0618	0.0714	0.1003	-0.0518	0.6724	-0.0126
0.5636	0.0727	0.0552	0.0677	0.1090	-0.0547	0.6910	-0.0104
0.5460	0.0756	0.0489	0.0639	0.1181	-0.0578	0.7097	-0.0086
0.5286	0.0786	0.0431	0.0600	0.1275	-0.0609	0.7286	-0.0071
0.5114	0.0815	0.0375	0.0560	0.1373	-0.0641	0.7475	-0.0060
0.4943	0.0844	0.0324	0.0521	0.1474	-0.0672	0.7666	-0.0052
0.4775	0.0873	0.0276	0.0481	0.1578	-0.0703	0.7857	-0.0048
0.4609	0.0901	0.0232	0.0440	0.1685	-0.0733	0.8049	-0.0045
0.4444	0.0928	0.0192	0.0400	0.1796	-0.0762	0.8242	-0.0044
0.4282	0.0954	0.0156	0.0360	0.1910	-0.0789	0.8436	-0.0045
0.4122	0.0979	0.0123	0.0319	0.2027	-0.0813	0.8630	-0.0045
0.3964	0.1002	0.0094	0.0279	0.2147	-0.0835	0.8825	-0.0044
0.3809	0.1023	0.0069	0.0239	0.2270	-0.0854	0.9020	-0.0042
0.3656	0.1043	0.0048	0.0199	0.2396	-0.0868	0.9215	-0.0037
0.3506	0.1061	0.0031	0.0159	0.2525	-0.0879	0.9411	-0.0031
0.3357	0.1076	0.0017	0.0119	0.2657	-0.0886	0.9607	-0.0022
0.3212	0.1089	0.0008	0.0079	0.2791	-0.0888	0.9804	-0.0012
0.3069	0.1100	0.0002	0.0040	0.2929	-0.0886	1.0000	-0.0004
		0.0000	0.0000				